ULTRASENSITIVE MAGNETOMETRY AND IMAGING WITH NV DIAMOND

A Dissertation

by

CHANGDONG KIM

Submitted to the Office of Graduate Studies of
Texas A&M University
in partial fulfillment of the requirements for the degree of

DOCTOR OF PHILOSOPHY

May 2010

Major Subject: Electrical Engineering

ULTRASENSITIVE MAGNETOMETRY AND IMAGING WITH NV DIAMOND

A Dissertation

by

CHANGDONG KIM

Submitted to the Office of Graduate Studies of
Texas A&M University
in partial fulfillment of the requirements for the degree of

DOCTOR OF PHILOSOPHY

Approved by:

Chair of Committee,	Philip Hemmer
Committee Members,	Steve Wright
	Jun Zou
	Winfried Teizer
Head of Department,	Costas Georghiades

May 2010

Major Subject: Electrical Engineering

ABSTRACT

Ultrasensitive Magnetometry and Imaging with NV Diamond.

(May 2010)

Changdong Kim, B.S., Korea University, Seoul, Korea;

M.S., Texas A&M University

Chair of Advisory Committee: Dr. Philip Hemmer

NV centers in a diamond are proving themselves to be good building blocks for quantum information, electron spin resonance (ESR) imaging, and sensor applications. The key feature of the NV is that it has an electron spin that can be polarized and read out at room temperature. The readout is optical, thus the magnetic field imaging can also be done easily. Magnetic field variation with feature sizes below 0.3 microns cannot be directly resolved, and so in this region magnetic resonance imaging must be employed. To realize the full sensitivity of NV diamond, the spin transition linewidth must be as narrow as possible. Additionally, in the case of NV ensembles for micron-sized magnetometers, there must be a high concentration of NV. To this end three techniques are explored: (1) Electron paramagnetic resonance (EPR) imaging with microwave field gradients, (2) Magic angle rotation of magnetic field, and (3) TEM irradiation to optimize the yield of NV in a diamond.

For the EPR imaging demonstration a resonant microwave field gradient is used in place of the usual DC magnetic gradient to obtain enough spatial resolution to resolve

two very close “double NV” centers in a type Ib bulk diamond. Microfabrication technology enabled the micron-size wire structure to sit directly on the surface of millimeter-scale diamond plate. In contrast to conventional magnetic resonance imaging pulsed ESR was used to measure the Rabi oscillations. From the beating of Rabi oscillations from a “double NV,” the pair was resolved using the one-dimension EPR imaging (EPRI) and the spatial distance was obtained.

To achieve high sensitivity in nitrogen-doped diamond, the dipole-dipole coupling between the electron spin of the NV center and the substitutional nitrogen (^{14}N) electron must be suppressed because it causes linewidth broadening. Magic angle spinning is an accepted technique to push T_2 and T_2^* down toward the T_1 limit. An experiment was performed using the HPHT diamond with a high concentration of nitrogen, and a rotating field was applied with a microfabricated wire structure to reduce line broadening. In this experiment, ~50% suppression of the linewidth was observed and the effective time constant T_2^* improved from 114 ns to 227 ns.

To achieve the highest possible sensitivity for micro-scale magnetic sensors the concentration of NV should be large. Since the unconverted N are magnetic impurities they shorten T_2 and T_2^*, giving a tradeoff between NV (and therefore N) concentration and sensitivity. To construct a damage monitor, a type Ib HPHT sample was irradiated with electrons from a transmission electron microscope (TEM) and the effects on the ESR transition were seen well before physical damage appeared on the diamond and thus this proved to be a sensitive metric for irradiation damage.

DEDICATION

To My Wife and Son, Grace and Micah, and Family

ACKNOWLEDGEMENTS

I would like to thank my professors, Dr. Hemmer (advisor and chair), Dr. Wright, Dr. Zou, and Dr. Teizer in my committee, for their huge academic contribution and support. A special thanks goes to Dr. Wrachtrup, Dr. Jelezko, Gopi, and Florian at Universität Stuttgart for their willingness to help me in the research. I also want to extend my gratitude to Dr. Budker, Victor, and Erik at UC Berkeley for enriching my understanding and knowledge. Thanks also goes to my friend, Alek, for his input on my experiments. Finally, thanks to my family for their encouragement and to my wife for her patience and love.

TABLE OF CONTENTS

Page

LIST OF FIGURES

FIGURE Page

FIGURE Page

FIGURE Page

FIGURE Page

LIST OF TABLES

CHAPTER I

INTRODUCTION

1.1 Motivation

As predicted by Moore's law[1], we have observed the scaling down of the electronic devices and their rapid development. In nanometer-sized devices, quantum effects cannot be ignored and spin electronics (or spintronics) was developed to handle both the electron charge and spin and has a better capability to explain the expected physical phenomena[2]. The giant magnetoresistive (GMR) hard-drive head developed in 1998 can be considered the first spintronic device. Most recently an involatile magnetic random access memory (MRAM) has been researched and is due to emerge into the market soon.

In addition to the information storage, spintronics can be applied to quantum computing as well as spin-based multifunctional devices, like the spin-transistor, spin-LED, and high-speed optical switches[3]. Controlling a single spin with light offers a pathway toward these applications. Recently spintronics has been researched in a few optically detected systems[4], such as quantum dot[5,6], GaAs quantum well[7], and diamond[8,9].

The advancement of spintronics depends on the development of novel materials, micro/nano-fabrication of new structures exhibiting spintronics phenomena. In order to characterize such magnetic materials and devices, magnetic imaging techniques and

---

This dissertation follows the style of Physical Review B.

methods with the sensitivity to detect very small magnetic fields can provide spatial measurements of the sample structure and its corresponding magnetic properties[10]. Among the approaches for magnetic imaging are microscopy techniques such as the magnetic force microscopy (MFM)[11] and conventional micromagnetometer devices, for example, the scanned superconducting quantum interface device (SQUID) magnetometer[12].

Recently, diamond-based materials have emerged as novel candidates for spintronics[13]. The nitrogen vacancy (NV) center in diamond has a long electron spin coherence time at room temperature. Already key applications, such as the single photon transistor[14], quantum logic[15], and nanoscale magnetic imaging[16] have demonstrated using advanced implantation and spin manipulation techniques. The motivation behind the research of NV diamond is the potential to develop room temperature devices for spintronics applications from information storage to quantum computing.

Quantum Computing

Compared to the conventional computer, the quantum computer can speed up information processing quadratically or exponentially and transport data with complete secrecy[17]. Divincenzo provided a few basic criteria for the physical implementation of a quantum computer and many approaches have been developed[18].

There exist many candidates for quantum bit, qubit, depending on the experimental system: nuclear magnetic resonance (NMR), ion trap, neutral atom, cavity quantum electro-dynamic (QED), optical or solid state quantum computation, and other techniques. Each approach has its own strengths and weakness and has been researched to determine what is needed to implement a quantum computer.

The NV center is one of these candidates. One of its main advantages is that it has a long coherence time at room temperature. The current status of quantum computing for the NV center according to the Divincenzo criteria is summarized in Table 1. Since the NV center is based on an electron spin in a solid state material, it provides more scalability to extend to multiple-qubit processors using the current semiconductor fabrication technologies.

Table 1. Quantum computing roadmap of NV center according to Divincenzo criteria.

Divincenzo Criteria	NV Cetner at Room Temperature
1. Well-characterized qubit	Achieved
2. Initialize the qubit state	Achieved
3. Long coherence time	Achieved
4. Universal set of quantum gates	Achieved
5. Qubit-specific measurement capability	Achieved
6. Interconvert stationary and flying qubits	Proposed
7. Transmit flying qubits	Proposed

Note: Adapted from *A Quantum Information Science and Technology Roadmap* by ARDA, http://qist.lanl.gov, 2004 and "Room-Temperature Solid-State Quantum Processors in Diamond" by P. R. Hemmer and M. Lukin, Proc. of SPIE Vol. 6976 , 697602 (2008).

Magnetic Imaging Using the NV Center

For paramagnetic species such as the NV center, electron paramagnetic resonance (EPR) imaging techniques have made a huge contribution in obtaining the spatial resolution and understanding the nature of impurities in solid state materials. EPR techniques have been performed to identify and detect molecules mainly in biological systems and solid state applications.

As in NMR imaging (NMRI) or magnetic resonance imaging (MRI), EPR imaging (EPRI) consists of measuring the electron spin resonance (ESR) spectra in the existence of the gradient field to produce an image of electron spins in the sample[19]. One of challenges in EPRI using the gradient field is that it generally requires a higher field gradient than NMRI because the EPRI signals are complicated by the hyperfine coupling and anisotropic g-factor. As a possible technique to overcome this and more easily reach the T_1 limit, a microwave gradient field can be used, but is generally difficult to implement.

In previous magnetic imaging studies using the NV center, a one-dimensional (1D) DC gradient field was used to get a 1D image. To achieve 2D imaging, a new structure is required. At the same time the metal gradient-wire structure for the microwave signals needs to be improved as it was fabricated on a separate substrate and therefore a gap existed between the NV center and the gradient-producing structure. In order to reduce the gap and obtain the highest gradient field, direct fabrication on the diamond is necessary. In principle, higher spatial resolution can be obtained with this higher gradient field. By making the gradient wire structures out of coplanar stripline design a high microwave gradient field can be easily obtained.

Microdevice for Imaging: Magnetometer

One of the key applications of magnetic imaging is to construct a microdevice for magnetic field measurements. Here the emphasis shifts from obtaining high spatial resolution of electron spins to mapping the local field with high sensitivity. SQUID magnetometers provide this capability today but the drawback is that they need cryogenic cooling to function properly.

Figure 1 shows the sensitivity and size scales for magnetometry techniques, such as Hall probes with a simpler structure at room temperature[20], magnetic resonance force microscopy (MRFM)[21] and atomic vapor magnetic sensors. Each technique has a different sensitivity and an optimum size range.

As shown in the Figure 1 by the shot noise projection, the NV magnetometer can provide magnetic field detection with high sensitivity on small size scales at room temperature. Using a single NV spin in a nanodiamond mounted on an atomic force microscope (AFM) scanning probe, the NV can in principle be brought in close enough proximity to detect the magnetic field generated by a single electron or nuclear spin as shown by the dashed lines in Figure 1 in the region of “Demo 1.” Further, a bulk diamond can be used to detect magnetic material variations at the micron scale with ultrahigh sensitivity[22] as shown by the region labeled “Demo 3.”

For bulk diamond magnetometry, one way to improve the sensitivity is to increase the NV concentration, but this causes linewidth broadening due to the dipole-dipole coupling [see Figure 2]. In principle this can be reduced by using a rotating sample. However this is very inconvenient for micro-imaging applications because of the difficulty of maintaining high spatial resolution while rotating at high speeds. An alternative is to rotate the magnetic field using micro-stripline structures attached to the diamond. Still another way to suppress broadening and high NV concentration is to note that most of this broadening comes from interactions between NV and residual substitutional N that has not formed NVs. In this case, higher sensitivity should be achievable by eliminating the residual N using electron irradiation to convert them to NV centers. Here the issue is how to prevent damage to the diamond at high radiation doses, and especially how to minimize the effect of damage on the NV magnetic sensitivity.

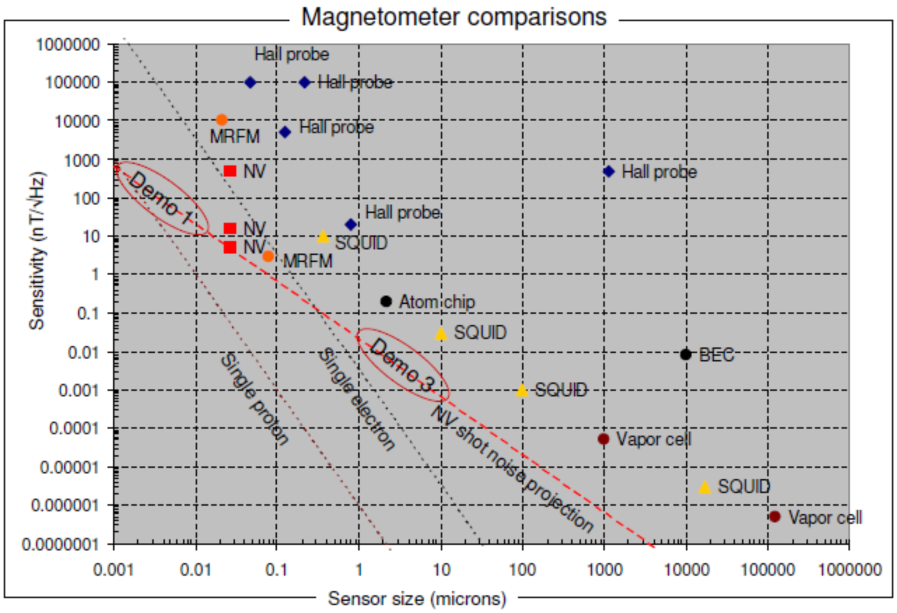

Figure 1. Sensitivity of magnetometer techniques is depicted.

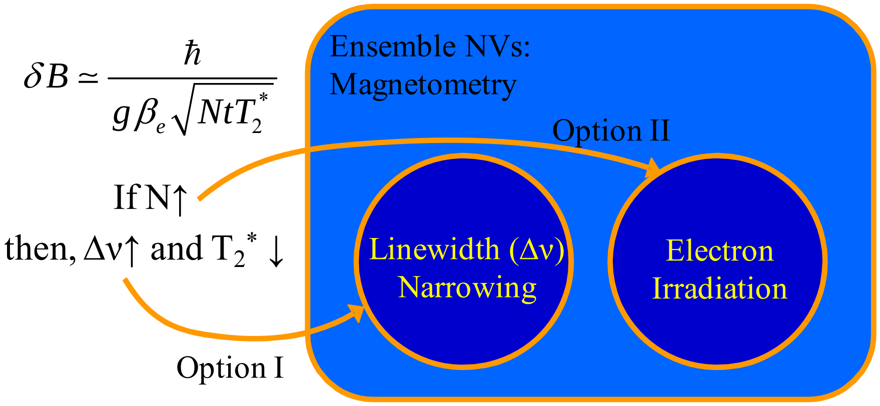

Figure 2. For the bulk diamond magnetometer, the sensitivity δB can be improved using the higher concentration of the NV center but it causes the linewidth broadening. One option is to suppress the inhomogeneous linewidth broadening using the rotating field. The other option is the electron irradiation to convert the residual nitrogen to the NV center.

1.2 Nitrogen Vacancy in Diamond

The tremendous advances in diamond defect modelings have made possible the recent experimental breakthroughs in the study of nitrogen vacancy. Since du Preeze first discovered the NV^- center of the 1.945 eV absorption line (637 nm) in 1965[23], the NV^- defect has attracted considerable attention as a good candidate for a qubit of a quantum computer as well as a single photon source for quantum information processing [24,25,26,27]. The uniaxial stress measurements by Davies and Hamer in 1976 showed that 1.945 eV absorption is a transition between an A ground state and an E excited state of a trigonal center[28]. Two-laser hole burning measurement[29], electron spin resonance (ESR)[30 31], optically detected spin coherence[32] and Raman heterodyne detection[33] confirmed that the NV^- has a triplet ^3A ground state[29] which is the essential property of the NV center. Collins, Thomaz, and Jorge also showed that that the optically excited state is a spin triplet[34].

Nitrogen is the most abundant impurity in natural, high pressure high temperature (HPHT) and chemical vapor deposition (CVD) diamonds. Nitrogen defects are effective in trapping migrating vacancies. One of the most studied paramagnetic defects is the negatively charged nitrogen vacancy center (NV^-) which is composed of a substitutional nitrogen adjacent to a vacancy[35]. Experimental results have proved that the NV center exists in two charge states, NV^0 and NV^-, with the neutral state exhibiting a zero-phonon line (ZPL) at 575 nm and the singly–charged state at 637 nm (1.945 eV)[35,36,37]. In order to form the defects in a diamond, the neutral substitutional nitrogen center, N_S^0, is irradiated to produce vacancies and the diamond is annealed to allow the vacancies to migrate as follows[38,39]:

$$\begin{aligned} &N_S^0 + V^0 \rightarrow NV^0 \quad \text{and} \\ &NV^0 + N_S^0 \rightarrow NV^- + N_S^+ \end{aligned} \tag{1}$$

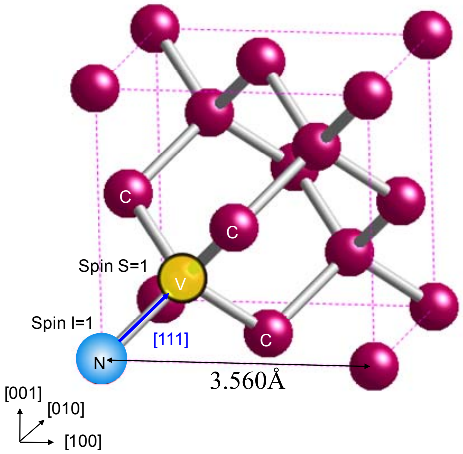

Figure 3. Schematic diagram of the nitrogen vacancy defect in the diamond.

If the NV^0 gains an extra negative charge, which is added to the five electrons (the three dangling carbon bonds and two valence electrons from the nitrogen), there are six electrons associated with the NV center[40]. The electron spin of the NV center is defined by the coupling between the captured electron from carbonic lattice of diamond and the unpaired electron from the nitrogen atom, resulting in a spin $S = 1$. Thus, the NV center exists as a paramagnetic impurity. Figure 3 shows a physical view of the NV defect center in diamond. Based on neutron irradiation experiments, the NV defect has been identified as a negatively charged center[36].

The NV^- defect center in diamond has a few characteristics that can be used to identify it. The fluorescence emission spectrum shows the zero phonon line (ZPL) at 637 nm and the sidebands which are dominated by the NV^- center [Figure 4(a)]. If a microwave signal is applied to the NV^- center, it shows the electron paramagnetic resonance (EPR) or electron spin resonance (ESR) at 2.87 GHz which is called the zero-field splitting with no external magnetic field applied [Figure 4(b)]. Using these two methods, the properties of the NV center are analyzed and characterized effectively.

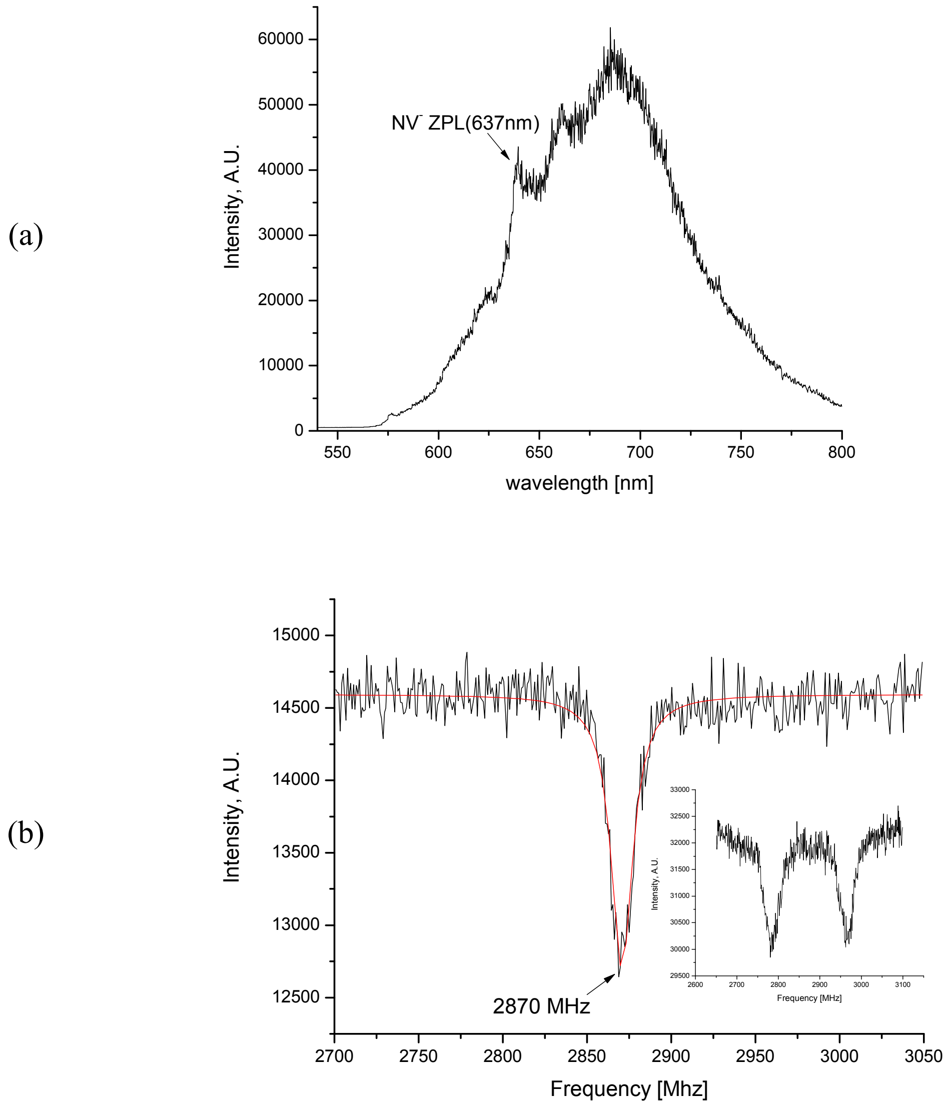

Figure 4. (a) Typical spectrum for the NV^{-} center shows the ZPL at 637 nm. (b) If the microwave signal is swept, the NV^{-} center has the EPR resonance frequency at 2.87 GHz.

1.3 Dissertation Outline

This dissertation reviews the EPR properties of single NV centers in diamond and outlines its experimental methods and results for a few applications. The material presented is as follows: Chapter II describes the spin properties of the NV center such as the spin Hamiltonian and hyperfine coupling and gives the theoretical background to ODMR on single NV centers. It also covers the Rabi oscillation, T_1, T_2, and T_2^* which are obtainable from the continuous wave (CW)/pulsed ESR experiments. Chapters III to V cover three applications, which are presented in an independent journal format with some repetition of their theoretical background. First, Chapter III presents the experimental approach for the distance measurement between two NV centers using the Rabi oscillations. Chapter IV provides the experimental methods in acquiring the linewidth narrowing using the rotating field which is applied to ensemble NV centers. The CW ESR experiment and analysis of the results are given. Chapter V details the electron irradiation effect on the bulk diamond where the NV^0 and NV^- ionization fraction and ESR frequency shifts are discussed with respect to the varying electron irradiation dose. Finally, Chapter VI summarizes the dissertation and lays out the future works in improving current results. The additional contributions to the development of NV center imaging, linewidth narrowing experiment, and electron irradiation are provided in this chapter. Through basic proof-of-concept experiments and analysis, the research presented herein can be improved to have higher performance and greater efficiency than this report. Finally, the Appendices detail the theoretical background for the EPR concepts, the optical setup and magnetic resonance hardware, and the microwave circuit fabrication.

CHAPTER II

PHYSICAL CONCEPTS OF NV DIAMOND

2.1 Spin Hamiltonian of NV Center

Optically Detected Magnetic Resonance (ODMR)

The NV center in diamond has triplet ground and excited states as shown in Figure 5. The triplet ground state is the essential property of the NV center and has been well described by many experiments. The ground state is separated into a doublet and a singlet corresponding to $\left|m_s = \pm 1\right\rangle$ and $\left|m_s = 0\right\rangle$ split by 2.87 GHz. The excited triplet state ^{3}E is still explored to better understand the complicated fine structure due to the spin-spin and spin-orbit interactions and the strain in the crystal[41]. There also exists the metastable singlet state ^{1}A to which the electron spins of the NV center escape from the ^{3}E state through intersystem crossing (ISC) [42]. Recently, Manson and his colleagues found that the infrared (IR) emission is attributed to the $^1\text{E}\leftrightarrow{}^1\text{A}$ transition[43].

Once the NV center is optically illuminated, the fluorescence is detected due to the optical transition between the excited triplet state ^{3}E and the triplet ground state ^{3}A and the optical emission spectra show the 637 nm ZPL[29,44]. A simple three level scheme can be used to describe the optical excitation and emission cycle of the NV center[45].

The optically detected magnetic resonance (ODMR) spectrum of the NV center is achieved through the microwave signal frequency sweeping. An electron or nuclear spin in the magnetic field has a small magnetic moment and aligns either with or against any applied field which is designated as spin-up, or spin-down. These two orientations have different energies, and the energy gap between them is proportional to the magnitude of the applied field. Once the levels have been split, the spin resonates with the applied radiation which matches the energy gap. The applied signal is typically called microwave (mw) radiation in the case of ESR and radiofrequency (RF) radiation in the case of NMR. Further splitting of the spin energy levels may arise from local interactions between electronic and nuclear spins such as the hyperfine interaction.

A pulse of resonant microwave radiation flips the spin from one orientation to the other. The superposition of the two eigenstates is generated by varying the microwave pulse length and is described by $\psi(t) = \cos \Omega_{mw} t \left| m_s = \pm 1 \right\rangle + \sin \Omega_{mw} t \left| m_s = \pm 1 \right\rangle$ where Ω_{mw} is the microwave Rabi frequency depending on the applied microwave field intensity[46].

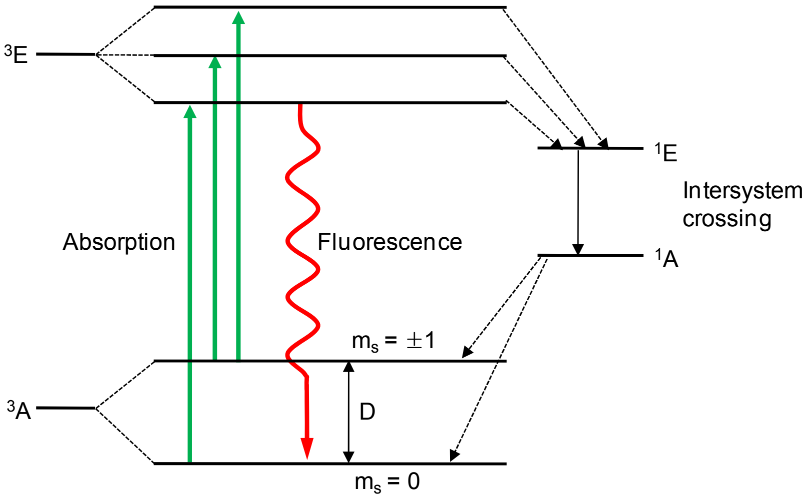

Figure 5. The energy level diagram of electronic states of NV center. The ground state is triplet ^3A with the splitting between degenerated upper level $m_S = \pm1$ and lower level $m_S = 0$ being about 2.87 GHz. The upper levels are singlet ^1A and triplet ^3E.

Spin Hamiltonian

The Hamiltonian for the electron spin S=1 of the NV ground state with neglecting hyperfine effects can be defined as[47,48]

$$H = g\beta_e \mathbf{B}^{\mathrm{T}} \cdot \mathbf{S} + \mathbf{S}^{\mathrm{T}} \cdot \mathbf{D} \cdot \mathbf{S} \tag{2}$$

with the electronic g-factor, $g = 2.0028$, the Bohr magnetron, $\beta_e = 9.2740 \times 10^{-24}\,\mathrm{J/T}$, the external magnetic field B, and the zero-field splitting tensor $D = 2.87\,\mathrm{GHz}$[31]. For the C_{3v} trigonal symmetry with the zero-field splitting, the spin Hamiltonian in the principal axis system is given by

$$H = g_e\beta_e \mathbf{B} \cdot \mathbf{S} + D[S_z^2 - \tfrac{1}{3}S(S+1)] + E[S_x^2 - S_y^2] \tag{3}$$

where the principal axes (X, Y, and Z) are chosen with respect to the crystallographic axis system (X', Y', and Z') [see Figure 6][49]. When the external magnetic field is parallel to the quantization axis of the electron spins, i.e. $B \,||\, Z$ where the Z axis is along the [111] direction, the electron Zeeman splitting depends linearly on the magnetic field strength. At about 1024 Gauss of magnetic field along the NV quantization axis, a level anti-crossing (LAC) occurs between $m_s = -1$, and $m_s = 0$ state [Figure 7][50].

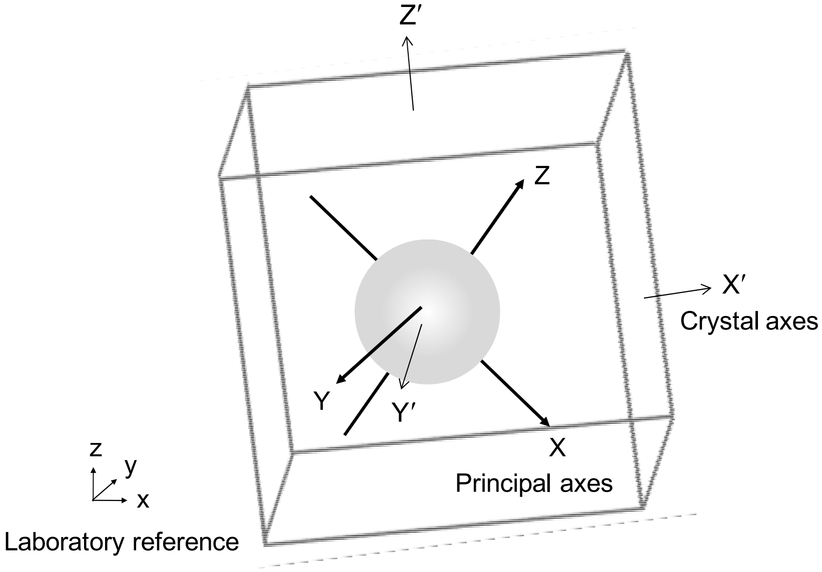

Figure 6. The schematic diagram plots the three different sets of coordinates. The laboratory axes (x, y, z) are fixed for the sake of reference. The crystal axes labeled (X′, Y′, Z′) are the orthogonal set of axes in bulk diamond. For the purpose of obtaining the symmetry for the paramagnetic species, the principal axes (X, Y, Z) which are the same as the diagonalized crystal axes are used.

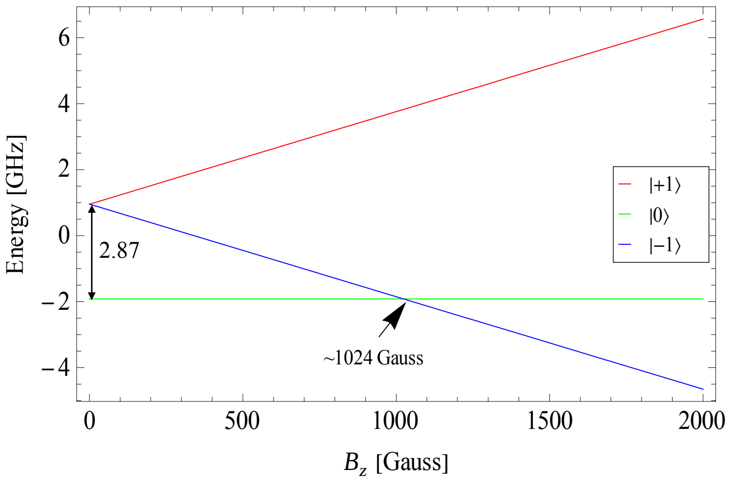

Figure 7. Zeeman splitting of the NV center with E = 0 and B||Z in the C_{3v} symmetry.

Hyperfine Coupling

In EPR, the unpaired electron interacts with neighboring nuclear dipole moments and this results in the splitting of resonance which is called nuclear hyperfine interaction or splitting. The hyperfine interaction may be either dependent (anisotropic) or independent (isotropic) on the orientation of the external magnetic field with respect to a molecular axis. In a diamond, the hyperfine structure of nitrogen is much easier to observe than that of ^{13}C in EPR since ^{14}N ($I = 1$) is nearly 100% abundant. The nitrogen hyperfine parameters are very accurately known and it has been determined that there is small unpaired electron probability density on the nitrogen atom, and the unpaired electrons are almost entirely localized on the three neighboring carbon dangling orbitals[51].

The nuclear spin Hamiltonian of ^{14}N is given by[40,52,53]

$$H_N = \mathbf{S}^{\mathrm{T}} \cdot \mathbf{A} \cdot \mathbf{I} + \mathbf{I}^{\mathrm{T}} \cdot \mathbf{P} \cdot \mathbf{I} = A_{\parallel} S_z I_z + A_{\perp}(S_x I_x + S_y I_y) + P(I_z{}^2 - \frac{1}{3} I(I+1)) \tag{4}$$

where $I = 1$ is the nitrogen nuclear spin, $S = 1$ is the NV center electron spin, $A_{\parallel} = 2.3$ MHz and $A_{\perp} = 2.1$ MHz are the hyperfine constants parallel and perpendicular to the defect axis, [111], and $P \approx -5.04$ MHz is the quadrupole splitting constant. The intimate view at close range around the $m_s = +1$ or $m_s = -1$ transition shows the resonances corresponding to the three ^{14}N nuclear spin sublevels[54]. This hyperfine interaction observed with ESR provides a measurement of $A_{\parallel}$ = 2.3 MHz.

If the ^{15}N which is naturally 0.1% abundant is implanted to the diamond, the ODMR spectrum corresponding to the ^{15}N is different from that of the 14N[55]. Similarly, for the 1.1% abundant ^{13}C nucleus, a clearly different hyperfine coupling is measured. The ODMR measurements show that the ^{13}C nucleus produces ~130 MHz hyperfine coupling parameter[56,57]. In Figure 8, the energy level diagrams of the NV center coupled to the different nuclei are plotted.

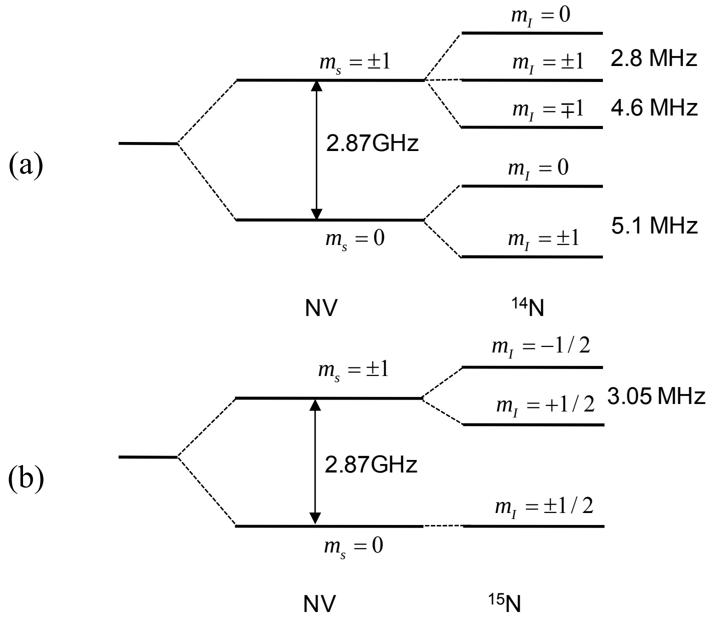

Figure 8. Hyperfine structure for the NV electron spin (a) with ^{14}N and (b) coupled to the ^{15}N nuclear spin with the calculated hyperfine splittings.

2.2 Rabi Oscillation

Once the NV center is excited using the 532 nm green laser, the electron spin of an NV center is polarized into $m_s = 0$ of the ground state[46,58,59] and the microwave signal is applied to manipulate the electron spin state. When the applied microwave field is tuned to the resonance frequency, i.e., 2.87 GHz, the optical measurement shows the spin transition between $m_s = 0$ and $m_s = \pm 1$ which consists of a simple two level system.

If the external magnetic field causes the Zeeman splitting of $m_s = \pm 1$ state, two resonance frequencies corresponding to the transitions $m_s = +1 \leftrightarrow m_s = 0$ and $m_s = -1 \leftrightarrow m_s = 0$ are observed. The resonant microwave driven oscillations in the spin population between two states are known as Rabi oscillation[60,61]. In the two level system, the Rabi frequency is given by $\Omega_R = \mu B / h$ where μ is the transition dipole moment, B is the applied magnetic field, and h is the Planck's constant.

Figure 9 shows the pulse sequence for the Rabi oscillation where the duration of mw pulse, τ, varies and the population remaining in $m_s = 0$ is measured. The Rabi frequency Ω_R is proportional to the square root of the microwave power $\sqrt{P_{mw}}$ [Figure 10]. Practically, the Rabi frequency is doubled by increasing the mw power by a factor of 4.

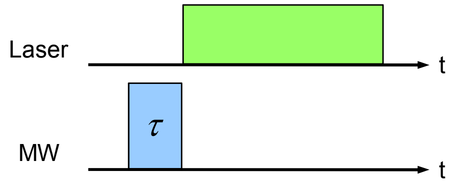

Figure 9. The pulse sequence for the Rabi oscillation is depicted. The population in m_S=0 is measured as the microwave duration τ varies. The whole sequence repeats to average the fluorescence signal in the time-domain of the experiment.

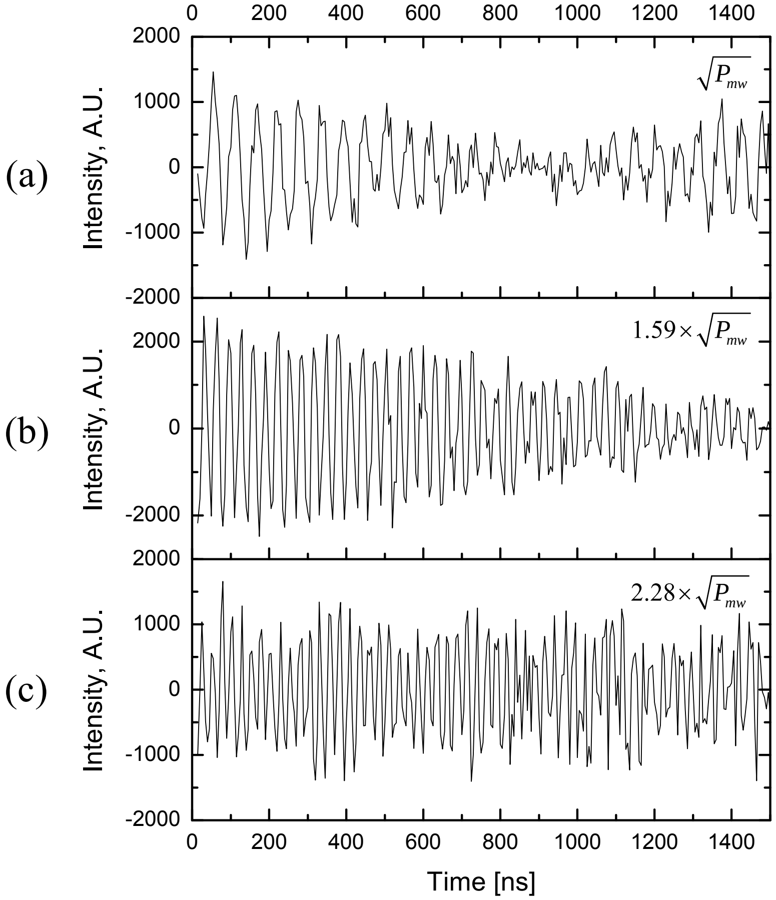

Figure 10. The Rabi oscillations are measured using varying microwave powers of which square root values are (a) $\sqrt{P_{mw}}$, (b) $1.59\times\sqrt{P_{mw}}$, and (c) $2.28\times\sqrt{P_{mw}}$. The calculated Rabi frequencies are 17.81 MHz, 31.71 MHz, and 39.31 MHz, respectively and they are approximately linear with respect to the square root of the microwave power.

2.3 Spin Relaxation Time and Linewidth

Linewidth

If the magnetic field B is taken along the Z axis (B||Z) in Equation 3, the energies can be expressed by

$$E_{\pm} = \tfrac{1}{3}D \pm g\beta_e B$$
$$E_0 = -\tfrac{2}{3}D \tag{5}$$

where $E = 0$ due to the C_{3v} symmetry. The transition $E_{\pm} \leftrightarrow E_0$ between two levels complying with the selection rule $\Delta m_s = \pm 1$ can be induced by the microwave radiation $h\nu_{\pm}$ as below:

$$\nu_{\pm} = D \pm g\beta_e B / h \tag{6}$$

The Heisenberg uncertainty relation can be expressed by[62,63]

$$\Delta\nu \cdot \Delta t = g\beta_e \Delta B / h \approx 1/2\pi \tag{7}$$

where $\Delta\nu$ is the electron spin linewidth and Δt is the electron spin lifetime. Since the lifetime Δt is determined by $1/\Delta t \approx 1/T_1 + 1/T_2$ where T_1 and T_2 are the spin-lattice relaxation time and the spin-spin relaxation time, respectively, the Equation 2-7 becomes

$$\Delta\nu \approx 1/(2\pi T_1) + 1/(2\pi T_2) \tag{8}$$

Usually since $T_1 \gg T_2$, e.g., $T_1 = 10^2$ to 10^4 s and $T_2 = 1.8$ ms for the ultrapure CVD diamond grown by the state-of-the-art technology[64], the electron spin linewidth $\Delta\nu$ is simplified to

$$\Delta\nu \approx 1/(2\pi T_2) \tag{9}$$

Broadening

The electron spin linewidth $\Delta\nu$ is generally dependent on the spin-lattice and spin-spin relaxation times. If the linewidth broadening is dominated by T_1 and T_2, it is called the homogeneous broadening. But if the broadening is originated by other causes such as the inhomogeneous g-factor and magnetic field and the hyperfine anisotropy, it is called the inhomogeneous broadening.

Spin Relaxation Times: T_1 and T_2

The spin-lattice or longitudinal relaxation time T_1 is the time over which the spin system forced out of equilibrium returns to the thermal equilibrium through the energy transfer to the surrounding lattice. In order to measure T_1, the inversion recovery sequence composed of two pulses is used [Figure 11][65].

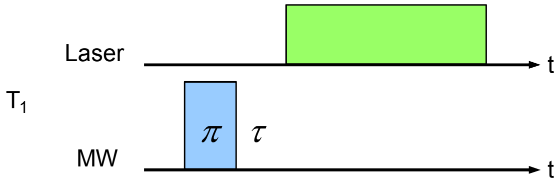

Figure 11. The inversion recovery pulse sequence is displayed to measure the T_1 time.

The spin-spin or transverse relaxation time T_2 is the time for dephasing in the x-y plane. The electron spin echo (also known as Hahn echo) is most widely used to measure the T_2 in ESR experiments[52]. Figure 12 shows the spin-echo pulse sequence which consists of the sequence $\pi/2-\tau_1-\pi-\tau_2-\pi/2$ where the π pulse is the microwave duration to flip the electron spin from $m_s=0$ to $m_s=\pm1$ and τ_1 and τ_2 are durations of free precession.

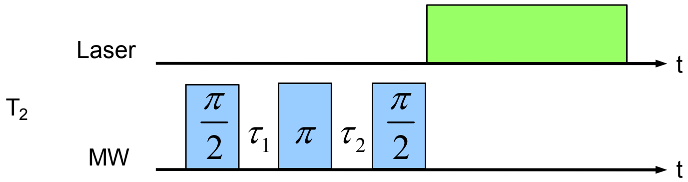

Figure 12. The spin-echo pulse sequence is depicted to measure the spin-spin relaxation time.

Spin Dephasing Rate, T_2^*

The spin dephasing rate T_2^* is a measure of the inhomogeneous electron spin linewidth broadening. T_2^* can be measured simply by the microwave signal sweeping or by the free induction decay (FID) sequence [Figure 13]. In diamond with a high nitrogen concentration such as HPHT diamond, the each spin in the ensemble NVs experiences the dipole-dipole coupling causing the spin linewidth broadening. The magic angle spinning (MAS) is one method to reduce the dipolar broadened line, thus, eliminate T_2^* or T_2 and reach the T_1 limit.

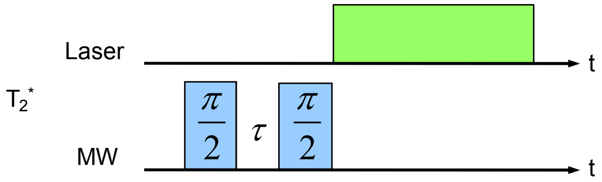

Figure 13. The free induction decay (FID) sequence is depicted for the spin dephasing time T_2^* measurement.

CHAPTER III

TWO DIMENSIONAL DISTANCE MEASUREMENT OF NV CENTER USING THE EPR IMAGING (EPRI)

3.1 Introduction

The nitrogen vacancy (NV) center in diamond is an electron paramagnetic species and has many applications, such as quantum computing[15, 66] and magnetic sensor [67] due to its electron paramagnetic resonance (EPR) properties. Recent experiments pronounce that the NV center can be a good probe enabling the bio-cell imaging and biomolecular tracking due to a low photobleaching and a low toxicity[68,69]. The electron spin resonance (ESR) is a useful means to identify the NV center in a bulk crystal or in bio-cells since the EPR imaging (EPRI) methods have been developed to achieve the spatial resolution in molecules[70].

Recently Balasubramanian *et al* demonstrated nanoscale imaging using the single electron spin of NV center in a nanodiamond[16]. They measured the ESR signal using the optical detection and calculated the magnetic field resulting from the magnetic material coated AFM tip and the nearby magnetic particle such as an electron. According to their measurement, it turned out that the spatial resolution of down to 5 nm was able to be obtained. In the other scanning microscopy to obtain the distribution without a magnetic field, Hell and his coworkers developed the stimulated emission depletion (STED) microscopy as a good competitor for the confocal microscopy, and improved the focal plane resolution down to 15–20 nm resolution [71,72,73].

Even though the specific techniques used in different EPR imaging vary, the principle of EPRI experiments is described by the change in the resonance frequency at the adjacent position as $\nu_e(\mathrm{MHz}) = g\beta_e B / h \approx 28 \cdot \frac{g}{g_e} B(\mathrm{mT})$ where ν_e is the microwave frequency, g_e and g are the g-factors of the free electron and the interacting electron with the surrounding particles, h is the Plank constant, and the applied magnetic field $B = (B_{res} + x \cdot \partial B_x / \partial x)$ is the field at the position x which is varied by the gradient field $\partial B_x / \partial x$ along the x axis from the resonance field B_{res} [74]. Using this equation, the distance between two adjacent paramagnetic species can be calculated experimentally as the existence of visually irresolvable particle is verified.

In the confocal microscopy, the 2D EPR spectroscopy has been performed to show the distribution of the NV center [75]. Besides, the STED microscopy has a dead area where the closely overlapped 'phantom' NV center cannot be resolved. In order to overcome the limitation of 1D EPRI and suggest an approach for the 2D EPRI beyond phantoms, the Rabi oscillation which is based on the spin dynamics of the NV center is measured using the pulsed electron spin resonance (ESR) in this experiment.

3.2 Theoretical Background

Spin Hamiltonian for Two Unpaired Electrons

For the system composed of two unpaired electrons with the magnetic field **B** applied along the z axis which is along the quantization axis of the NV center, i.e., the [111] orientation [Figure 14(a)], the spin Hamiltonian becomes

$$\begin{aligned} H &= g\beta_e \mathbf{B}^T \cdot \mathbf{S} + \mathbf{S}^T \cdot \mathbf{D} \cdot \mathbf{S} \\ &= g\beta_e B_z S_z + D[S_z^2 - \tfrac{1}{3} S(S+1)] + \tfrac{1}{2} E(S_+^2 + S_-^2) \end{aligned} \tag{10}$$

with zero-field tensors, $D = \frac{3}{2} D_z$ and $E = \frac{1}{2}(D_x - D_y)$. Summarizing the Hamiltonian in the basis set of $|+1\rangle$, $|0\rangle$ and $|-1\rangle$ of S_z, the spin Hamiltonian matrix is given by

$$\begin{pmatrix} g\beta_e B_z + \dfrac{D}{3} & 0 & 0 \\ 0 & -\dfrac{2}{3} D & 0 \\ 0 & 0 & -g\beta_e B_z + \dfrac{D}{3} \end{pmatrix} \tag{11}$$

with $D = 2.87$ GHz and $E = 0$. The calculation of the secular equation gives the energy set below:

$$-\tfrac{2}{3} D \quad \text{and} \quad \tfrac{1}{3} D \pm g\beta_e B_z \tag{12}$$

and they are plotted in Figure 14(b) as the magnetic field $B \parallel z$ increases. Among the transition indicated by arrows, the electron resonant transition of $\Delta m_S = \pm 1$ is allowed by the selection rule.

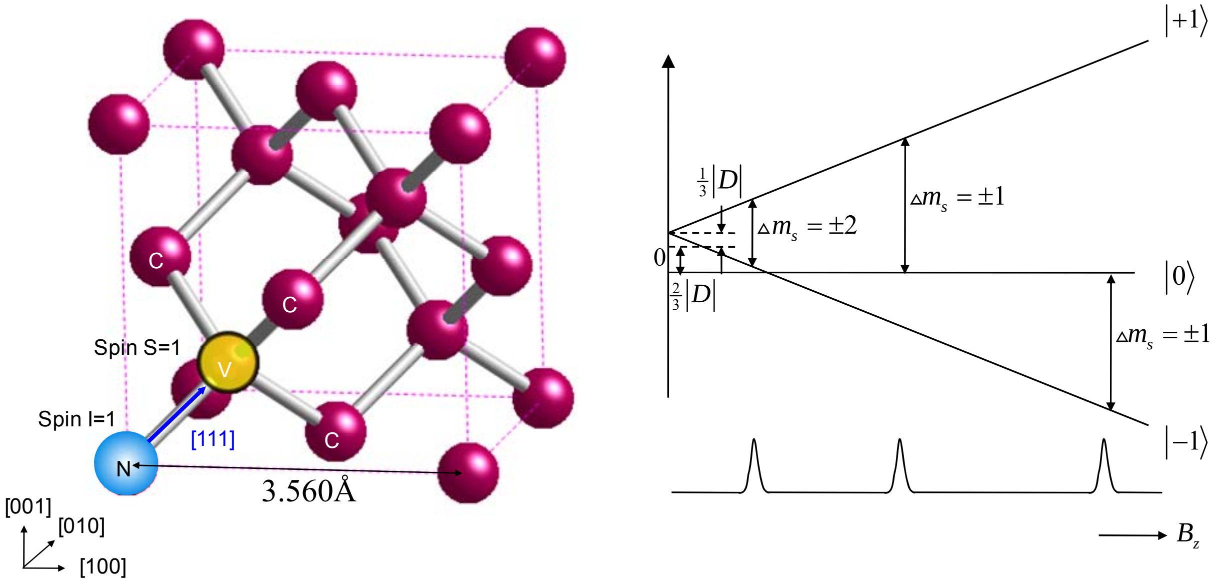

(a) (b)

Figure 14. (a) The lattice structure of the NV center in diamond is depicted. (b) The triplet state energies as a function of magnetic field (B||z) for D>0 and E=0 is displayed.

Rabi Oscillation

The Rabi frequency is defined as

$$\Omega_R = |\mu B| / h \tag{13}$$

where μ is the magnetic moment, h is the Planck constant, and B is the applied magnetic field. In the two level system composed of $|m_s = \pm 1\rangle$ and $|m_s = 0\rangle$ of the NV center, the Rabi oscillation is given by $\Omega_R = g\beta_e B / h$.

3.3 Materials and the Method

Thanks to the progress in the microfabrication technology, the explosive development has been made in atomic physics[76]. The micronscale electromagnet fabricated using the photolithograph and plating techniques performed successfully to generate the magnetic field up to 0.3T for atom manipulation[77]. The micron-size resonators of 200–500 μm were used for the pulsed EPR experiment to measure the FID as well as CW EPR experiment[78]. Their measurements found that the sensitivity of the resonator is inversely proportional to the size of the micronresonator. The micronscale structure created with the lithography and fabrication techniques is also proposed for NMR[79].

In this experiment, the diamond sample is a (100) cut type-Ib crystal (Element Six) in which many natural NV centers exist. In order to apply the microwave signal, the photolithography using the UV laser was utilized to produce the thin gold wire. The photoresist was spin-coated on the surface of the diamond substrate and was baked at 110˚C. After illuminating the UV light through the mask, the micronscale pattern was developed on the Ti and Au deposited surface. Subsequently, the gold plating was performed to make a thick pattern and the sacrificial layers of gold and Titanium were etched. In Figure 15, the 3–4 μm thick gold wires are separated by 4.8 μm at the central area.

Figure 15 shows the gold wires of which four inner wires are used to apply the microwave signal to manipulate the electron spin of the NV center in diamond. The advantage of fabricating the micronscale structure on the surface of the small diamond is that the higher magnetic field is acquired in the vicinity of the NV centers that are located underneath the surface. By removing the gap between the diamond substrate and the external wire or structure, the steep gradient field is obtained on the micron-size area with the reasonable microwave power or DC current.

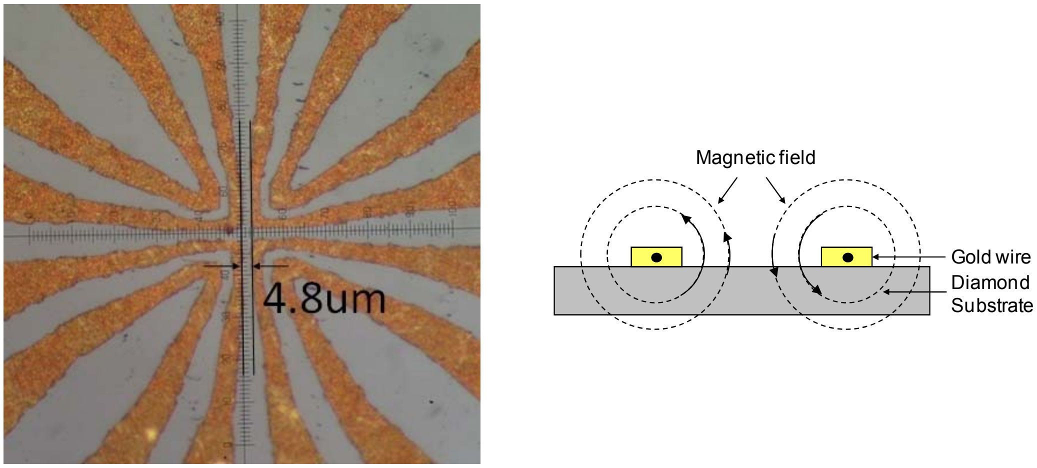

(a) (b)

Figure 15. (a) The ~3 μm thick gold wires are fabricated on top of the (100) cut type-Ib diamond surface. The four wires surrounding the center are used to apply the microwave signal to generate the magnetic field. (b) If the current flows in the same direction through two wires, the wire pair can generate the larger gradient field.

3.4 Simulation

Magnetic Field Simulation

Modeling the magnetic field generated by gold wire is one of the key methods for two-dimensional imaging. From the simulation, it turned out that the two wires placed at the diagonal positions [Figure 16] produce the symmetric field at the central area when they carry the microwave signals in the same direction [Figure 17(a)]. Figure 16 shows the two pairs of wire to make the symmetric fields. In order to calculate the magnetic field at each position, the magnetic field distribution should be simplified and modeled. But the 2D field modeling to obtain the field intensity and orientation is very complicated compared to the 1D distribution since the field vector and amplitude show the quadratic distribution such as ax^2+bx+c [Figure 17(b) to (d)]. Instead the 3D mapping on the simulation software (HFSS, Ansoft) was used for this experiment to facilitate the analysis.

Rabi Frequency for Different Orientations

In the crystal structure of diamond, there exist four different orientations of the NV center. The quantization axes of the NV center are inclined with respect to the [100] crystallographic axis by 54.7° and 125.3°. When the resonant microwave signal is applied to the bulk diamond, the Rabi oscillation is observed. When the field acting on the NV center is randomly oriented, the effective field which is the projection of the magnetic field onto the xy plane should be taken into account for the Rabi oscillation, $\Omega_R = |\mu B| / h$.

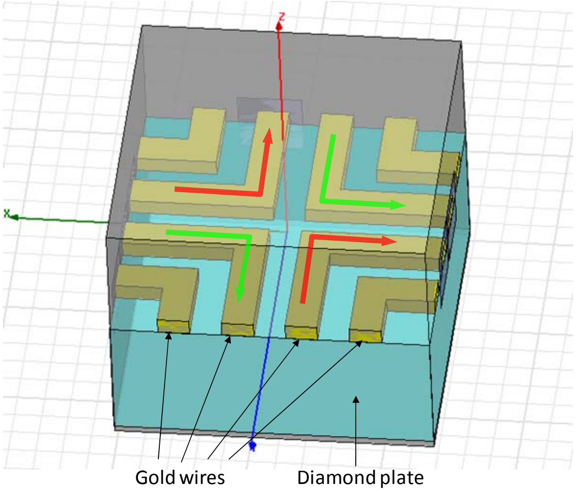

Figure 16. The simulation model for the field distribution is plotted using the commercial 3D finite element method (FEM) simulator (HFSS). The gold wires are placed on top of the bulk diamond. The red and green colored two pairs of wire are excited using the one Watt microwave signals at the same time.

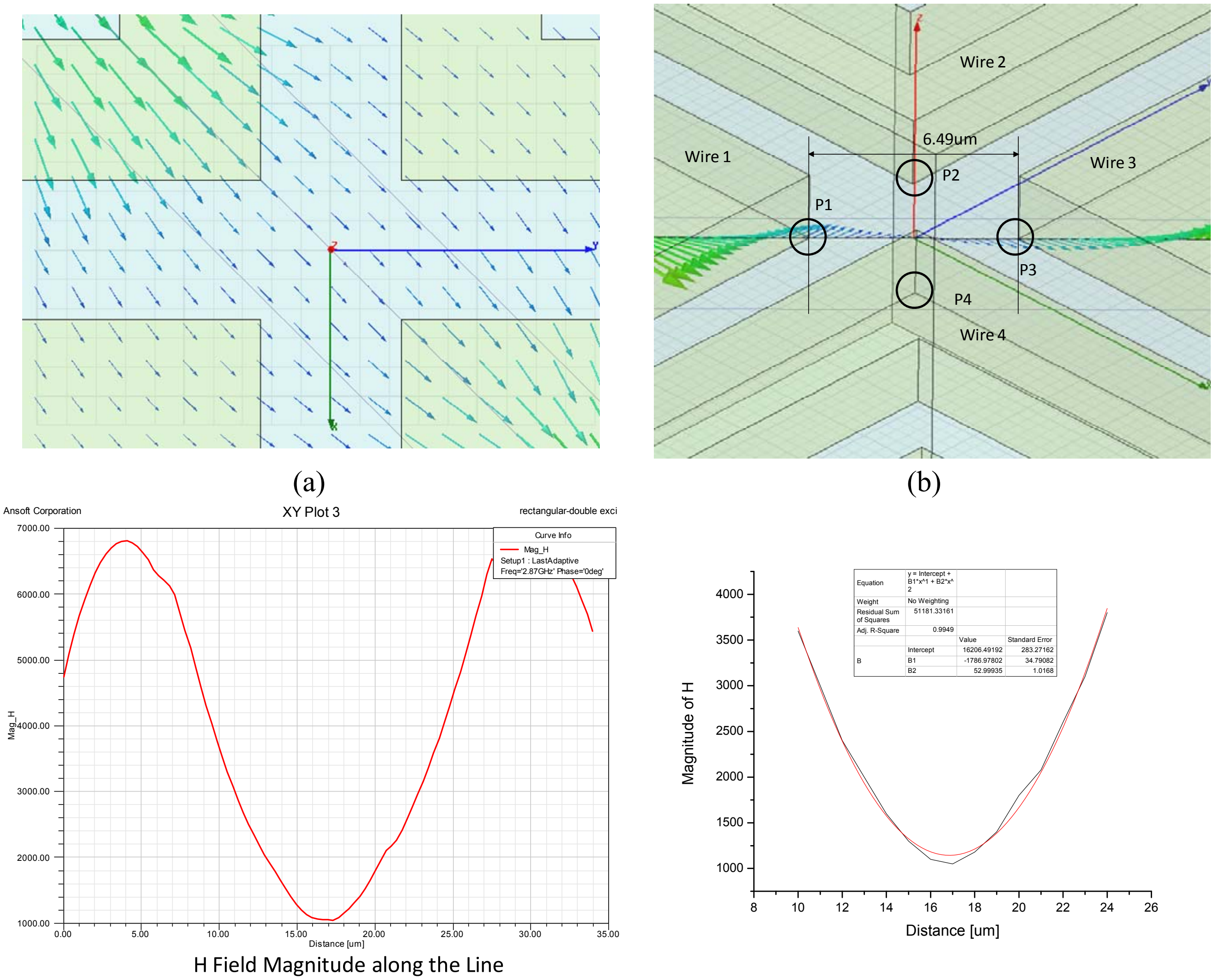

Equation	y = Intercept + B1*x^1 + B2*x^2		
Weight	No Weighting		
Residual Sum of Squares	51181.33161		
Adj. R-Square	0.9949		
		Value	Standard Error
B	Intercept	16206.49192	283.27162
	B1	-1786.97802	34.79082
	B2	52.99935	1.0168

(a) (b)

(c) (d)

Figure 17. (a) The top view of the structure is illustrated. The calculated field distribution between two wires is symmetric on the top surface of the diamond. (b) The H field vector is plotted along the line connecting two points, P1 and P2. (c) The magnitude of the H field is plotted. (d) The fitting curve shows that the magnetic field intensity is quadratic along the line.

For the random orientation of the magnetic field, the estimated Rabi frequency is given by

$$\Omega_R\,(\text{MHz}) = g\beta_e \mathbf{B}_\perp / h \approx 2.8B\sin\theta\,(Gauss) \tag{14}$$

where $\mathbf{B}_{\perp}$ is the perpendicular field to the static magnetic field $\mathbf{B}_z$ and θ is the angle between the random magnetic field $\mathbf{B}$ and $\hat{\mathbf{n}}_{\mathrm{i}}$, the unit vector along each quantization axis of the NV center with i = 1, 2, 3, and 4.

3.5 Results

The scanned fluorescence image of the diamond surface is shown in Figure 18. The bright regions on the four corners are the gold wires and the NV centers are located between them. It was found that the natural NVs in the type Ib diamond have a few different orientations and are the mixture of single and multiple impurities. Among many NVs, NV7 and NV12 are preferred since they are the same orientation. They are located at the center, therefore the random effects due to the imperfection of the structure seems to lessen.

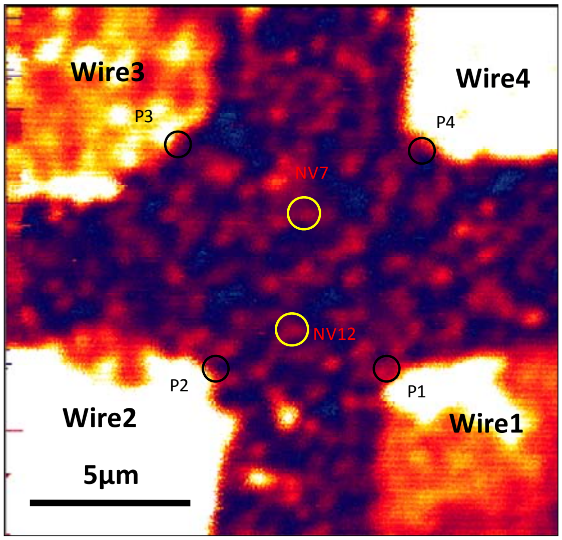

Figure 18. The scanned fluorescence image shows the NV centers at the center. They are surrounded by four wires for the microwave excitation which are characterized by the bright regions.

Once the image is obtained, the continuous wave electron spin resonance (CW ESR) spectrum is scanned using the microwave signal frequency sweeping in order to the resonant frequency for each NV center. In Figure 19, the CW ESR measurements show that NV7 and NV12 may be single NVs since they display one dominant dip which is split using the DC magnetic field (~35 Gauss) controlled by the electromagnet. For two different combinations of wires, the ESR measurements show the similar spectra around 2.770 GHz.

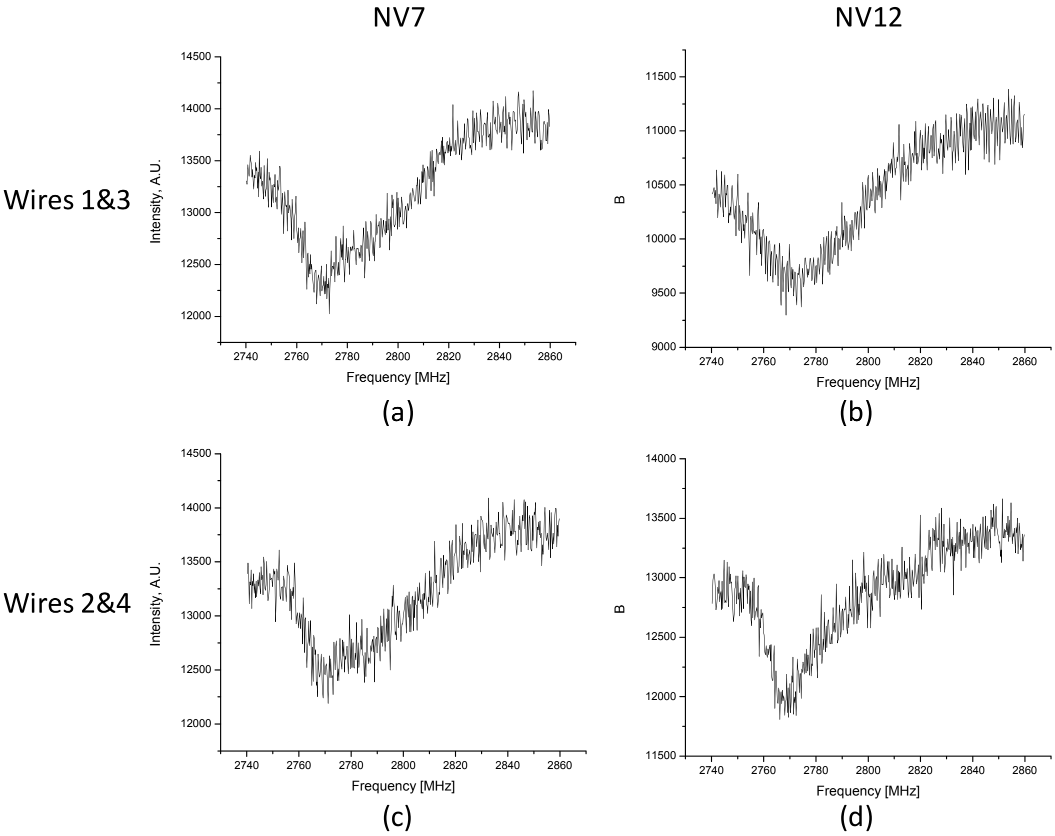

Figure 19. (a), (b), (c), and (d) The CW ESR measurements show the single dips for NV7 and NV12 when the two different wire pairs are excited with the same microwave power.

If the microwave signal is tuned to the resonant frequency at which the transition between two electron spin states, $\left|m_s=-1\right\rangle$ and $\left|m_s=0\right\rangle$, occurs, the pulse experiment for the Rabi frequency is performed. As the microwave signal duration, τ, varies from 5 ns to 2500 ns in the step of 5 ns, the laser is turned on for ~3 μs and off in sequence to collect the fluorescence [Figure 20(a)]. Using the signal process for the temporal data sequence, the Rabi oscillations are plotted for two wire pairs and two NVs in Figure 20(b) to (e).

Figure 21 shows the transformed Rabi oscillations in the frequency domain using the fast Fourier transform (FFT). In Figure 21(a) and (b), single frequencies are observed for NV7 and NV12 when the field caused by the microwave signals which are applied to the wires 1 and 3 is applied. On the other hand, when the microwave signals are applied to wires 2 and 4, NV7 shows one dominant and another weaker frequencies while NV12 has a single frequency.

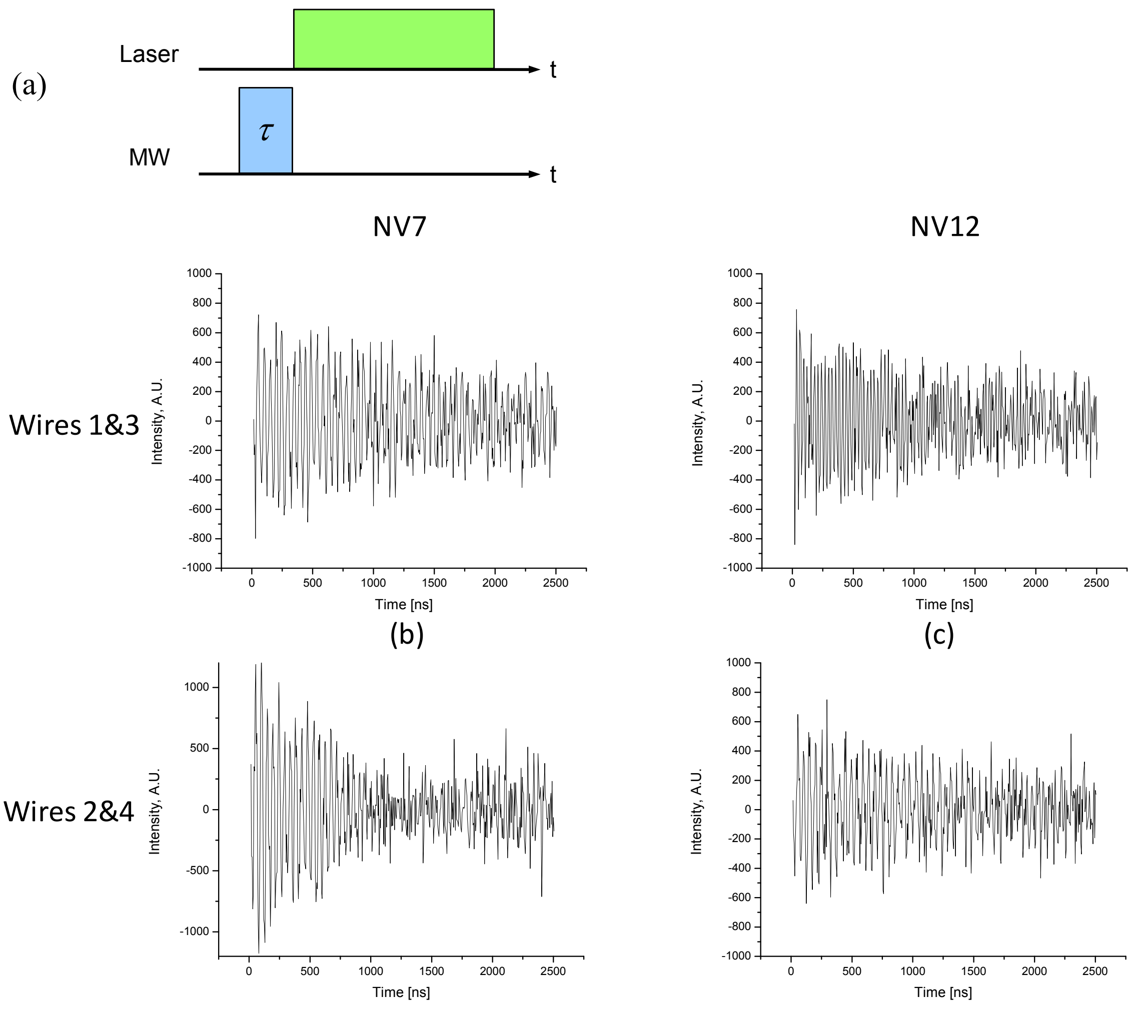

(b) (c)

(d) (e)

Figure 20. (a) The pulse sequence to measure the Rabi oscillation is depicted. The microwave signal varies during the microwave duration, τ and the laser is turn on and off in sequence. (b), (c), (d), and (e) The Rabi oscillation measurements are plotted in the temporal sequence after the signal processing.

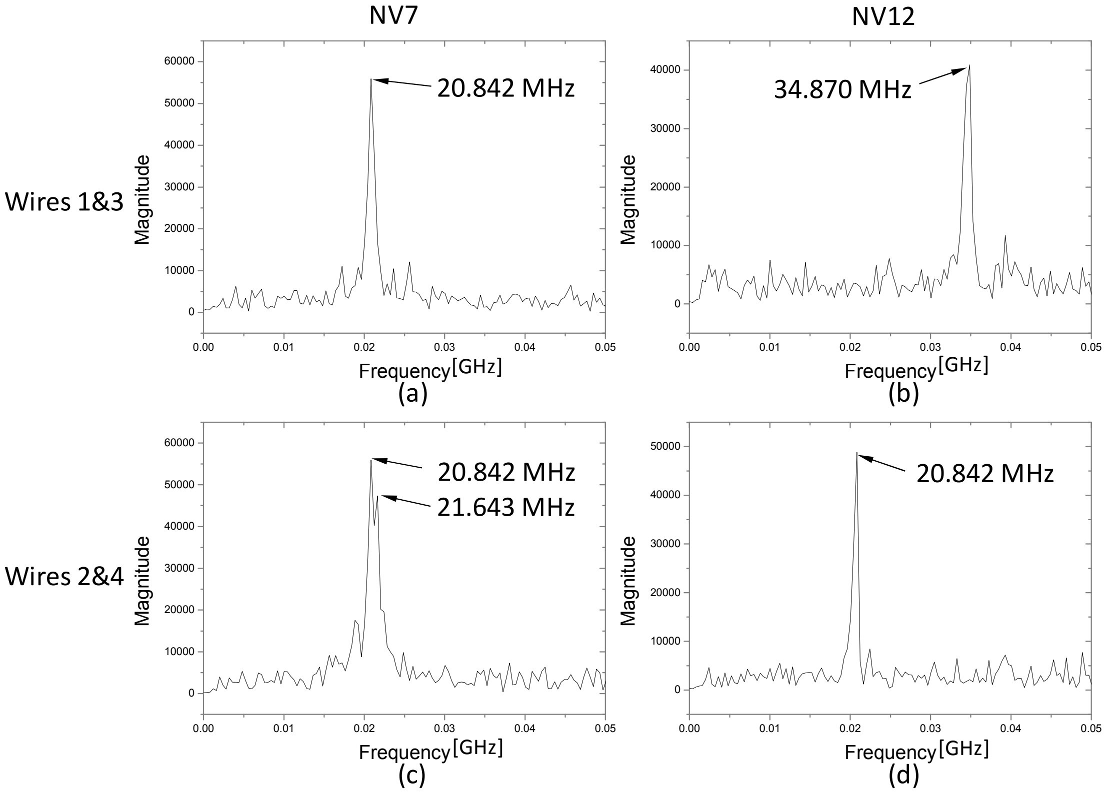

Figure 21. (a), (b), (c), and (d) The transformed Rabi oscillation measurements are displayed in the frequency domain using the FFT method. The spectra for NV7 and NV12 show the single frequencies using the wire 1 and 3 pair while they show the two frequencies for NV7 and one dominant frequency for NV12 using the wire 2 and 4 pair.

Rotating of the Coordinates

The diamond sample used for this experiment is the (100) cut crystal [Figure 22(a)] but for the orientations of four sides, there exists mismatch between the laboratory reference axes and the crystal axes. The approach to settle the conflict in different coordinate systems is to rotate the xy plane which is perpendicular to the [100] direction. Using the rotation matrix given by

$$\begin{pmatrix} x' \\ y' \end{pmatrix} = \begin{pmatrix} \cos\phi & -\sin\phi \\ \sin\phi & \cos\phi \end{pmatrix} \begin{pmatrix} x \\ y \end{pmatrix} \tag{15}$$

where ϕ is the varying angle with respect to the laboratory reference, the crystal axes are rotated as shown in Figure 22(b) and (c) while the Rabi frequencies for NV7 and NV12 are calculated.

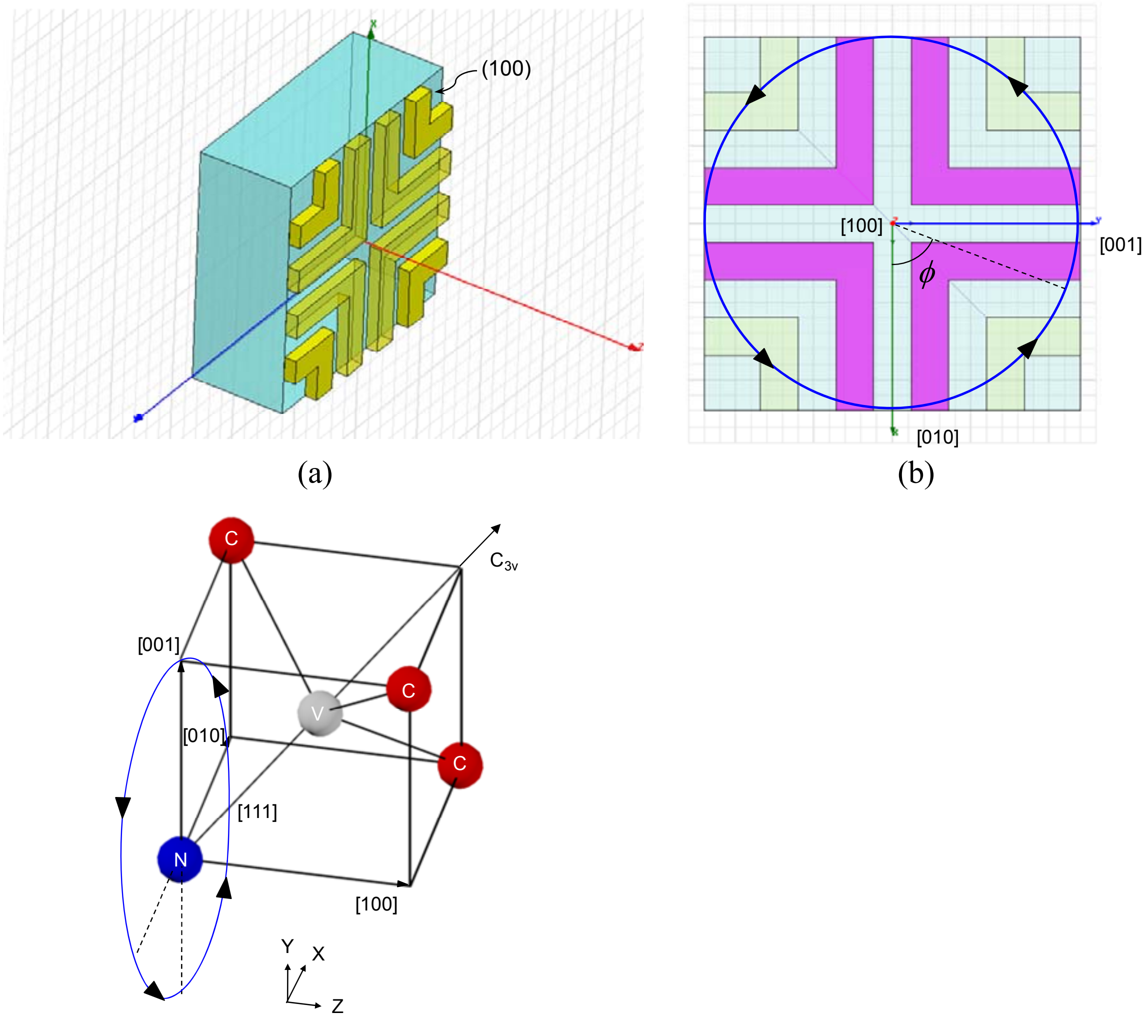

(a) (b)

(c)

Figure 22. (a) A (100) cut type Ib diamond was used for this experiment but there exists the mismatch between the laboratory reference axes and the crystal axes. (b) and (c) In order to the mismatch in the coordinate systems, the rotation matrix is applied to rotate the xy plane in the crystal coordinate system where the angle, ϕ, varies.

For each wire pair, the Rabi frequencies for NV7 and NV12 were calculated using the field intensity and orientation from the simulator. Along with the constant ratio of calculated and measured Rabi frequencies, Ω_c / Ω_m, for each wire pair, the corresponding curves for NV7 and NV12 should have a crossing point at the same rotation angle for two wire pairs. The numerical analysis was performed at different rotating angles for four NV orientations [Figure 23]. The calculation of Ω_c / Ω_m in Figure 24 shows that whichever orientation the NV7 and NV12 have, the ratio is ~1.377 and the 3D field mapping on the simulator gives the reliable field intensity and orientation.

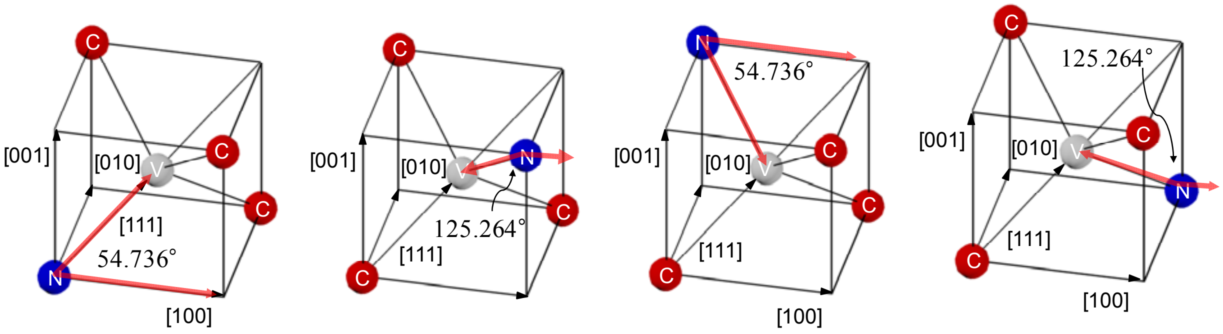

(a) (b) (c) (d)

Figure 23. Four different orientations of the NV quantization axis are depicted. The orientations 1, 2, 3, and 4 at (a), (b), (c) and (d), respectively are oriented at the angles, 54.7° and 125.3°, with respect to the [100] axis.

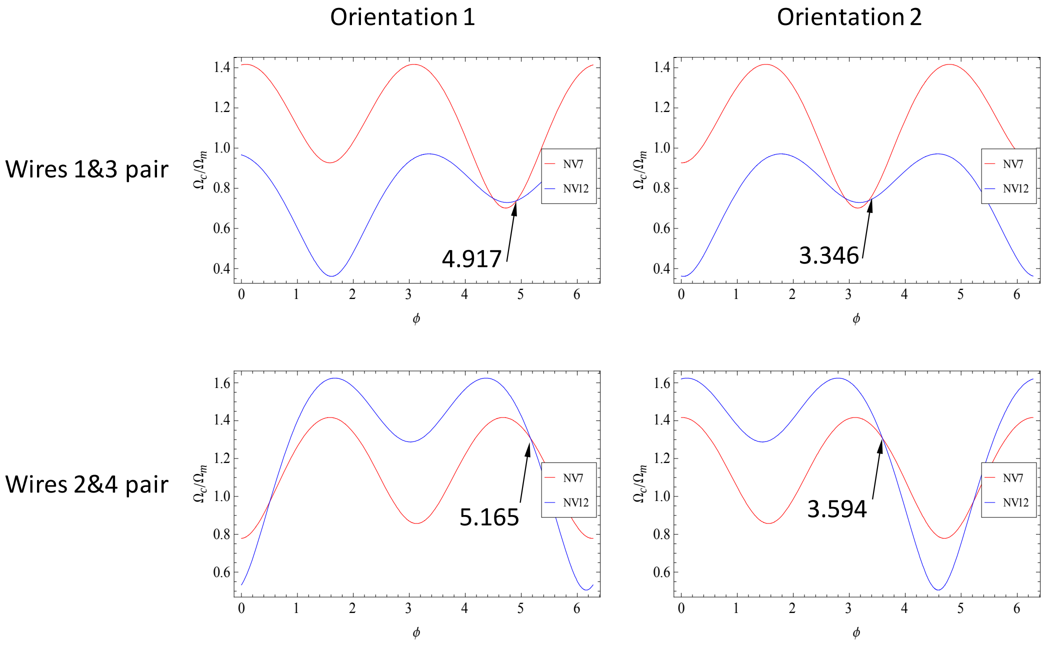

(a) $\Delta\phi$ =.248, ϕ_{avg}= 5.041
$\Omega_c/\ \Omega_m$ =1.3769 for wires 2&4 pair

(b) $\Delta\phi$ =.248, ϕ_{avg}= 3.470
$\Omega_c/\ \Omega_m$ =1.377 for wires 2&4 pair

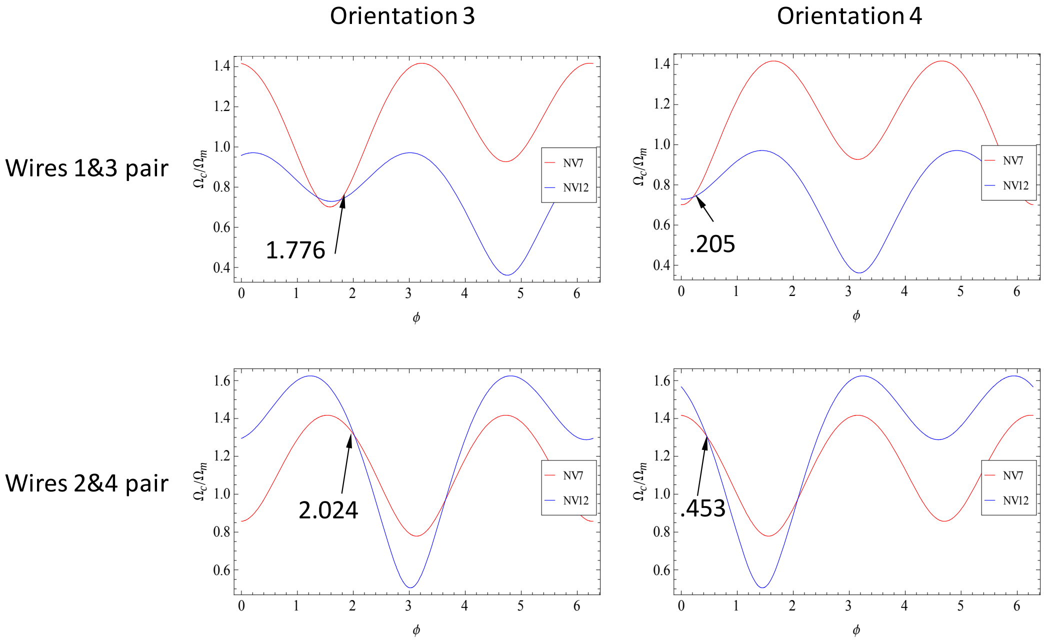

(c) $\Delta\phi$ =.248, ϕ_{avg}= 1.9
$\Omega_c/\ \Omega_m$ =1.3766 for wires 2&4 pair

(d) $\Delta\phi$ =.248, ϕ_{avg}= 0.329
$\Omega_c/\ \Omega_m$ =1.3767 for wires 2&4 pair

Figure 24. (a), (b), (c), and (d) The measured and calculated Rabi frequencies ratio, Ω_m/Ω_c is obtained as the rotation angle ϕ is scanned. The plots show that the crossing of two curves occurs at the different rotation angle ϕ but the ration is the same for different orientations.

Distance Calculations

Since the single dip was observed in the CW ESR spectrum of NV7 but two Rabi frequencies were measured, it is expected that double NVs in the same electron spin orientation are located at the site of NV7. For the same orientated NVs, the quadratic field distribution should be formulated to calculate the distance. The magnetic field intensity along the shifted P2′- P4′ line on the same depth of NV7 [Figure 25] is given by

$$B = a(r - r_0)^2 + b \tag{16}$$

where r_0 is the center point of the symmetry and the variables a and b can be obtained using the field distribution of the simulator in the factor of 1.377 [Figure 26]. For two Rabi frequencies, the frequency difference is achieved by

$$\Delta\Omega = 2.8 \cdot 4\pi \cdot 10^{-3} \cdot a[(r_1 - r_0)^2 - (r_2 - r_0)^2]/1.377 \tag{17}$$

where r_1 and r_2 are two NV positions. Using this equation, the calculated distance between double NVs is 713.16 nm with no change in the orientation of the second NV as shown in Figure 27.

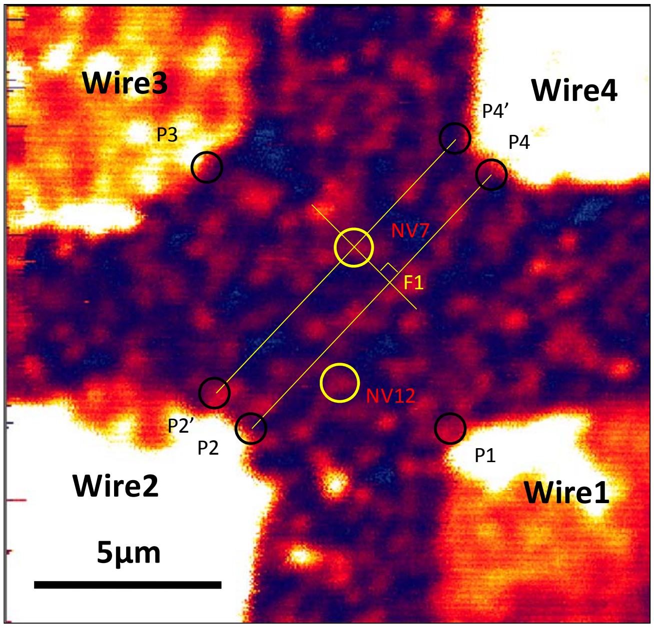

Figure 25. P2′ and P4′ are shifted parallel to the P2-P4 line. The filed distribution should be obtained to calculate the distance between two NVs.

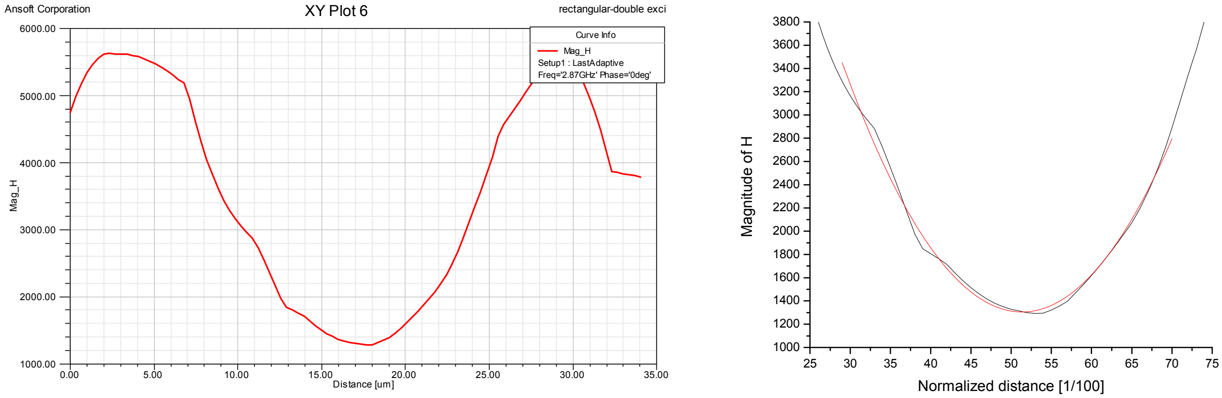

(a) (b)

Figure 26. (a) The quadratic field intensity distribution was obtained from the simulator. (b) The curve fitting shows a=22.10 A/m·µm^2.

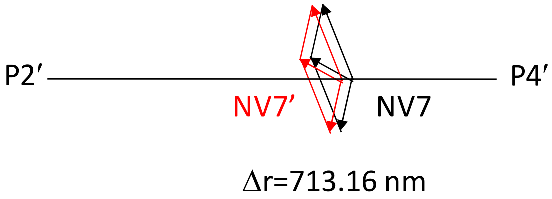

Figure 27. Another NV center position can be calculated while keeping the orientation fixed. The calculated distance between two NVs is 713.16 nm.

3.6 Conclusion

The distance measurement is one of the fundamental topics in the physical and life sciences. In order to achieve the spatial resolution of the NV color centers in the solid-state crystal, the 2D EPRI approach is taken for the first time using the pulsed ESR experiment to measure the Rabi frequency. Using one wire pair, the NV center seems to be a single but the second wire pair discovers the phantom impurity with the resolution of 713.16 nm.

From this experiment it is verified that the steep AC magnetic field gradient achieved between two diagonal wires can be used to measure the distance between closely located double NVs. The microfabrication technology is one of the essential methods for this experiment as it is the enabling technique to make a metal structure directly on the bulk diamond surface. However, the imperfection in the micronscale pattern can cause the mismatch between the calculation and the measurement.

Another challenge is the reliability of modeling on the magnetic field at the position of the central area. The quadratic dependence of the magnetic field along the distance between two points makes the field simplification approach reasonable. But the precise quantitative comparison between the calculation and the field measurement is anticipated to reduce the imperfection in the field orientation and intensity, and subsequently in the Rabi frequency.

CHAPTER IV

DIPOLAR LINEWIDTH NARROWING ON THE NITROGEN VACANCY IN DIAMOND USING THE ROTATING FIELD

4.1 Introduction

The magnetometer is an essential instrument measuring the magnetic field and has many applications in industry and in scientific research. The superconducting quantum interference device (SQUID)-based magnetometer provides extremely high sensitivity but has a cryogenic barrier which means that the SQUID needs cooling.[80] The atomic vapor magnetometer based on spin-exchange relaxation free (SERF) can provide the higher sensitivity[81]. Recent experiment demonstrated the atomic magnetometer of which sensitivity decreased to sub-fT $Hz^{-1/2}$ but the cell needed to be heated to 180°C[82]. Thanks to the advance in the nitrogen vacancy (NV) color center in diamond, the NV-based magnetometer produces the sensitivity surpassing that of SQUID[22] and has less limitation in the size and spin linewidth caused by the wall collision at room temperature compared to the atomic vapor magnetometer.

Due to the recent developments in diamond synthesis, the high purity of diamond can be achieved using the homoepitaxial diamond growth based on the chemical vapor deposition (CVD) method[83]. In the high purity diamond, the electron spin dynamics of a nitrogen vacancy (NV) is in the presence of strong influence of ^{13}C (1.1% abundance) and the spin coherence time and the electron spin linewidth $\Delta\nu$ are dependent on the nuclear spin of ^{13}C[64,84]. On the other hand, a few diamonds synthesized by the high-temperature/high-pressure (HPHT) method are characterized by the high concentration of the nitrogen atom. The electron spin of the NV center is dominated by the electron spins of the substitutional ^{14}N.

For the purpose of the magnetic sensor, the HPHT diamond can be used since it has a high concentration of the substitutional nitrogen (N_s) and the conversion technique from N_s to the NV is investigated[85]. But the sensitivity of the magnetometer is dependent on the spin linewidth which is mainly governed by the dipole-dipole coupling between the electron spin of the NV center and the ^{14}N electron spin. In order to suppress the linewidth broadening caused by this impurity, the rotating field such as magic angle spinning can be used[86,87]. In this paper, the rotating field is applied to considerably suppress the linewidth broadening and enhance the resolution of the ESR spectroscopy on the NV center.

4.2 Theoretical Background

Spin Hamiltonian for Two Unpaired Electrons

The NV center is composed of a substitutional nitrogen and an adjacent vacancy. The substitutional nitrogen is an electron donor and the NV center is negatively charged with the electron spin state S=1. Once the NV center is optically excited, the fluorescence emission is detected due to the $^3E \rightarrow {}^3A$ transition with a 637 nm zero-phonon line. The triplet ground state (^{3}A) is split into $m_s = \pm 1$ and $m_s = 0$ sublevels separated by the 2.87 GHz microwave transition [Figure 28(a)][31,88].

The spin Hamiltonian describing the behavior of the NV center is

$$H = g\beta_e \mathbf{B}^T \cdot \mathbf{S} + \mathbf{S}^T \cdot \mathbf{D} \cdot \mathbf{S} \tag{18}$$

where g is the electron g-factor, β_e is the Bohr magnetron, D is the zero-field tensor, and S is the electron spin. If the Hamiltonian is written in the basis set of $|+1\rangle$, $|0\rangle$ and $|-1\rangle$ of the electron spin S and the magnetic field B is taken along the quantization axis ($B \parallel z$), the energies can be expressed by $-\frac{2}{3}D$ and $\frac{1}{3}D \pm g\beta_e B_z$ with the external magnetic field, B_z, and $D = 2.87$ GHz due to C_{3v} symmetry ($E = 0$) [Figure 28(b)].

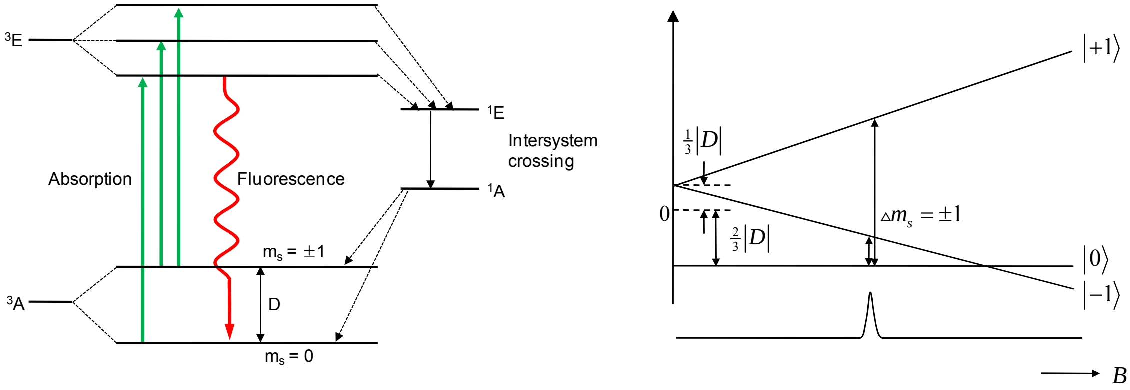

(a) (b)

Figure 28. (a) The energy level diagram of the NV center is depicted. (b) If the magnetic field is applied along the quantization axis, the degenerate $m_S=\pm 1$ state is split and the three energy states are obtained. Using the optically detected magnetic resonance (ODMR) spectroscopy, the $\Delta m_S=\pm 1$ transitions are observed.

Unpaired Electron Coupling with ^{14}N Electron

For the HPHT diamond with a high ^{14}N concentration, the dipole-dipole coupling between the electron spin of the NV center and the ^{14}N electron spin is taken into account, the total Hamiltonian becomes

$$H = g\beta_e \mathbf{B}^T \cdot \mathbf{S} + \mathbf{S}^T \cdot \mathbf{D} \cdot \mathbf{S} + H_{dd} \tag{19}$$

If the electron magnetic dipoles behave classically and the external static magnetic field **B** (||**z**) is applied to align them, the energy of dipole-dipole interaction between them is given by the expression below[48,89,90,91,92]:

$$U = -\mu_e^T \cdot B_N(\mathbf{r}, \mu_N) \tag{20}$$

where μ_e and μ_N are the electron dipole moments of the NV center and ^{14}N and θ is the angle between **B** and the line joining the two dipoles separated by the distance r. In this classical system which is shown in Figure 29 the local field, B_N, at the NV center arising from the ^{14}N electron spin depends on the angle θ and distance r is given by

$$B_N(\mathbf{r}, \mu_N) = -\frac{\mu_0}{4\pi}\frac{1}{r^3}\left[\mu_N - \frac{3}{r^2}(\mu_N^T \cdot \mathbf{r})\mathbf{r}\right] \tag{21}$$

Thus, the energy becomes

$$U = \frac{\mu_0}{4\pi}\frac{1}{r^3}\left[\mu_e^T \cdot \mu_N - \frac{3}{r^2}(\mu_e^T \cdot \mathbf{r})(\mu_N^T \cdot \mathbf{r})\right] \tag{22}$$

The dipolar Hamiltonian for the broadening is expressed in the similar way to the dipole-dipole coupling between an electron spin and a nuclear spin by

$$H_{dd} = \frac{\mu_0}{4\pi}\frac{g\beta_e g_n \beta_n}{r^3}\left[\mathbf{S}_e^{\mathbf{T}} \cdot \mathbf{S}_N - \frac{3}{r^2}(\mathbf{S}_e^{\mathbf{T}} \cdot \mathbf{r})(\mathbf{S}_N^{\mathbf{T}} \cdot \mathbf{r})\right] \tag{23}$$

Using the θ and ϕ in the polar coordinate,

$$\begin{aligned} H_{dd} &= \omega[\mathbf{S}_e^{\mathbf{T}} \cdot \mathbf{S}_N - 3[S_{ez}\cos\theta + \sin\theta(S_{ex}\cos\phi + S_{ey}\sin\phi)]\times \\ &\qquad\qquad [S_{Nz}\cos\theta + \sin\theta(S_{Nx}\cos\phi + S_{Ny}\sin\phi)]] \\ &= \omega[\mathbf{S}_e^{\mathbf{T}} \cdot \mathbf{S}_N - 3[S_{ez}\cos\theta + \tfrac{1}{2}\sin\theta(S_e^+ e^{-i\phi} + S_e^- e^{i\phi})]\times \\ &\qquad\qquad [S_{Nz}\cos\theta + \tfrac{1}{2}\sin\theta(S_N^+ e^{-i\phi} + S_N^- e^{i\phi})]] \\ &= \omega(A + B + C + D + E + F) \end{aligned} \tag{24}$$

where the dipolar alphabets are

$$\begin{aligned}
A &= S_{ez}S_{Nz}(1-3\cos^2\theta)\\
B &= -\tfrac{1}{4}(S_e^+S_N^- + S_e^-S_N^+)(1-3\cos^2\theta)\\
C &= -\tfrac{3}{2}(S_e^+S_{Nz} + S_{ez}S_N^+)\cos\theta\sin\theta e^{-i\phi}\\
D &= -\tfrac{3}{2}(S_e^-S_{Nz} + S_{ez}S_N^-)\cos\theta\sin\theta e^{i\phi}\\
E &= -\tfrac{3}{4}S_e^+S_N^+\sin^2\theta e^{-2i\phi}\\
F &= -\tfrac{3}{4}S_e^-S_N^-\sin^2\theta e^{2i\phi}
\end{aligned} \tag{25}$$

and the dipolar frequency ω is

$$\omega = \frac{\mu_0}{4\pi}\frac{gg_n\beta_e^2}{r^3} \tag{26}$$

For the NV and nitrogen system, the dipolar Hamiltonian is simplified to the secular term A given by

$$H_{dd} = \frac{\mu_0}{4\pi}\frac{gg_n\beta_e^2}{r^3}S_{ez}S_{Nz}(1-3\cos^2\theta) \tag{27}$$

Magic Angle Spinning

The dipole-dipole coupling shows the dependency on the orientation of the spin-to-spin vector $\mathbf{r}$ with respect to the external magnetic field $\mathbf{B}$. The reorientation of the vector $\mathbf{r}$ has been performed by rotating the sample itself in many experiments[93]. If the angle θ is manipulated to be the magic angle, $\theta = 54.7^\circ$, the dependency turns out to be averaged out over the time duration for the experiment.

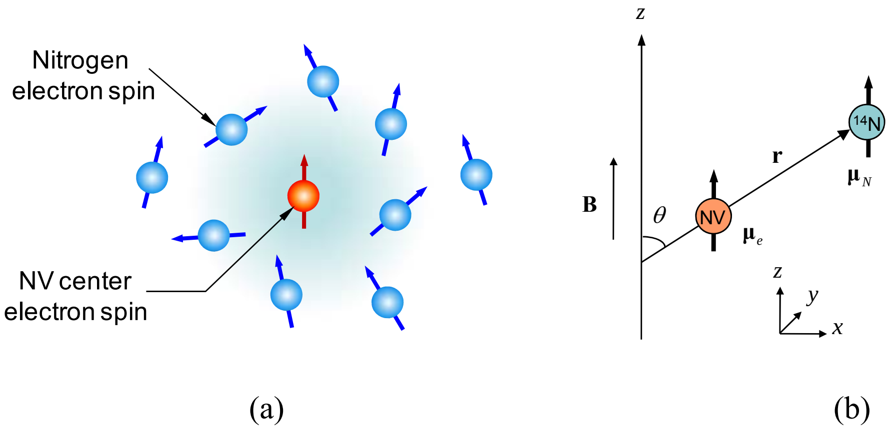

(a) (b)

Figure 29. (a) The electron spin of the NV center and the N electron spin configuration are illustrated. (b) They are placed in the external magnetic field B and the angle between B and the line connecting the electron and nuclear spins is θ. There exists the dipole-dipole coupling between the NV center and the intrinsic ^{14}N electron spins.

4.3 Materials and the Method

The sample used for this experiment was a (111) cut HPHT diamond with 40 ppm of nitrogen concentration and 10 ppm of NV^- concentration. The micronscale gold wire was fabricated for microwave signal transmission to manipulate the spin states of the NV center. Figure 30(a) shows the gold wires to apply the microwave and RF signals. The metal structure was made on the surface of a sapphire coverslip. The sample substrate was coated with Ti and Au in order. On top of metal surface, the thick photoresist pattern was created using the photolithography technique and development and the electroplating was followed in turn. After stripping the remaining photoresist, the underlying thin Ti and Au layers were etched and the thick gold pattern remained. For the ESR spectroscopy, the microwave and RF signals are transmitted through the wires which were bonded on the diamond surface.

The diamond sample rotation is technically limited since the microwave and RF signal needs to be applied at the same time. As an alternative, the four micron-size wires surrounding the central area are suggested [Figure 30(b)]. If the two phase-matched $\sin \omega t$ and $\cos \omega t$ signals are applied to the two diagonal wire pairs, the rotating RF signal is generated at the center and is proposed to reorient the spin-to-spin vector.

For the simulation of the magnetic field built on the x-y plane below the diamond surface, the 3D finite element method (FEM) simulator (HFSS, Ansoft) was used. From the simulation results in Figure 31, it should be noted that the generated field is elliptical rather than circular in the magnitude due to the asymmetry of the structure. Since the external field rotates in a slightly different shape at each depth underneath the surface, this may cause the axially asymmetric rotating field.

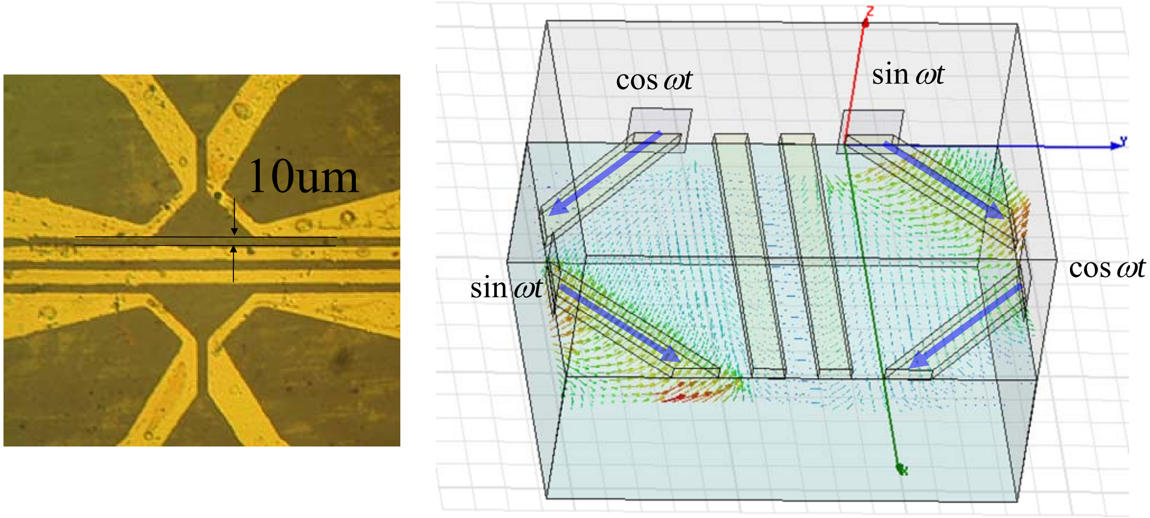

(a) (b)

Figure 30. (a) The gold wires are fabricated on the sapphire substrate and are bonded on the (111) cut HPHT diamond surface. The wires are connected to the external circuit board to apply the microwave and RF signals. (b) In order to produce the rotating field, the four wires structure is suggested with extra wires for the microwave signal.

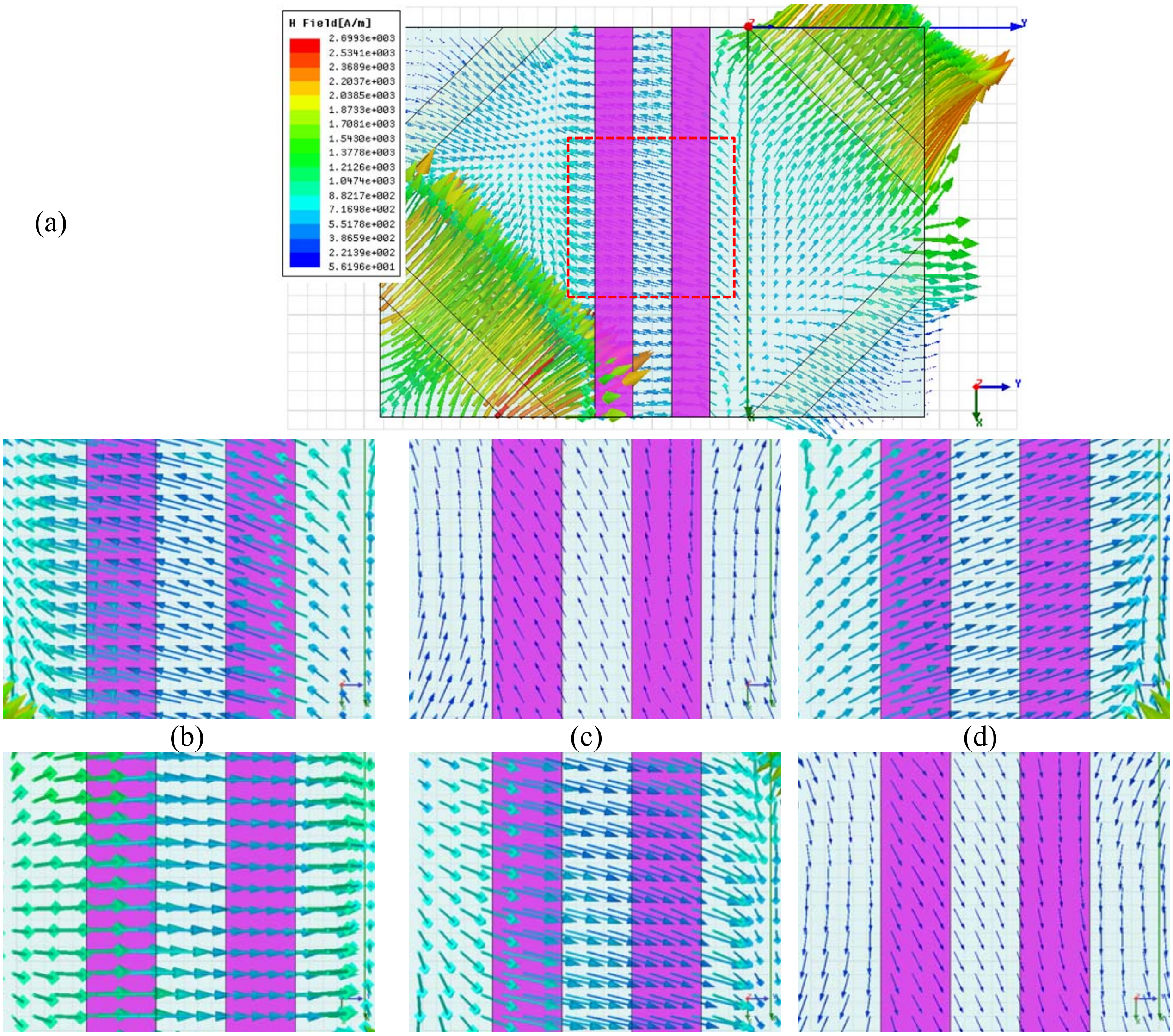

(a)

(b) (c) (d)

(e) (f) (g)

Figure 31. (a) The phase-matched sinωt and cosωt signals are excited to the two diagonal wire pairs with 1 Watt of the power. The generated field within the red dotted rectangle with the depth set to 10 μm underneath the surface are displayed at different phases of the input signals such as (b) 0º, (c) 45º, (d) 90º, (e) 135º, (f) 180º and (g) 225º, respectively.

The diamond sample was excited using the 532 nm Ar ion laser. A 0.8 numerical aperture objective of 100x was used to focus the green light and collect the fluorescence. Once the fluorescence emission passes through the dichroic mirror to separate the optical pumping light, it is detected using the color filtered (647–800 nm bandpass) Si photodiode.

There exist four different orientations of the NV center in the diamond as shown in Figure 32(a), (b), (c), and (d). In order to separate orientations, three-dimensional electromagnetic coils were built to control the magnetic field along each axis independently. If the microwave signal is applied to the wire, the electron spin of the NV center is manipulated between $\left| m_S = +1 \right\rangle$ and $\left| m_S = 0 \right\rangle$ in the ground state. The optically detected magnetic resonance (ODMR) signals are detected using the microwave signal frequency sweeping [Figure 32(e)]. The [111] oriented ensemble NVs are selectively chosen using the electromagnet for this experiment.

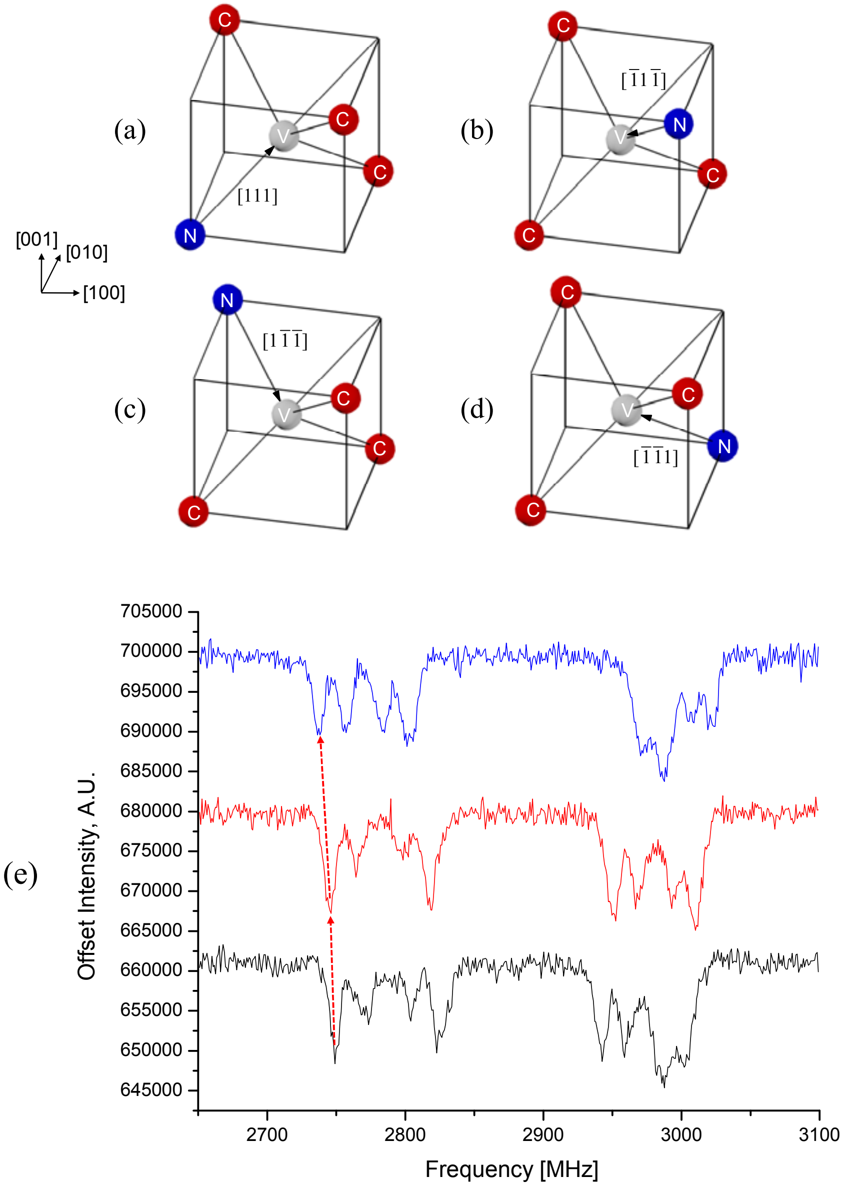

Figure 32. (a), (b), (c), and (d) There exist four different orientations of NV center with respect to the crystal axes. (e) The ODMR signals were measured using the microwave frequency sweeping. If the current flow to one electromagnet coil is controlled to vary the magnetic field, the ODMR signal shows the different frequency variation to each orientation. Using this manipulation, the orientation of the ensemble NVs can be selectively chosen.

4.4 Results

Lindwidth Narrowing

When the microwave signal is applied, the electron spin linewidth $\Delta\nu$ shows the dependence on the microwave signal and laser powers[94]. The full-width half-maximum (FWHM) of the linewidth increases as the microwave power goes up while it decreases as the optical power goes down. For the given microwave and optical powers, the RF signals are applied to four wires and the external field is rotating on the x-y plane [Figure 33].

Figure 34(a) shows the main dip while the rotating field causes the sidebands located at the multiples of the rotation frequency ν_{RF}. After analyzing the data, the characterized FWHM of the electron spin decreases from 3.4 MHz to 2.5 MHz as the RF power goes up to 40 dBm. For a few different RF frequencies in Figure 34(b), the measurements show that the FWHM decreases, especially from 2.8 MHz to 1.4 MHz for ω_{RF} = 2.5 MHz.

The observed linewidth was suppressed up to 50% using the rotating field. The linewidth did not reach the ^{13}C limit at which the broadening is ~200kHz, thus, the rotating field seems to not be large enough to average out the dipole-dipole coupling in the time-domain of the experiment. The distance between one wire and the center is about 55 μm and needs to be reduced by removing the central two wires. On the other hand, in Figure 34(a) the center frequency shift is observed up to 8 MHz for ω_{RF} = 2.5 MHz as the RF power increase. The shift may be caused partially by the g-factor inhomogeneity, elliptical field distribution, and weak vibration due to the high RF power.

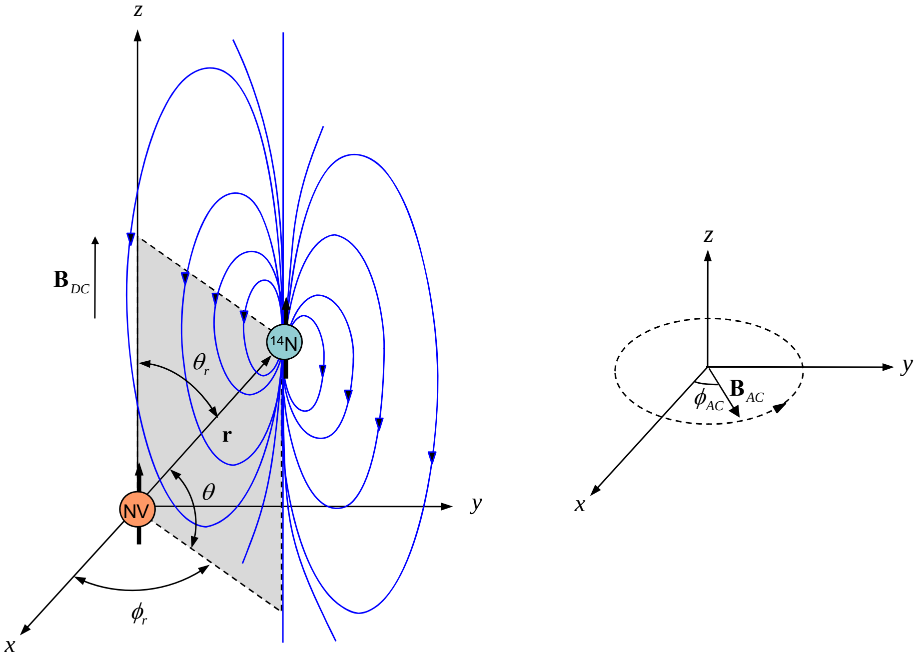

Figure 33. A simple system for the rotating field to suppress the dipole-dipole coupling between the NV center and the ^{14}N electron spin is illustrated. The static magnetic field B_{DC} was applied to isolate four orientations and choose the [100] orientation selectively. The rotating field B_{AC} was applied on the x-y plane and the angle between spin-to-spin vector r and the external rotating field was given as θ.

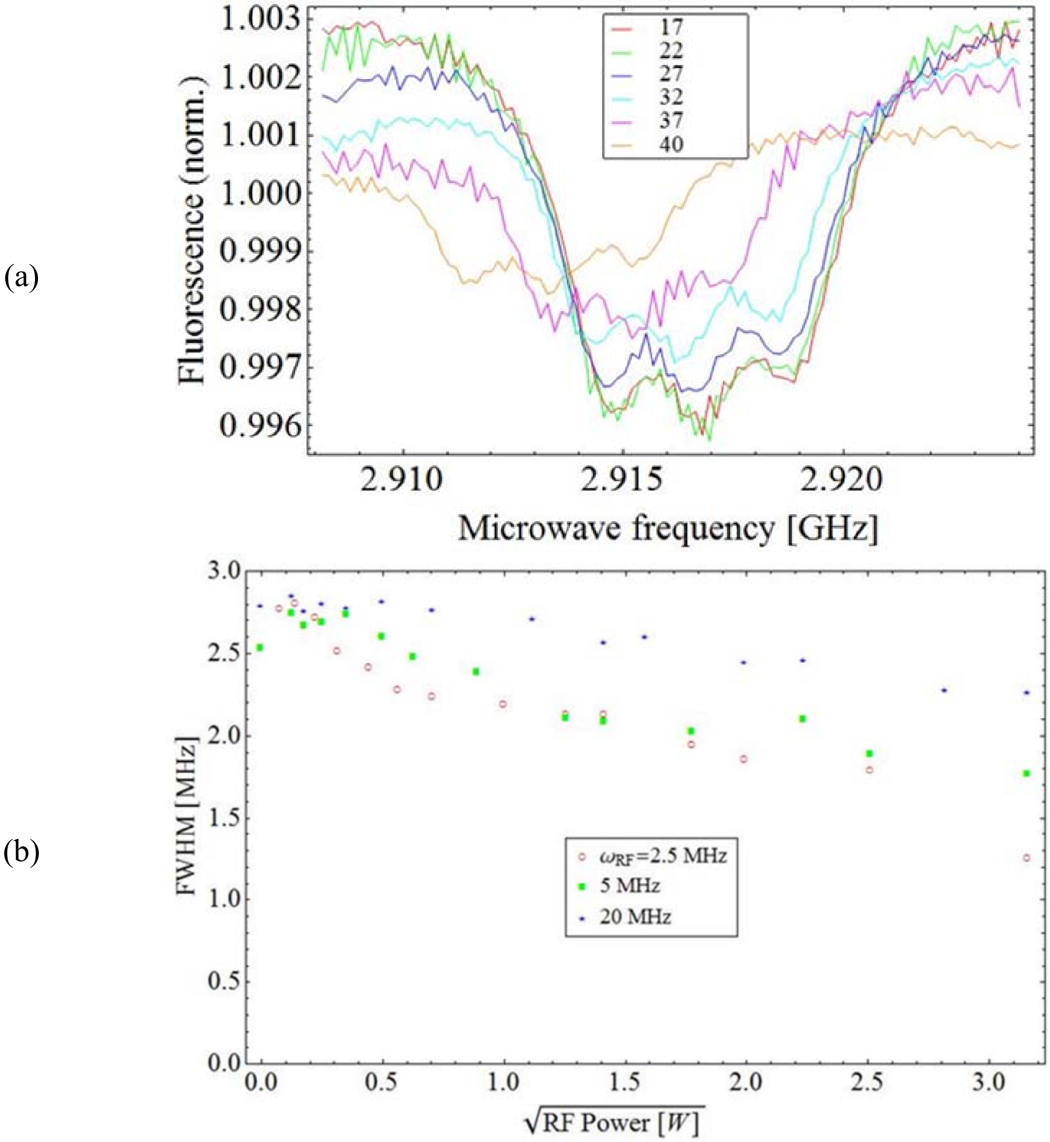

Figure 34. (a) The CW ESR data are depicted for different RF powers using ω_{RF} = 12 MHz, P_{mw}= -20 dBm and P_{opt}= 8 mW. (b) The CW ESR data are characterized for different RF powers and frequencies using P_{mw}= -25 dBm and P_{opt}= 10 mW.

Optical Magnetometry and the Effective Time Constant T_2^*

In the optical magnetometry, the sensitivity of the magnetometer is given by[22,95]

$$\delta B \simeq \frac{\hbar}{g\beta_e\sqrt{NtT_2^*}} \tag{28}$$

where $\hbar$ is Planck's constant, N is the number of the NV centers, t is the total averaging time, and T_2^* is the effective relaxation time. Practically the inhomogeneously broadened linewidth which is the full-width half-maximum of the spectral peak is given by $\Delta\nu = 1/(\pi \cdot T_2^*)$ [96]. Using the rotating field, T_2^* was improved from 114 ns to 227 ns. This corresponds to ~30% improvement in the detectable sensitivity.

4.5 Conclusion

In this experiment, the rotating field suppression was observed in the spin linewidth broadening of the NV center caused by the substitutional ^{14}N in a HPHT diamond. The ESR spectroscopy measurements show that the ~50% improvement was obtained in $\Delta\nu$. Subsequently, the sensitivity of the magnetometer using the diamond increases by ~30%.

In order to achieve the higher suppression of the broadening, the rotating field intensity needs to be increased. Using the microfabrication technology for the upgraded metal structure with the central wires removed, the distance between the center and wires can be reduced to $10\,\mu m$ which results in the 5.5 times larger field. It is expected that the linewidth dominated by the ^{13}C (1% abundance) can be obtained using the higher field intensity.

The other technique to investigate the linewidth narrowing is the free induction decay (FID). The linewidth measurements for the rotating samples were reported using the FID[97]. The rotating field experiment along with the FID is anticipated using the numerical analysis based on the time-dependent Hamiltonian such as Floquet Hamiltonian[98] for a better understanding of the sidebands and linewidth narrowing.

CHAPTER V

NV DIAMOND ESR AND IONIZATION FRACTION VS ELECTRON IRRADIATION DOSE

5.1 Introduction

The nitrogen-vacancy (NV) center in diamond has been explored recently for many applications including quantum information, magnetic sensors and subwavelength imaging. Much of the NV utility is due to its optically detectable ground-state electron spin resonance. To achieve the best performance, a high concentration of NV centers is desired[22]. This is done by either implanting nitrogen into pure diamond or by creating vacancies in nitrogen-rich diamond, followed by annealing to produce the NVs. Substitutional nitrogen atoms (N) that do not form NVs are a source of spin dephasing, and so it is important to maximize the conversion of N to NV. One way to achieve this is with high-dose electron irradiation. To first order, the fraction of N converted to NV is linear in irradiation dose. However at very high doses, so much damage can accumulate that the diamond is converted to graphite. In this paper we show that even well below the graphitization threshold, the irradiation damage can have a pronounced effect on the properties of the NV.

Diamond can be damaged using a number of irradiating species including electron, neutron, proton and ion beams. Koike *et al* reported on the displacement threshold energy, T_d, of type IIa natural diamond using TEM for three principal crystallographic directions, [100], [110], and [111]. It was found that T_d was 37-48eV and the minimum electron incident energy needs to be 180-220 keV in order to form displacement-related defect clusters[99]. Steeds and his co-workers demonstrated the creation of self-interstitials, a carbon-carbon pair along [100], using a 300 keV TEM[100,101]. Campbell and Mainwood predicted the radiation damage of diamond caused by both electron and Gamma irradiation. According to their calculations, for 250 keV electrons the maximum penetration depth is ~375 μm and the number of vacancies per micrometer depth is 0.74 (vacancies/electrons/cm)[102]. Recently, Acosta *et al* reported proton and electron irradiation on diamond, comparing the converted NV^- and NV^0 concentrations for optical magnetometer applications[85].

5.2 Materials and the Method: TEM Irradiation

We use TEM irradiation of the [100] orientation of nitrogen-rich type Ib bulk diamond. After irradiation the vacancies are made mobile by annealing at approximately 700 C. These vacancies are attracted to a substitutional nitrogen center, N_S^0, to form a NV as follows[39,103]:

$$\begin{gathered} N_S^0 + V^0 \rightarrow NV^0 \quad \text{and} \\ NV^0 + N_S^0 \rightarrow NV^- + N_S^+ \end{gathered} \tag{29}$$

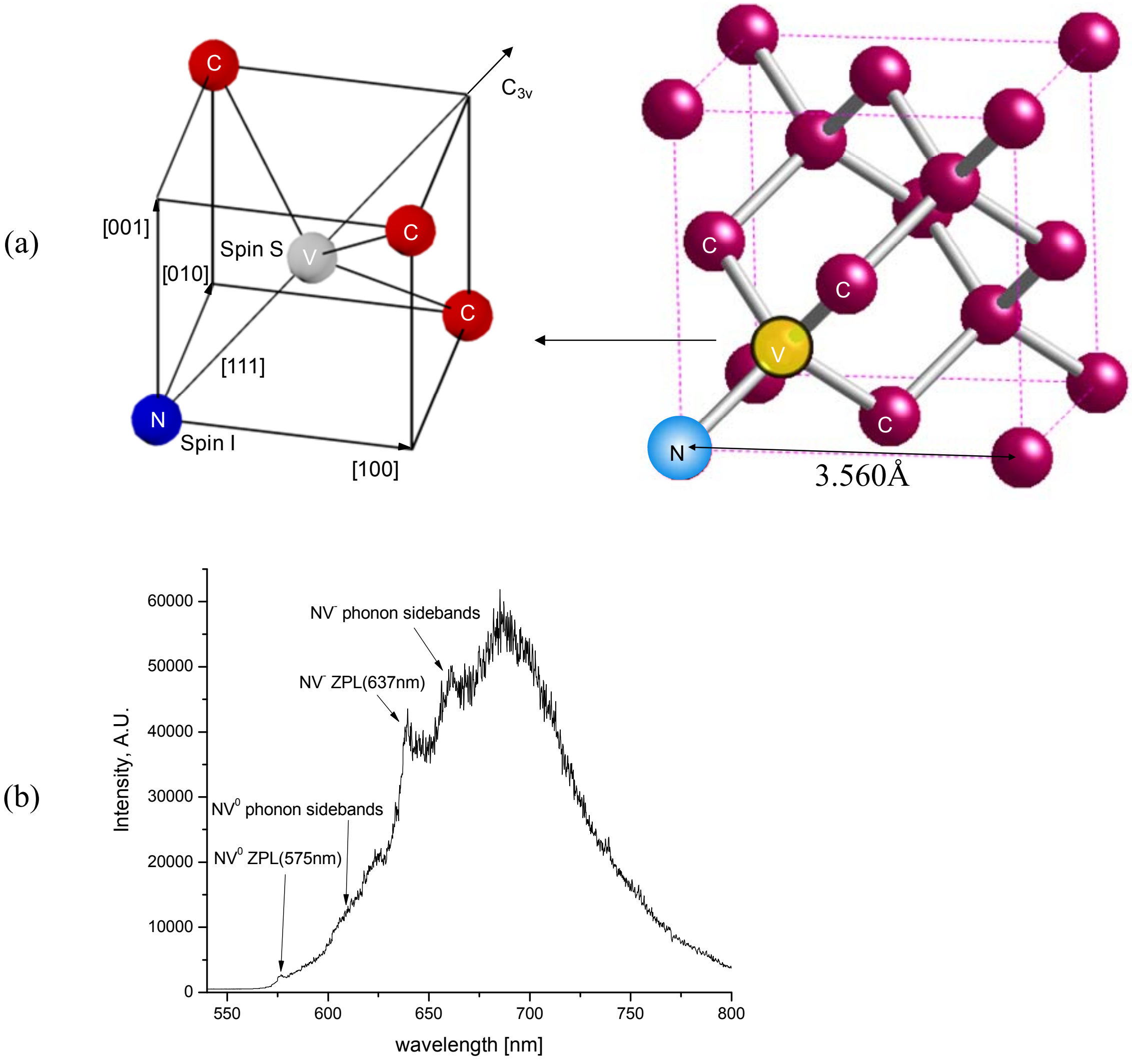

Figure 35. (a) The NV defect center is oriented to the [111] direction in the schematic diagram of the diamond lattice. (b) Typical spectrum for the NV center. The spectrum was taken for the (100) type-Ib diamond with the optical power of P_{op}=1.98 mW.

The second reaction assumes that a second nitrogen center serves as an electron donor to enhance the fraction of negatively charged NV centers. Here the [100] orientation is chosen because it has a lower electron-energy threshold for displacement of the carbon atoms compared to the other orientations at room temperature, and this allows us to use our 200 keV TEM.

It is now widely accepted that there are six electrons associated with the NV^- center[40], three from the dangling carbon bonds, two from the nitrogen, and one from the donor. Unlike most color centers, the ground state is an electron spin triplet, S = 1, and thus the NV^- center is a paramagnetic impurity. Figure 35 shows a physical view of the NV defect center in diamond and the typical fluorescence emission spectrum. In type-Ib diamond, most of the nitrogen exists in the form of a single substitutional nitrogen which serves as an electron donor[104,105]. For this reason, electron irradiation experiments on a type Ib diamond normally produce the negatively charged NV^-.[106]

The diamond used in this experiment was a type-Ib HPHT single-crystal plate grown at Element Six with an initial nitrogen concentration of 40-70ppm. The irradiation was done using a 200kV TEM (JEOL JEM-2010) which is over the minimum incident electron energy to form the defect clusters reported by Koike *et al*. A wide range of irradiation doses were studied ranging from 1.28×10^{18} to $6.39\times10^{21}e^-/cm^2$. Each irradiated spot is produced by focusing the electron beam to a diameter of a few microns and exposing it for different time durations to vary the electron dose. After the irradiation, annealing at 700°C is done both to create NVs and to heal the irradiation damage of the diamond.

The optical test setup is based on scanning confocal microscopy. A 532 nm Nd:YAG laser illuminates the diamond sample through a long working distance objective with numerical aperture of 0.8 and magnification of 60x. The scanned images before and after the annealing process are shown in Figure 36 where the absolute count rate is reproducible within factor of 2 between runs. Prior to the annealing, the high dose spots give visible fluorescence but the low dose spots are not detected [Figure 36(a)]. After the annealing a large increase in the APD count rate is seen shown in Figure 36(b) to (e) and Figure 37.

5.3 Results

Spectrum

The emission spectrum from each of the irradiated spots was measured before and after annealing, and at different depths. For reference, the spectrum of the unirradiated diamond surface is shown in Figure 37(a). Before the annealing, the emission spectrum from the highest dose region gives a broad featureless spectrum in this spectral region, as seen in Figure 37(b), but after annealing the fluorescence intensity shows a drastic increase as seen in Figure 37(c) and Figure 38, for multiple irradiation doses. At low doses, the spectra show that NV^- is the dominant defect even at this low electron voltage as reported by Uedono *et al* for type-Ib diamond. As the dosage increases, the NV^0 fraction rises and a new peak at 639 nm appears, which obscures the zero phonon line of NV^- at 638 nm.

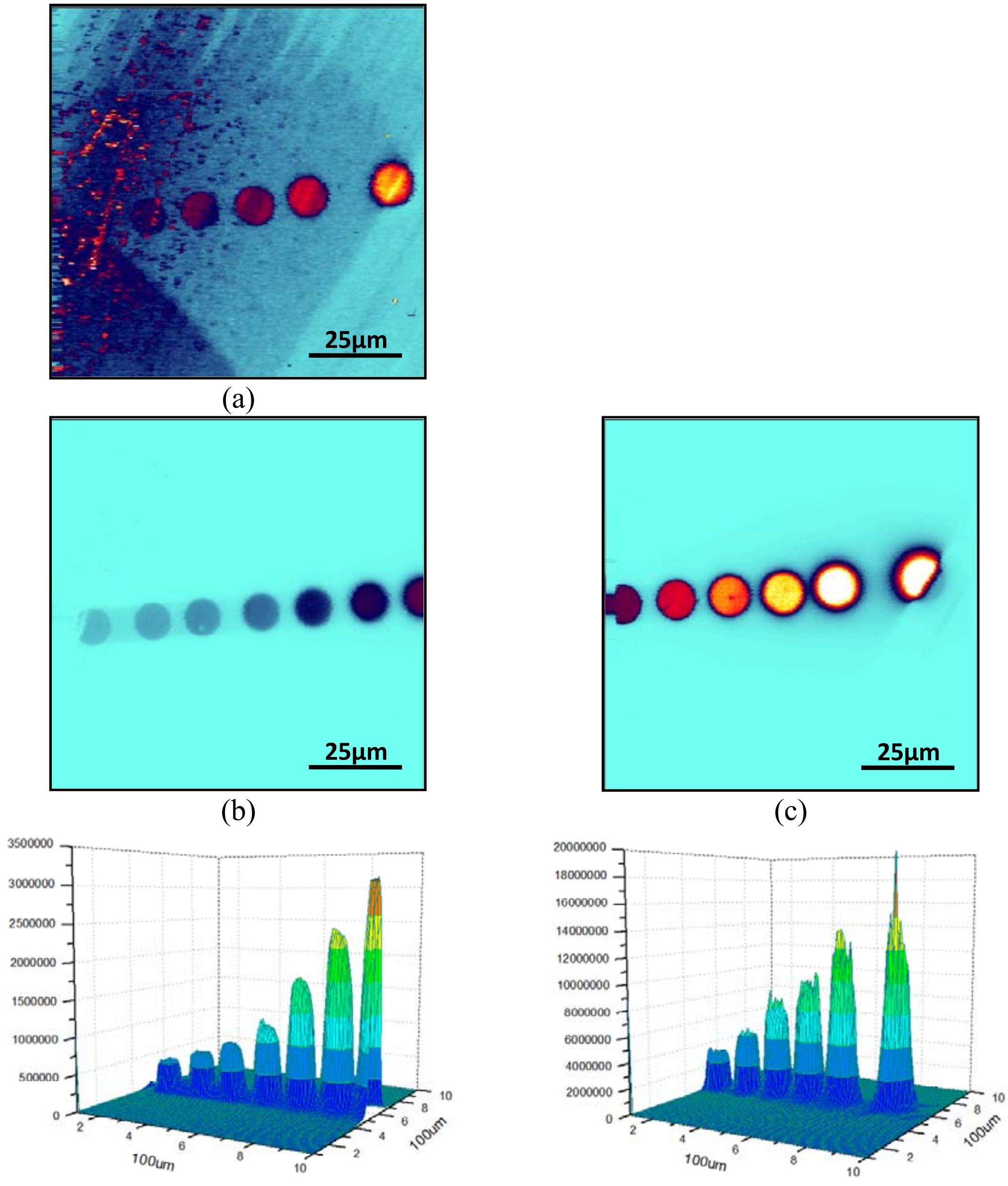

(a)

(b) (c)

(d) (e)

Figure 36. (a) The TEM irradiated spots appear before the anneal. The highest dose is located on the rightmost hand side and the dose goes down to the left side. The fluorescence image is measured with no optical attenuator and the low dose spots are not detected since their fluorescence is not high enough compared to the background. The process of annealing removes the irradiation damage to the lattice structure and results in a huge difference in the fluorescence of the NVs. (b), (c), (d) and (e) are the scanned fluorescence images using the APD for twelve different doses, where (b) and (d) are lower six doses and (c) and (e) are higher ones.

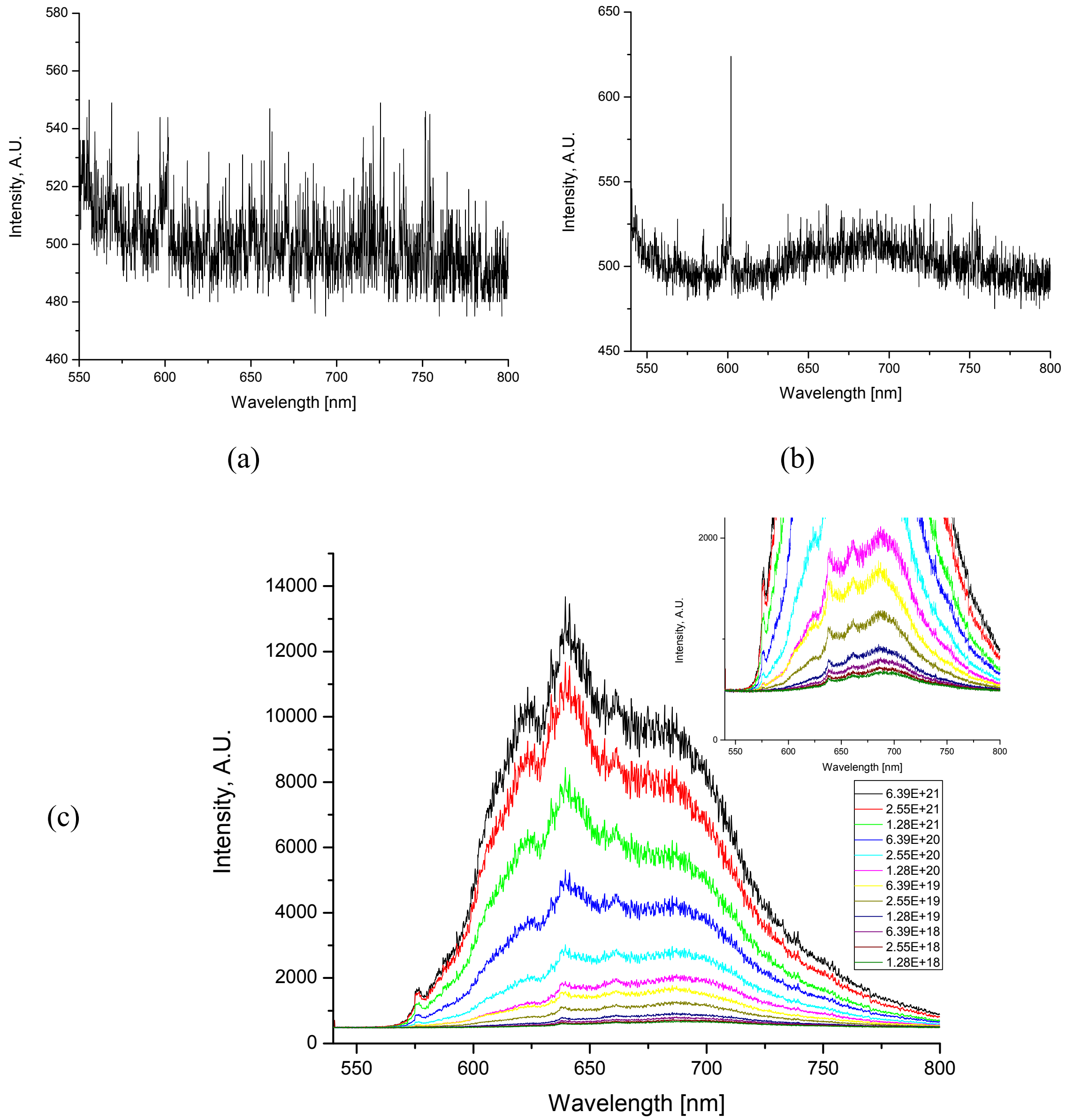

(a)

(b)

(c)

Figure 37. The spectra are measured (a) on the unirradiated area and (b) on the irradiated spot for the highest dose before the annealing and show a very weak intensity in the spectral range for the fluorescence. (c) The spectrum for each dose is obtained at the same optical power and integration time. As the dosage increases, it is observed that the NV^0 and NV^- peaks also rise. (d) For the high dose, the spectra measured at different focal point below the diamond surface displays the TEM irradiation depth profile. The maximum intensity for the third highest dose is ~2 μm below the surface and the irradiation extends penetration down below 18 μm.

(d)

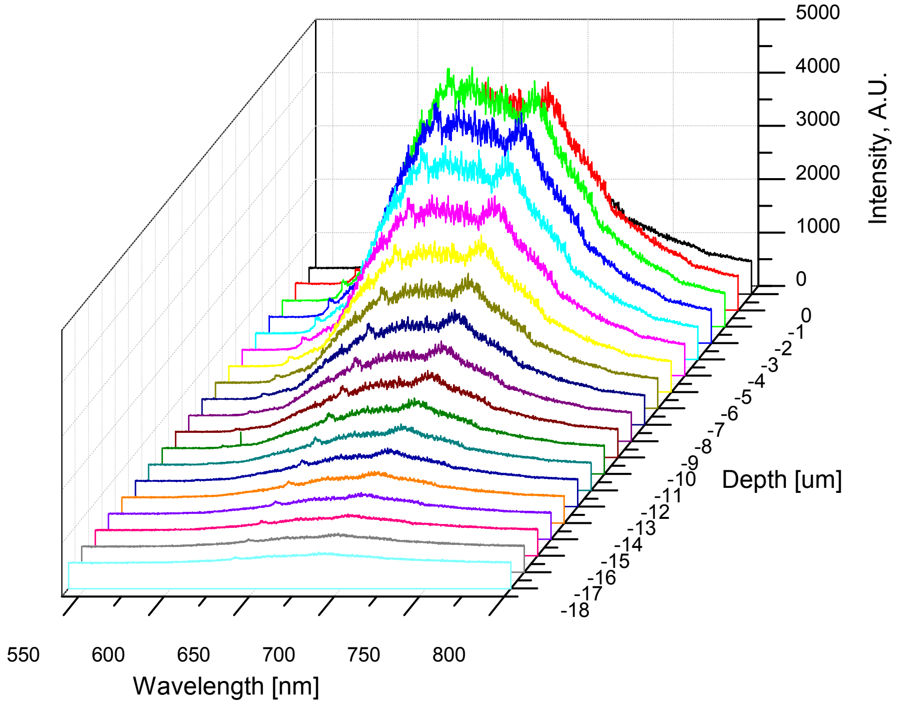

Figure 37 Continued

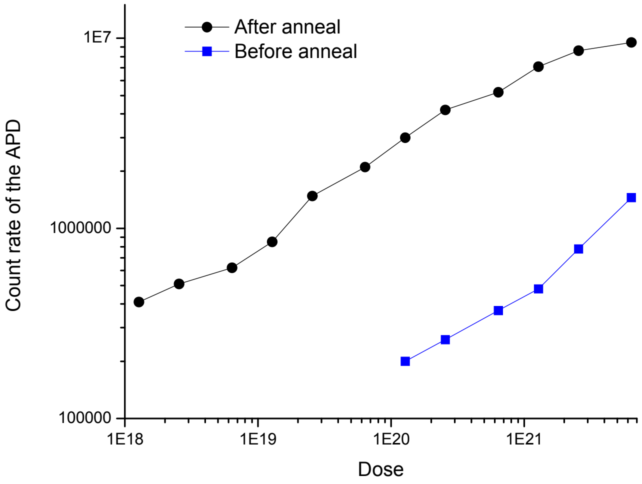

Figure 38. The fluorescence count rate of the APD before and after anneal is shown on the log scale, where an optical attenuator (0.5% transmission) is used to protect the APD for the count rate after anneal. The count rate after anneal shows a saturation as the dosage goes up.

Spectra recorded at various depths below the surface [Figure 37(d) and 39(b)][107] show NV^0 and NV^- features down to 2–4 μm below the surface, where the resolution in this direction is estimated at 1 μm.

To estimate NV concentration, the zero phonon peaks at ~575 nm and at ~638 nm are fit to a Gaussian function. The result is shown in Figure 39. Here, the NV^0 and NV^- concentrations saturate at around 1×10^{21} $-1\times10^{22}e^-/cm^2\cdot s$, where NV^- saturates earlier. The NV^- concentration still appears to rise at the highest dose but this is actually due to the unidentified peak at 639 nm [see Table 2 and $\Delta\lambda_c$ in Figure 39(a)]. The apparent ratio of NV^0 to NV^- is found to be maximized at $2.55\times10^{21}e^-/cm^2\cdot s$.

At high enough dose, ion irradiation can transform the diamond structure to graphite,[108] as evidenced by the broadband fluorescence which appears before annealing at the highest doses. The transformation proceeds in proportion to the dose and eventually the characteristics of diamond are lost. The saturation of the NV conversion happens as the graphitization threshold is approached.

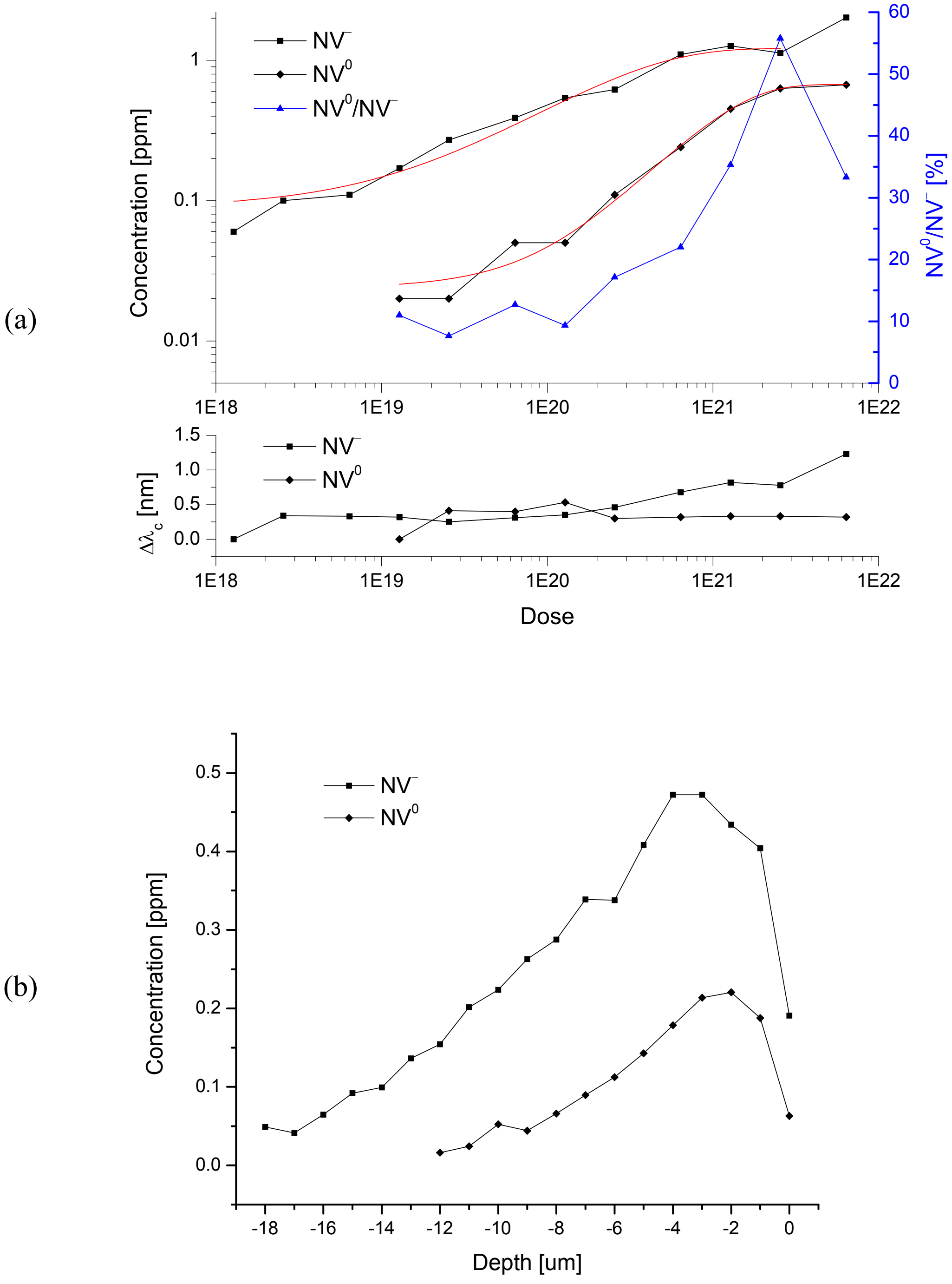

Figure 39. (a) The NV⁻ and NV^0 concentrations over 632–643 nm and 572–530 nm ranges respectively can be calculated using the spectrum from the NV⁻ concentration already known. The concentration curves will be the same as ones for A×B in Table 2 except the constant conversion factor is applied. (b) The NV⁻ and NV^0 concentrations are depicted as the depth varies.

Table 2. The NV$^-$ and NV^0 peaks are characterized to obtain the center wavelength, FWHM and height.

	NV$^-$					NV0				
Dose [e-/cm^2]	λ_c [nm]	FWHM (A) [nm]	Height (B) A.U.	AxB	Concen. [ppm]	λ_c [nm]	FWHM (A) [nm]	Height (B) A.U.	AxB	Concen. [ppm]
1.28E+18	638.17	3.66	35.09	128.45	0.06	–	–	–	–	–
2.55E+18	638.51	4.03	47.27	190.41	0.10	–	–	–	–	–
6.39E+18	638.50	4.01	56.20	225.20	0.11	–	–	–	–	–
1.28E+19	638.49	4.16	82.19	342.31	0.17	575.84	4.23	8.94	37.79	0.02
2.55E+19	638.42	3.85	140.26	539.92	0.27	576.25	2.38	17.34	41.23	0.02
6.39E+19	638.48	3.92	200.27	784.07	0.39	576.24	2.70	36.90	99.50	0.05
1.28E+20	638.52	4.13	259.44	1071.12	0.54	576.37	2.90	34.24	99.24	0.05
2.55E+20	638.63	3.77	326.21	1228.32	0.62	576.14	2.72	76.99	209.58	0.11
6.39E+20	638.85	4.52	483.23	2183.36	1.10	576.16	2.65	181.37	480.19	0.24
1.28E+21	638.99	4.16	609.59	2534.38	1.27	576.17	2.66	335.97	894.00	0.45
2.55E+21	638.95	3.93	571.26	2242.67	1.13	576.17	2.66	470.40	1250.99	0.63
6.39E+21	639.40	3.98	1009.99	4021.66	2.02	576.16	2.63	508.49	1338.63	0.67

Electron Paramagnetic Resonance Shift

The electron spin transition frequency of the NV⁻ center is given by a Hamiltonian typical for a system with two unpaired electrons in C_{3v} symmetry:

$$H = g\beta_e \mathbf{B}^T \cdot \mathbf{S} + \mathbf{S}^T \cdot \mathbf{D} \cdot \mathbf{S} \tag{30}$$

When the magnetic field (B_z) is applied along the quantization axis of the electron spin, S_z, this Hamiltonian has eigenfunctions: $|+1\rangle$, $|0\rangle$ and $|-1\rangle$ of S_z. If $B_z = 0$, there are three states, one of energy $E_0 = -\frac{2}{3}D$ and the other two of energy $E_{\pm 1} = \frac{1}{3}D$ where the zero-field splitting tensor $D = 2.87$ GHz[31,109] [Figure 40(a)]. In order to identify the NV⁻ center in diamond, ESR measurements were performed. The copper wire was placed very closed to the irradiated area as shown in Figure 40(b) and the microwave signal was frequency swept. In Figure 40(c), the ESR measurements are depicted for the different doses and show a blue shift in the resonance frequency. As the dose goes up, the ESR frequency increases from 2.87 GHz by an amount up to 18 MHz or 0.7%, as shown in Figure 40(d) and the linewidth broadens up to 22.3% (Table 3) and finally disappears at a dose 6.39×10^{20}e$^-$/cm$^2\cdot$s.

Since the ESR linewidth broadening was reported during diamond to graphite conversion[110,111], the ESR shift may come from a change in lattice constant. The loss of ESR is expected to happen as the diamond is graphitized.

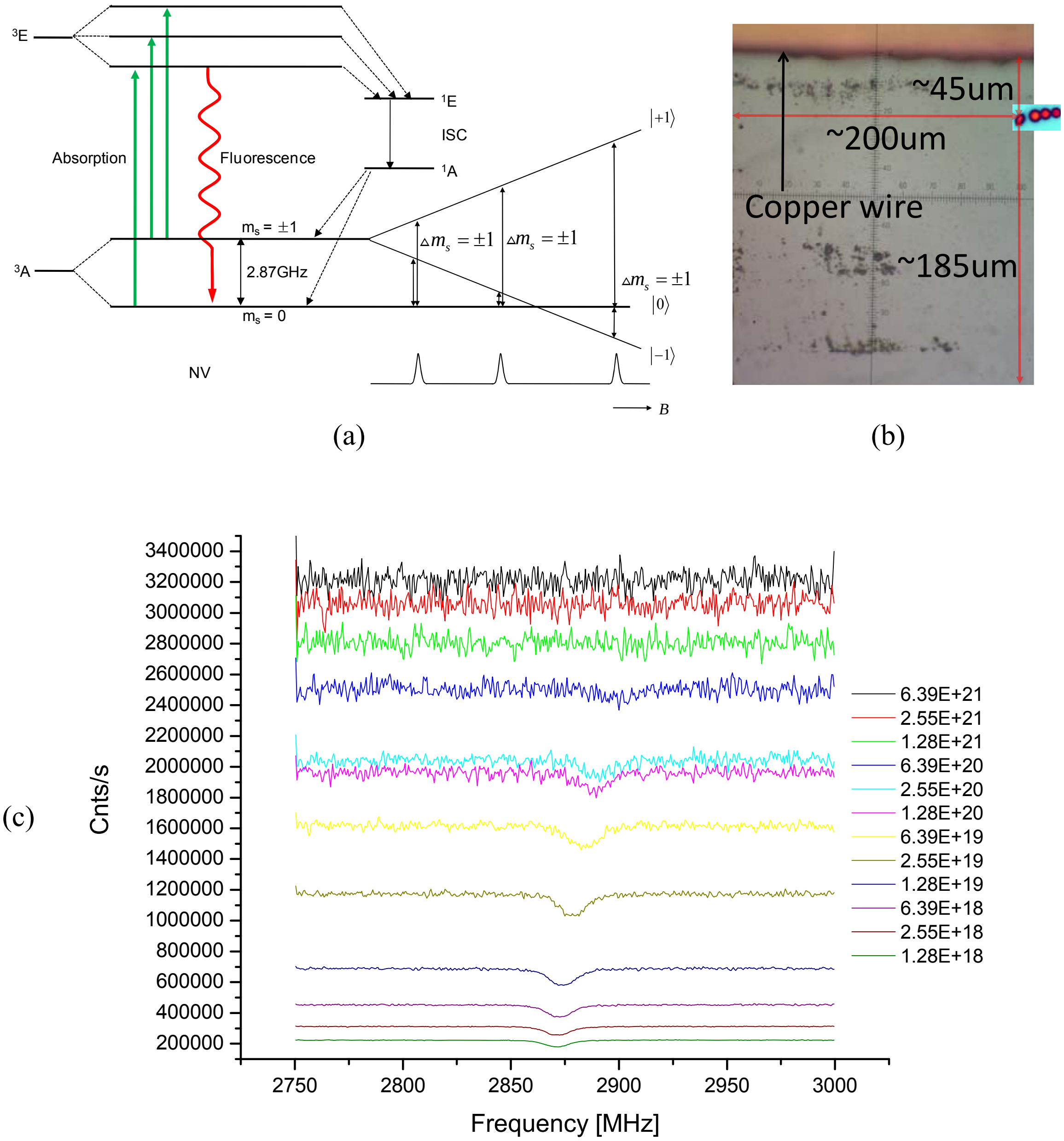

(a)

(b)

(c)

Figure 40. (a) The energy level diagram for the NV⁻ shows 2.87 GHz for the electron resonance frequency. The Zeeman splitting of the NV center is exaggerated for the purpose of the illustration. (b) The wire is located very close to the irradiated spots to apply the microwave signals and is parallel to the series of irradiated spots. (c) The CW ESR measurements are obtained using the same microwave power, $P_{mw} = 25$ dBm. The electron spin resonance frequency for the NV center increases as the dosage gets higher and eventually the resonance disappears. (d) The electron spin resonance frequency shifts up as the dose increases. This shift can be explained by the distortion in the diamond lattice structure caused by the electron irradiation.

(d)

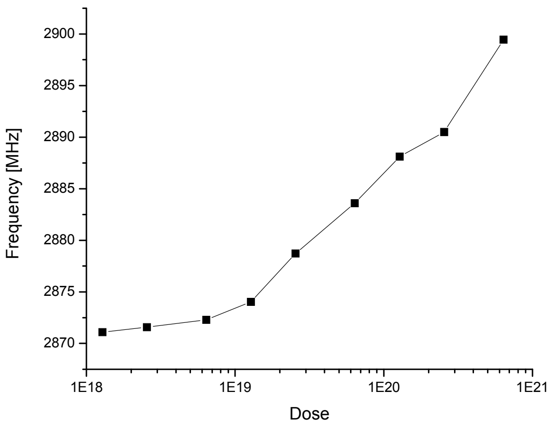

Figure 40 Continued

Table 3. The characterized data for the CW ESR are obtained from each measurement in Figure 40(c).

Dose [e-/cm^2]	CW ESR f_c [MHz]	FWHM [MHz]	Height [cnts/s]
1.28E+18	2871.10	14.59	-42230.34
2.55E+18	2871.57	14.94	-54321.82
6.39E+18	2872.29	15.09	-77953.39
1.28E+19	2874.02	16.04	-106075.99
2.55E+19	2878.72	15.20	-140101.96
6.39E+19	2883.60	17.55	-137190.15
1.28E+20	2888.12	16.73	-116490.71
2.55E+20	2890.49	17.13	-100723.33
6.39E+20	2899.46	18.77	-66529.47
1.28E+21	–	–	–
2.55E+21	–	–	–
6.39E+21	–	–	–

5.4 Conclusion

After irradiation and annealing at 700°C, the NV^0 and NV^- concentrations in the type-Ib diamond are estimated from the photo-emission spectra for the varying irradiation doses. At doses of $1.02\times10^{20}e^-/cm^2\cdot s$ for NV^- and $6.27\times10^{20}e^-/cm^2\cdot s$ for NV^0 the concentrations saturate. The irradiation also causes the NV^- ESR frequency to upshift by 18 MHz, possibly due to diamond lattice swelling. Eventually graphitization of the diamond causes the loss of the ESR signal.

Irradiation temperature is one of factors to control the irradiation damage for diamond. Steeds *et al* performed their experiments at low temperature and showed the temperature dependency of the defect centers. Since the high temperature ion implantation can avoid graphitization[112], this should be pursued to determine the effect on NV^- and NV^0 conversion efficiency as well as NV^- ESR properties.

CHAPTER VI

CONCLUSION

6.1 Summary and Future Work

Three different applications using the CW and pulsed ESR spectroscopy techniques were performed. For the 2D imaging, the Rabi oscillations were measured to resolve the double NVs using two pairs of gold wires. The metal structure was fabricated directly on the diamond surface with the microfabrication technology. The 2D imaging covers the limitation of 1D imaging and provides spatial resolution for the irresolvable NVs. In order to improve the 2D imaging, a better magnetic field modeling may be needed to anticipate the field orientation and intensity with more accuracy. Using a smaller metal structure and a pure diamond with less impurities, the spatial resolution will be improved down to a few nm.

The rotating field was used to suppress the electron spin linewidth broadening caused by the dipole-dipole coupling between the electron spin of the NV center and the nitrogen electron spin. The 50% line width narrowing was observed and subsequently the 30% improvement of the sensitivity was achieved. The rotating field needs to be improved in the intensity and shape. By removing the central two wires, the field may be more axially symmetric and the distance between the center to the wires will be also reduced. Using the higher field intensity, the electron spin linewidth narrowing can be obtained hopefully down to the ^{13}C limit.

The electron irradiation on the type Ib bulk diamond was studied using the wide range of the electron dose with TEM. The NV^- and NV^0 concentrations were characterized and their saturation was observed along with the NV^0 fraction obtained up to ~55%. Using the CW ESR experiments, the ESR resonance frequency shift was found by 18 MHz. The spectral dependence on the temperature was reported, thus, the conversion efficiency from the substitutional nitrogen to the NV center can be improved using the heating stage during the electron irradiation. The ESR resonance frequency can be prevented using the heating to avoid the graphitization at the high doses.

REFERENCES

[1] G. E. Moore, Electronics, **38**, 114 (1965).

[2] D. D. Awschalom, R. A. Buhrman, J. M. Daughton, S. von Molnár, and M. L. Roukes (Eds.), *Spin Electronics* (Kluwer Academic Publishers, Norwell, MA, 2004).

[3] S. A. Wolf, D. D. Awschalom, R. A. Buhrman, J. M. Daughton, S. von Molnar, M. L. Roukes, A. Y. Chtchelkanova, and D. M. Treger, Science **294**, 1488 (2001).

[4] T. Dietl, D. D. Awschalom, M. Kaminska, and H. Ohno (Eds.), *Spintronics, Volume 82: Semiconductors and Semimetals* (Elsevier, Amsterdam, 2008).

[5] J. Berezovsky, M. H. Mikkelsen, O. Gywat, N. G. Stoltz, L. A. Coldren, and D. D. Awschalom, Science **314**, 1916 (2006).

[6] M. H. Mikkelsen, J. Berezovsky, N. G. Stoltz, L. A. Coldren, and D. D. Awschalom, Nature Physics **3**, 770 (2007).

[7] R. C. Myers, M. H. Mikkelsen, J. M. Tang, A. C. Gossard, M. E. Flatte, and D. D. Awschalom, Nature Materials **7**, 203 (2008).

[8] T. Gaebel, M. Domhan, I. Popa, C. Wittman, P. Neumann, F. Jelezko, J. R. Rabeau, N. Stavrias, A. D. Greentree, S. Prawer, J. Meijer, J. Twamley, P. R. Hemmer, and J. Wrachtrup. Nature Physics **2**, 408 (2006).

[9] F. Jelezko, T. Gaebel, I. Popa, M. Domhan, A. Gruber, and J. Wrachtrup, Phys. Rev. Lett. **93**, 130501 (2004).

[10] D. D. Awschalom, R. A. Buhrman, J. M. Daughton, S. von Molnár, and M. L. Roukes (Eds.), *Spin Electronics* (Kluwer Academic Publishers, Norwell, MA, 2004).

[11] R. Proksch, Curr. Opinion Sol. State & Mat. Sci. **4**, 231 (1999).

[12] J. R. Kirtley and J.P. Wikswo, Ann. Rev. Mat. Sci. **29**, 117 (1999).

[13] D. D. Awschalom, R. Epstein, and R. Hanson, Scientific American **297**, 84 (2007).

[14] D. E. Chang, A. S. Sørensen, E. A. Demler, and M. D. Lukin, Nature Physics **3**, 807 (2007).

[15] M. V. Gurudev Dutt, L. Childress, L. Jiang, E. Togan, J. Maze, F. Jelezko, A. S. Zibrov, P. R. Hemmer, and M. D. Lukin, Science **316**, 1312 (2007).

[16] G. Balasubramanian, I. Y. Chan, R. Kolesov, M. Al-Hmoud, J. Tisler, C. Shin, C. Kim, A. Wojcik, P. R. Hemmer, A. Krueger, T. Hanke, A. Leitenstorfer, R. Bratschitsch, F. Jelezko, and J. Wrachtrup, Nature **455**, 648 (2008).

[17] D. P. Divincenzo, Fortschr. Phys. **48**, 771 (2000).

[18] ARDA, *A Quantum Information Science and Technology Roadmap,* http://qist.lanl.gov, 2004.

[19] B. C. Gilbert, M. J. Davies, and D. M. Murphy (Eds.), *Electron Paramagnetic Resonance Vol. 20* (The Royal Society of Chemistry, Cambridge, UK, 2007).

[20] A. M. Chang, H. D. Hallen, L. Harriot, H. F. Hess, H. L. Loa, J. Kao, R. E. Miller, and T. Y. Chang, Appl. Phys. Lett. **61**, 1974 (1992).

[21] Z. Zhang, P. C. Hammel, and P. E. Wigen. Appl. Phys. Lett. **68**, 2005 (1996).

[22] J. M. Taylor, P. Cappellaro, L. Childress, L. Jiang, D. Budker, P. R. Hemmer, A. Yacoby, R. Walsworth, and M. D. Lukin, Nature Physics **4**, 810 (2008).

[23] L. du Preez, PhD Thesis, Univ. of Witwatersrand, South Africa, 1965.

[24] A. Beveratos, R. Brouri, T. Gacoin, A. Villing, J. P. Poizat, and P. Grangier, Phys. Rev. Lett. **89**, 187901 (2002).

[25] A. Drabenstedt, L. Fleury, C. Tietz, F. Jelezko, S. Kilin, A. Nizovtzev, and J. Wratchup, Phys. Rev. B **60**, 11503 (1999).

[26] S. Kuhn, C. Hettich, C. Schmitt, J.-Ph. Poizat, and V. Sandoghdar, J. Micros. **202**, 2 (2000).

[27] F. T. Charnock and T. A. Kennedy, Phys. Rev. B **64**, 041201 (2001).

[28] G. Davies and M. F. Hamer, Proc. R. Soc. A **348**, 285 (1976).

[29] N. R. S. Reddy, N. B. Manson, and E. R. Krausz, J. Lumin. **38**, 46 (1987).

[30] D. A. Redman, S. Brown, R. H. Sands, and S. C. Rand, Phys. Rev. Lett. **67**, 3420 (1991).

[31] J. H. N. Loubser and J. A. van Wyk, Rep. Prog. Phys. **41**, 1201 (1978).

[32] E. van Oort, N. B. Manson, and M. Glasbeek, J. Phys. C **21**, 4385 (1988).

[33] N. B. Manson, X. -F. He, and P. T. H. Fisk, Opt. Lett. **15**, 1094 (1990).

[34] A. T. Collins, M. F. Thomaz, and M. I. B. Jorge, J. Phys. C. Solid State Phys. **16**, 2177 (1983).

[35] J. P. Goss, R. Jones, P. R. Briddon, G. Davies, A. T. Collins, A. Mainwood, J. A. van Wyk, J. M. Baker, M. E. Newton, A. M. Stoneham, and S. C. Lawson, Phys. Rev. B **56**, 16031 (1997).

[36] Y. Mita, Phys. Rev. B **53**, 11360 (1996).

[37] F. Treussarta, V. Jacquesa, E. Wua, T. Gacoinb, P. Grangierc, and J.-F. Rocha, Physica B: Cond. Matt. **376**, 926 (2006).

[38] G. Davies, S.C. Lawson, A.T. Collins, A. Mainwood, and S.J. Sharp, Phys. Rev. B **46**, 13157 (1992).

[39] F. Jelezko, C. Tietz, A. Gruber, I. Popa, A. Nizovtsev, S. Kilin, and J. Wrachtrup, Single Mol. **2**, 255 (2001).

[40] J. H. N. Loubser and J. A. van Wyk, *Diamond Research, vol. 11* (Industrial Diamond Information Bureau, London, 1977).

[41] J. P. D. Martin, J. Lumin. **81**, 237 (1999).

[42] D. A. Redman, S. Brown, R. H. Sands, and S. C. Rand, Phys. Rev. Lett. **67**, 3420 (1991).

[43] L. J. Rogers, S. Armstrong, M. J. Sellars, and N. B. Manson, New J. Phys. **10**, 103024 (2008).

[44] E. van Oort and M. Glasbeek, Chem. Phys. **143**, 131 (1990).

[45] F. Jelezko, and J. Wrachtrup, Physica Status Solidi (a) **203**, 3207 (2006).

[46] F. Jelezko, T. Gaebel, I. Popa, A. Gruber, and J.Wrachtrup, Phys. Rev. Lett. **92**, 076401 (2004).

[47] A. Schweiger and G. Jaschke, *Priciples of Pulse Electron Resonance* (Oxford University Press, Oxford, UK, 2001).

[48] J. A. Weil and J. R. Bolton, *Electron Paramagnetic Resonance*, 2nd Ed. (Wiley, New York, 2007).

[49] M. Brustolon and E. Giamello (Eds.), *Electron Paramagnetic Resonance: A Practitioner's Toolkit* (John Wiley & Sons, Hoboken, NJ, 2009).

[50] K. Holliday, N. B. Manson, M. Glasbeek, and E. van Oort, J. Phys. Condens. Matter Phys. **1**, 7093 (1989).

[51] A. Fujishima, Y. Einaga, T. N. Rao and D. A. Tryk, *Diamond Electrochemistry* (Elsevier Science, Amsterdam, 2005).

[52] A. Schweiger and G. Jeschke, *Principles of Pulse Electron Paramagnetic Resonance* (Oxford University Press, Oxford, UK, 2001).

[53] F. T. Charnock and T. A. Kennedy, Phys. Rev. B **64**, 041201 (2001).

[54] X. -F. He, N. B. Manson, and P. T. H. Fisk, Phys. Rev. B **47**, 8809 (1993).

[55] J. R. Rabeau, P. Reichart, G. Tamanyan, D. N. Jamieson, S. Prawer, F. Jelezko, T. Gaebel, I. Popa, M. Domhan, and J. Wrachtrup, Appl. Phys. Lett. **88**, 023113 (2006).

[56] I. Popa, T. Gaebel, M. Domhan, C. Wittmann, F. Jelezko, and J. Wrachtrup, Phys. Rev. B **70**, 201203(R) (2004).

[57] J. Wrachtrup, S. Y. Kilin, and A. P. Nizovtsev, Optics and Spectroscopy **91**, 429. (2001).

[58] J. Harrison, M. J. Sellars, and N. B. Manson, J. Lumin. **107**, 245 (2004).

[59] J. Harrison, M. J. Sellars, and N. B. Manson, Diamond Relat. Mater. **15**, 586 (2006).

[60] L. Mandel and E. Wolf, *Optical Coherence and Quantum Optics* (Cambridge University Press, Cambridge, UK, 1995).

[61] M. O. Scully and M. S. Zubairy. *Quantum Optics* (Cambridge University Press, Cambridge, UK, 1997).

[62] A. Abragam and B. Bleaney, *Electron Paramagnetic Resonance of Transition Ions* (Clarendon, Oxford, UK, 1970).

[63] F. Gerson and W. Huber, *Electron Spin Resonance Spectroscopy of Organic Radicals* (Wiley, Darmstadt, Germany, 2003).

[64] G. Balasubramanian, P. Neumann, D. Twitchen, M. Markham, R. Kolesov, N. Mizuochi, J. Isoya, J. Achard, J. Beck, J. Tissler, V. Jacques, P. R. Hemmer, F. Jelezko, and J. Wrachtrup, Nature Materials, **8**, 383 (2009).

[65] M. H. Levitt, *Spin Dynamics Basics of Nuclear Magnetic Resonance*, 2nd Ed. (Wiley, Chichester, UK, 2008).

[66] J. Wrachtrup and F. Jelezko, J. Phys. Condens. Matter **18**, S807 (2006).

[67] J. R. Maze, P. L. Stanwix, J. S. Hodges, S. Hong, J. M. Taylor, P. Cappellaro, L. Jiang, M. V. Gurudev Dutt, E. Togan, A. S. Zibrov, A. Yacoby, R. L. Walsworth, and M. D. Lukin, Nature **455**, 644 (2008).

[68] S.-J. Yu, M.-W. Kang, H.-C. Chang, K.-M. Chen, and Y.-C. Yu, J. Am. Chem. Soc. **127**, 17604 (2005).

[69] O. Faklaris, D. Garrot, V. Joshi, F. Druon, J. P. Boudou, T. Sauvage,. P. Georges, P. A. Curmi, and F. Treussart, Small **4**, 2236 (2008).

[70] L. J. Berliner, G. R. Eaton, and S. S. Eaton (Eds.), *Distance Measurements in Biological Systems by EPR* (Kluwer, New York, 2002).

[71] G. Donnert, J. Keller, R. Medda, M. A. Andrei, S. O. Rizzoli, R. Luhrmann, R. Jahn, C. Eggeling, and S. W. Hell, PNAS **103**, 11440 (2006).

[72] B. Harke, J. Keller, C. K. Ullal, V. Westphal, A. Schönle, and S. W. Hell, Optics Express **16**, 4154 (2008).

[73] B. Hein, K. I. Willing, and S. W. Hell, PNAS **105**, 14271 (2008).

[74] S. Schlick and M. V. Motyakin, in *Electron Paramagnetic Resonance Vol. 20*, edited by B. C. Gilbert, M. J. Davies, and D. M. Murphy (The Royal Society of Chemistry, Cambridge, UK, 2007).

[75] M. J. R. Hoch and A. R. Day, Solid State Commun. **30**, 211 (1979).

[76] C. S. Adams, M. Sigel, and J. Mlynek, Phys. Rep. **240**, 143 (1994).

[77] M. Drndic, K. S. Johnson, J. H. Thywissen, M. Prentiss, and R. M. Westervelt, Appl. Phys. Lett. **72**, 2906 (1998).

[78] R. Narkowicz , D. Suter, and R. Stonies, J. Magn. Reson. **175**, 275 (2005).

[79] G. Boero, J. Frounchi, B. Furrer, P.-A. Besse, and R. S. Popovic, Rev. Sci. Instrum. **72**, 2764 (2001).

[80] J. Clarke and A.I. Braginski (Eds.), *The SQUID Handbook Vol. I Fundamentals and Technology of SQUIDs and SQUID Systems* (Wiley-VCH, Weinheim, Germany, 2004).

[81] V. Shah, S. Knappe, P. D. D. Schwindt, and J. Kitching, Nature Photonics **1**, 649 (2007).

[82] S.-K. Lee, K. L. Sauer, S. J. Seltzer, O. Alem, and M. V. Romalis, Applied Physics Letters **89**, 214106 (2006).

[83] S. Koizumi, C. E. Nebel, and M. Nesladek (Eds.), *Physics and Applications of CVD Diamond* (Wiley-VCH, Weinheim, Germany, 2008).

[84] R. Hanson, Nature Materials **8**, 368 (2009).

[85] V. M. Acosta, E. Bauch, M. P. Ledbetter, C. Santori, K. M. C. Fu, P. E. Barclay, R. G. Beausoleil, H. Linget, J. F. Roch, F. Treussart, S. Chemerisov, W. Gawlik, and D. Budker, Phys. Rev. B **80**, 115202 (2009).

[86] C. A. Meriles, D. Sakellariou, A. Moulé, M. Goldman, T. Budinger and A. Pines, J. Magn. Reson. **169**, 13 (2004).

[87] D. Sakellariou, C. Meriles, R. Martin, and A. Pines, Magn. Reson. Imag. **23**, 295 (2005).

[88] E. van Oort and M. Glasbeek, Chem. Phys. **152**, 365 (1991).

[89] J. H. van Vleck, Phys. Rev. **74**, 1168 (1948).

[90] A. Abragam, *The Principles of Nuclear Magnetism* (Clarendon Press, Oxford, UK, 1961).

[91] C. P. Slichter, *Principles of Magnetic Resonance,* 3rd Ed. (Springer, Berlin, Heidelberg, Germany, 1990).

[92] G. Jeschke and H. W. Spiess, in *Novel NMR and EPR Techniques*, Lecture Notes in Physics, edited by J. Dolinsek, M. Vilfan, and S. Zumer (Springer, Berlin, 2006).

[93] D. Hessinger, C. Bauer, M. Hubrich, G. Jeschke, and H. W. Spiess, J. Magn. Reson. **147**, 217 (2000).

[94] N. D. Bhaskar, J. Camparo, W. Happer, and A. Sharma, Phys. Rev. A **23**, 3048 (1981).

[95] D. Budker and M. V. Romalis, Optical Magnetometry, Nature Physics **3**, 227 (2007).

[96] M. H. Levitt, *Spin Dynamics Basics of Nuclear Magnetic Resonance*, 2nd Ed. (Wiley, Chichester, UK, 2008).

[97] I. J. Lowe. Phys. Rev. Lett. **2**, 285 (1959).

[98] A. D. Bain and R. S. Dumont, Concepts Magn. Reson. **13**, 159 (2001).

[99] J. Koike, D. M. Parkin, and T. E. Mitchell, Appl. Phys. Lett. **60**, 1450 (1992).

[100] J. W. Steeds, S. Charles, T. J. Davis, A. Gilmore, J. Hayes, D. Pickard, and J. E. Butler, Diamond Relat. Mater. **8**, 94 (1999).

[101] J. W. Steeds, S. J. Charles, J. Davies, and I. Griffin, Diamond. Relat. Mater. **9**, 397 (2000).

[102] B. Campbell and A. Mainwood, Phys. Status Solidi A **181**, 99 (2000).

[103] G. Davies, S. C. Lawson, A. T. Collins, A. Mainwood, and S.J. Sharp, Phys. Rev. B **46**, 13157 (1992).

[104] A. T. Collins, J. Phys. C: Solid State Phys. **11**, L417 (1978).

[105] A. T. Collins, J. Phys. C: Solid State Phys. **13**, 2641 (1980).

[106] A. Uedono, K. Mori, N. Morishita, H. Itoh, S. Tanigawa, S. Fujii, and S. Shikata, J. Phys. Condens. Matter. **11**, 4925 (1999).

[107] J. Martin, R. Wannemacher, J. Teichert, L. Bischoff, and B. Köhler, Appl. Phys. Lett. **75**, 3096 (1999).

[108] A. Hoffman, S. Prawer, and R. Kalish, Phys. Rev. B **45**, 12736 (1992).

[109] L. J. Rogers, S. Armstrong, M. J. Sellars, and N. B. Manson, New J. Phys. **10**, 103024 (2008).

[110] B. L. V. Prasad, H. Sato, T. Enoki, Y. Hishiyama, Y. Kaburagi, A. M. Rao, P. C. Eklund, K. Oshida, and M. Endo, Prasad Phys. Rev. B **62**, 11209 (2000).

[111] T. Enoki, Phys. Solid State, **46**, 651 (2004).

[112] G. Braunstein and R. Kalish, Appl. Phys. Lett. **38**, 416 (1981).

APPENDIX A

THEORETICAL BACKGROUND OF ELECTRON PARAMAGNETIC RESONANCE[†]

A.1 Angular Momentum

The Hamiltonian operator for the total energy, H, is expressed by

$$H\psi_i = E_i\psi_i \tag{31}$$

where ψ_i is the energy eigenfunction for a particular system and E_i is the exact total energy for the ith state of the system. The energy for a given Hamiltonian is obtained from multiplying both sides by ψ_i^* and integrating in the complete range of the spatial variables. Assuming $|\psi_i\rangle$ is expressed as the linear combination of the orthogonal set of $|\varphi_i\rangle$'s, the Hamiltonian matrix (also called the energy matrix) is constructed as

---

[†] This review covers the brief summary of fundamental theory and topics on the electron paramagnetic resonance which could be found in many books of this subject as listed below:
B. C. Gilbert, M. J. Davies, and D. M. Murphy (Eds.), *Electron Paramagnetic Resonance Vol. 20* (The Royal Society of Chemistry, Cambridge, UK, 2007); F. Gerson and W. Huber, *Electron Spin Resonance Spectroscopy of Organic Radicals* (Wiley, Darmstadt, Germany, 2003); J. A. Weil and J. R. Bolton, *Electron Paramagnetic Resonance*, 2nd Ed. (Wiley, New York, 2007); L. J. Berliner, G. R. Eaton, and S. S. Eaton (Eds.), *Distance Measurements in Biological Systems by EPR* (Kluwer, New York, 2002); M. A. Hemminga and L. J. Berliner (Eds.), *ESR Spectroscopy in Membrane Biophysics* (Springer, New York, 2007); M. Brustolon and E. Giamello (Eds.), *Electron Paramagnetic Resonance: A Practitioner's Toolkit* (John Wiley & Sons, Hoboken, NJ, 2009); P. Blumler, B. Blumich, R. Botto, and E. Fukushima (Eds.), *Spatially Resolved Magnetic Resonance* (Wiley-VCH, Weinheim, Germany, 1998); Philip Rieger, *Electron Spin Resonance: Analysis and Interpretation* (RSC Publishing, Cambridge, UK, 2007); W. R. Hagen, *Biomolecular EPR Spectroscopy* (CRC Press, Boca Raton, FL, 2009).

$$H = \begin{bmatrix} a_{11} & \cdots & a_{1n} \\ \vdots & \ddots & \vdots \\ a_{n1} & \cdots & a_{nn} \end{bmatrix} \tag{32}$$

where $a_{ij} = \langle \varphi_j | H | \varphi_i \rangle$.

When the square of the total angular momentum, $J^2 = \mathbf{J}^T\mathbf{J}$, is applied to ψ_i, it can produce the constant of motion, λ_i, as given below:

$$J^2 \psi_i = \lambda_i \psi_i \tag{33}$$

where the eigenvalue λ_i is given in the unit of $\hbar^2$. When $\mathbf{J}$ represents the orbital angular momentum, λ_i is found to be a function of the quantum number j, which is an integer. For the spin angular momentum, the quantum number j is a half-integer. For an integer or half-integer j, the allowed m-values are given by

$$m = -j, -j+1, \cdots, j+1, j \tag{34}$$

and there exist the complete orthogonal set of $2j+1$ states associated with the values m. Considering $|\varphi_i\rangle = | j,m\rangle$, $\mathbf{J}^2$ and J_z which can be diagonalized with $\mathbf{J}^2$ are expressed with the eigenvalue and eigenstate as[1]

$$\begin{aligned} \mathbf{J}^2 | j,m\rangle &= j(j+1) | j,m\rangle \\ J_z | j,m\rangle &= m | j,m\rangle \end{aligned} \tag{35}$$

The ladder operator J_+ and J_- are defined by the linear combination of J_x and J_y:

$$\begin{aligned} J_+ &\equiv J_x + iJ_y \\ J_- &\equiv J_x - iJ_y \end{aligned} \tag{36}$$

By convention, J_+ and J_- are written as

$$\begin{aligned} J_+ \mid j,m\rangle &= \sqrt{j(j+1)-m(m+1)} \mid j,m+1\rangle = \sqrt{(j-m)(j+m+1)} \mid j,m+1\rangle \\ J_- \mid j,m\rangle &= \sqrt{j(j+1)-m(m-1)} \mid j,m-1\rangle = \sqrt{(j+m)(j-m+1)} \mid j,m-1\rangle \end{aligned} \tag{37}$$

When there exist two angular momentums, the total angular momentum is given by

$$\mathbf{J} = \mathbf{J}_1 + \mathbf{J}_2 \tag{38}$$

where $\mathbf{J}_1$ and $\mathbf{J}_2$ are the angular momentum operators for two particles. Since $\mathbf{J}_1$ and $\mathbf{J}_2$ commute, $\mathbf{J}_1^T\mathbf{J}_2$ is obtained by

$$\mathbf{J}_1^T\mathbf{J}_2 = \tfrac{1}{2}(\mathbf{J}^2 - \mathbf{J}_1^2 - \mathbf{J}_2^2) \tag{39}$$

A.2 Magnetic Dipole Moment

The magnetic dipole moment, μ, is one of very important quantities in the magnetic resonance. The magnetic moment is proportional to the angular momentum of the magnetic species like nuclei and electrons and is given by

$$\boldsymbol{\mu} = \alpha g \beta \mathbf{J} = \gamma \hbar \mathbf{J} \tag{40}$$

Here, the factor α is ± 1, the dimensionless g factor is the Zeeman splitting constant for the each species, β is the same dimensioned factor as $\boldsymbol{\mu}$ called the magnetron, γ is the gyromagnetic ratio and $\mathbf{J}$ is the dimensionless angular momentum vector.

For electrons, $\alpha_e = -1$, the free-electron Zeeman factor is[2]

$$g_e = 2.0023, \tag{41}$$

the Bohr magnetron is

$$\beta_e = \frac{e\hbar}{2m_e} = 9.2740 \times 10^{-24}\,\mathrm{J/T} \tag{42}$$

where e is the electron charge and m_e is the mass of the electron, and $\mathbf{J}$ is the electron spin operator $\mathbf{S}$. In general, the electron Zeeman factor, g for the electrons interacting with other particles is not equal to g_e. The gyromagnetic ratio of the free electron is

$$\gamma_e = -g_e\beta_e / \hbar = -1.7609 \times 10^{11}\,\mathrm{s^{-1}T^{-1}} \tag{43}$$

For nuclei, $\alpha_n = +1$, the nuclear magnetron is

$$\beta_n = \frac{e\hbar}{2m_p} = 5.0508 \times 10^{-27}\,\mathrm{J/T} \tag{44}$$

where m_p is the mass of the proton, and $\mathbf{J}$ is the nuclear spin operator $\mathbf{I}$. The nuclear g factor g_n is different for each nucleus and the nuclear gyromagnetic ration is given by

$$\gamma_n = g\beta_n / \hbar \tag{45}$$

The energy of a magnetic dipole moment $\boldsymbol{\mu}$ in a field $\mathbf{B}$ [Figure 41] is defined by

$$E = -\boldsymbol{\mu}^{\mathrm{T}} \cdot \mathbf{B} = -\mathbf{B}^{\mathrm{T}} \cdot \boldsymbol{\mu} = -\mu B \cos\theta = -B\mu_z \tag{46}$$

where θ is the angle between the magnetic field and the magnetic dipole moment.

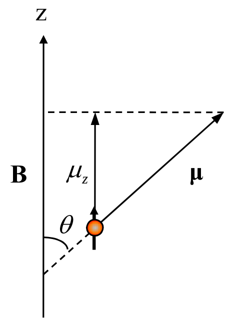

Figure 41. Energy of a magnetic dipole in an external magnetic field B.

A.3 Spin Hamiltonian

Electron and Nuclear Zeeman Splitting

The interaction of an electron or a nucleus with a static magnetic field $\mathbf{B}\,(\|\,\mathbf{z})$ is expressed in

$$H = -\mathbf{B}^{\mathrm{T}} \cdot \boldsymbol{\mu} = -B\mu_z \tag{47}$$

Considering $\mu_{ez} = -g\beta_e S_z$ and $\mu_{nz} = g_n\beta_n I_z$ from A.2, Equation 47 becomes the electron and nuclear spin Hamiltonians defined by

$$H_e = g\beta_e B S_z \tag{48}$$

$$H_n = -g_n\beta_n B I_z \tag{49}$$

and it shows that electron and nuclear Zeeman interactions have opposite sign. For the simplest system with a single electron spin $S = \frac{1}{2}$ or with a nuclear spin $I = \frac{1}{2}$ placed in a magnetic field, the spin Hamiltonians can be expressed equivalently in Dirac notation by

$$H_e \left|\pm\tfrac{1}{2}\right\rangle_e = \pm\tfrac{1}{2} g\beta_e B \left|\pm\tfrac{1}{2}\right\rangle_e \tag{50}$$

$$H_n \left|\pm\tfrac{1}{2}\right\rangle_n = \mp\tfrac{1}{2} g_n\beta_n B \left|\pm\tfrac{1}{2}\right\rangle_n \tag{51}$$

where $\left|\pm\tfrac{1}{2}\right\rangle_e$ and $\left|\pm\tfrac{1}{2}\right\rangle_n$ are the corresponding eigenfunctions of the possible electron and nuclear spin quantum numbers, $m_S = \pm\frac{1}{2}$ and $m_I = \pm\frac{1}{2}$. Thus, the Zeeman energies $E_{e\pm\frac{1}{2}}$ and $E_{n\pm\frac{1}{2}}$ for $m_S = \pm\frac{1}{2}$ and $m_I = \pm\frac{1}{2}$ are obtained by [see Figure 42]

$$E_{e\pm\frac{1}{2}} = \left\langle \pm\tfrac{1}{2}\right| H_e \left|\pm\tfrac{1}{2}\right\rangle = \pm\tfrac{1}{2} g\beta_e B \tag{52}$$

$$E_{n\pm\frac{1}{2}} = \left\langle \pm\tfrac{1}{2}\right| H_n \left|\pm\tfrac{1}{2}\right\rangle = \mp\tfrac{1}{2} g_n\beta_n B \tag{53}$$

The energy differences between two levels

$$\Delta E_e = E_{e+\frac{1}{2}} - E_{e-\frac{1}{2}} = g_e \beta_e B = h\nu_e \tag{54}$$

$$\Delta E_n = E_{n-\frac{1}{2}} - E_{n+\frac{1}{2}} = g_n \beta_n B = h\nu_n \tag{55}$$

correspond to the electronic and nuclear transitions induced by an electromagnetic field matching the photon energies, $h\nu$.

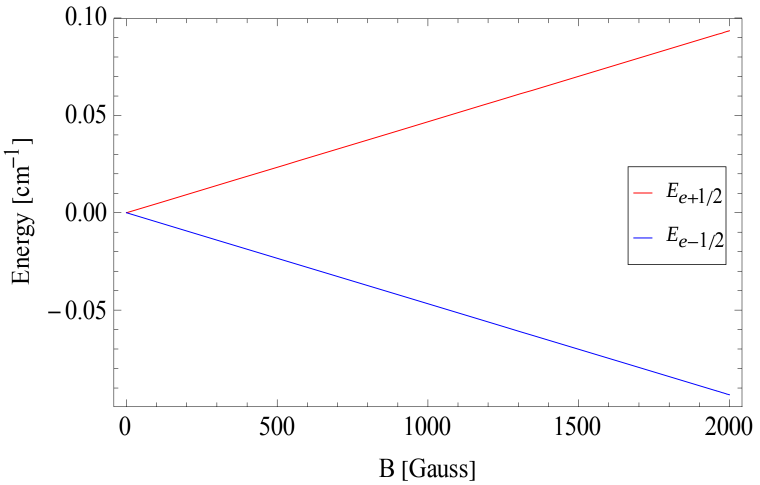

Figure 42. Energy levels of an electron in a magnetic field for a S=1/2 system.

Hyperfine Interaction

The unpaired electron interacting with neighboring nuclear dipole moments causes the splitting of the resonance called nuclear hyperfine interaction. The hyperfine interaction can be isotropic or anisotropic according to the dependency on the orientation of the magnetic field with respect to the molecular axis. In the absence of anisotropy, the hyperfine coupling is expressed by

$$H_{A_0} = A_0 \mathbf{S}^{\mathrm{T}} \cdot \mathbf{I} \tag{56}$$

where the isotropic hyperfine coupling constant A_0 is

$$A_0 = \frac{2\mu_0}{3} g\beta_e\beta_n |\psi(0)|^2 \tag{57}$$

and $|\psi(0)|^2$ is the probability of finding the electron at the nuclear point[3].

The spin Hamiltonian for the system with one unpaired electron and one nucleus with $I = \frac{1}{2}$ is expressed by the sum of the electron and nuclear spin Hamiltonians and the hyperfine interaction:

$$H = g\beta_e \mathbf{B}^{\mathrm{T}} \cdot \mathbf{S} - g_n\beta_n \mathbf{B}^{\mathrm{T}} \cdot \mathbf{I} + A_0 \mathbf{S}^{\mathrm{T}} \cdot \mathbf{I} \tag{58}$$

If the magnetic field is taken along z, the spin Hamiltonian becomes

$$\begin{aligned} H &= g\beta_e B S_z - g_n\beta_n B I_z + A_0(S_z I_z + S_x I_x + S_y I_y) \\ &= g\beta_e B S_z - g_n\beta_n B I_z + A_0[S_z I_z + \tfrac{1}{2}(S_+ I_- + S_- I_+)] \end{aligned} \tag{59}$$

where $S_+ = S_x + iS_y$ and $S_- = S_x - iS_y$.

For the system with $S = \frac{1}{2}$ and $I = \frac{1}{2}$, there exist four spin states represented in $|m_S, m_I\rangle$ which are $|+\frac{1}{2},+\frac{1}{2}\rangle$, $|+\frac{1}{2},-\frac{1}{2}\rangle$, $|-\frac{1}{2},+\frac{1}{2}\rangle$, and $|-\frac{1}{2},-\frac{1}{2}\rangle$. The energy of each state is computed using the spin Hamiltonian H[4567]:

$$E_{+\frac{1}{2},+\frac{1}{2}} = E_1 = \langle +\tfrac{1}{2},+\tfrac{1}{2}| H |+\tfrac{1}{2},+\tfrac{1}{2}\rangle = +\tfrac{1}{2} g\beta_e B - \tfrac{1}{2} g_n\beta_n B + \tfrac{1}{4} A_0 + \dots \tag{60}$$

$$E_{+\frac{1}{2},-\frac{1}{2}} = E_2 = \langle +\tfrac{1}{2},-\tfrac{1}{2}| H |+\tfrac{1}{2},-\tfrac{1}{2}\rangle = +\tfrac{1}{2} g\beta_e B + \tfrac{1}{2} g_n\beta_n B - \tfrac{1}{4} A_0 + \dots \tag{61}$$

$$E_{-\frac{1}{2},+\frac{1}{2}} = E_4 = \langle -\tfrac{1}{2},+\tfrac{1}{2}| H |-\tfrac{1}{2},+\tfrac{1}{2}\rangle = -\tfrac{1}{2} g\beta_e B - \tfrac{1}{2} g_n\beta_n B - \tfrac{1}{4} A_0 + \dots \tag{62}$$

$$E_{-\frac{1}{2},-\frac{1}{2}} = E_3 = \langle -\tfrac{1}{2},-\tfrac{1}{2}| H |-\tfrac{1}{2},-\tfrac{1}{2}\rangle = -\tfrac{1}{2} g\beta_e B + \tfrac{1}{2} g_n\beta_n B + \tfrac{1}{4} A_0 + \dots \tag{63}$$

If the magnetic field is large enough, the energies become simplified to the first order energies with '$\dots$' terms ignored under the condition of high field approximation, i.e., $g\beta_e B \gg A_0$.

The energy levels are illustrated in Figure 43 and the arrows indicate two transitions subject to the angular momentum selection rules $\Delta m_S = \pm 1$ and $\Delta m_I = 0$. The allowed transition energies are

$$h\nu_1 = E_{+\frac{1}{2},+\frac{1}{2}} - E_{-\frac{1}{2},+\frac{1}{2}} = g\beta_e B + \tfrac{1}{2}A_0 + \dots \tag{64}$$

$$h\nu_2 = E_{+\frac{1}{2},-\frac{1}{2}} - E_{-\frac{1}{2},-\frac{1}{2}} = g\beta_e B - \tfrac{1}{2}A_0 + \dots \tag{65}$$

The hyperfine interacting gives the splitting to each electron Zeeman spin level. Then, the nuclear Zeeman interaction leads to the hyperfine level shift but it has no effect on the energy difference between the levels.

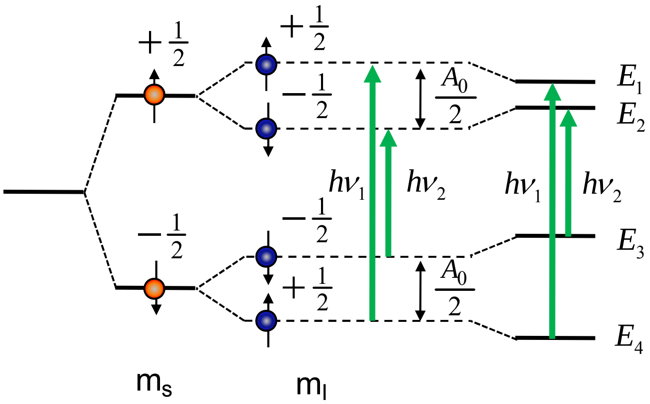

Figure 43. The energy level diagram for a system of electron spin S=1/2 and nuclear spin I=1/2. The red color represents the electron spin components of S=1/2 along the magnetic field while the blue color represents the nuclear spin components.

Spin Hamiltonian for Two Electrons

For the system with two unpaired electrons, the system energy separates into a singlet and a triplet states resulting from the coulombic repulsion called electron exchange interaction. The electron exchange interaction can be expressed by

$$H_J = \mathbf{S_1} \cdot \mathbf{J} \cdot \mathbf{S}_2 = \sum_{i,j} J_{ij} S_{1i} S_{2j} \tag{66}$$

where $i, j = x, y, z$, J_{ij} is the exchange coupling constant and S_1 and S_2 are electron spins for electrons 1 and 2[8,9,10]. The singlet and triplet states are (in the notation of $|S, m_S\rangle$)

$$|0,0\rangle = \tfrac{1}{\sqrt{2}}(|\tfrac{1}{2},-\tfrac{1}{2}\rangle - |-\tfrac{1}{2},\tfrac{1}{2}\rangle) \quad \text{for singlet, } S = 0 \tag{67}$$

and

$$\begin{aligned} |1,+1\rangle &= |\tfrac{1}{2},\tfrac{1}{2}\rangle \\ |1,0\rangle &= \tfrac{1}{\sqrt{2}}(|\tfrac{1}{2},-\tfrac{1}{2}\rangle + |-\tfrac{1}{2},\tfrac{1}{2}\rangle) \quad \text{for triplet, } S = 1 \\ |1,-1\rangle &= |-\tfrac{1}{2},-\tfrac{1}{2}\rangle \end{aligned} \tag{68}$$

If the singlet-triplet splitting is large ($\gg k_b T$) and the triplet state is lower in energy than the singlet, the triplet state ($S = 1$) is populated and the exchange interaction can be safely ignored with the triplet focused on[11].

Another interaction for the two unpaired electrons called the dipole-dipole interaction causes the zero-field splitting to the triplet state in the zero magnetic field. In analogy to the electron nuclear dipole-dipole interaction, the electron-electron dipole interaction is expressed by

$$\begin{aligned} H_D(\mathbf{r}) &= \frac{\mu_0}{4\pi}\left[\frac{\boldsymbol{\mu}_1^{\mathrm{T}}\cdot\boldsymbol{\mu}_2}{r^3} - \frac{3(\boldsymbol{\mu}_1^{\mathrm{T}}\cdot\mathbf{r})(\boldsymbol{\mu}_2^{\mathrm{T}}\cdot\mathbf{r})}{r^5}\right] \\ &= \frac{\mu_0}{4\pi} g_1 g_2 \beta_e^2 \left[\frac{\mathbf{S}_1^{\mathrm{T}}\cdot\mathbf{S}_2}{r^3} - \frac{3(\mathbf{S}_1^{\mathrm{T}}\cdot\mathbf{r})(\mathbf{S}_2^{\mathrm{T}}\cdot\mathbf{r})}{r^5}\right] \end{aligned} \tag{69}$$

where $\boldsymbol{\mu}_1$ and $\boldsymbol{\mu}_2$ are the magnetic dipole moments for electrons 1 and 2, $\mathbf{r}$ is the vector from electron 1 and electron2, g_1 and g_2 are electron g factors and $\mathbf{S}_1$ and $\mathbf{S}_2$ are electron spin operators. By expanding in a three dimensional space, summarizing and integrating over the electron spatial distribution, Equation 69 can be written in the matrix form as:

$$H_D(\mathbf{r}) = \frac{\mu_0}{8\pi}(g\beta_e)^2 \begin{bmatrix} S_x & S_y & S_z \end{bmatrix} \begin{bmatrix} \left\langle \frac{r^2-3x^2}{r^5} \right\rangle & \left\langle \frac{-3xy}{r^5} \right\rangle & \left\langle \frac{-3xz}{r^5} \right\rangle \\ & \left\langle \frac{r^2-3y^2}{r^5} \right\rangle & \left\langle \frac{-3yz}{r^5} \right\rangle \\ & & \left\langle \frac{r^2-3z^2}{r^5} \right\rangle \end{bmatrix} \begin{bmatrix} S_x \\ S_y \\ S_z \end{bmatrix} \tag{70}$$

where the bracket implies averaging over the spatial variables.

Equation 70 can be simplified to the spin Hamiltonian

$$H_D(\mathbf{r}) = \mathbf{S}^T \cdot \mathbf{D} \cdot \mathbf{S} = 2\mathbf{S}_1^T \cdot \mathbf{D} \cdot \mathbf{S}_2 \tag{71}$$

where the factor of 2 is due to the interchange of spins $\mathbf{S}_1$ and $\mathbf{S}_2$. It is noted that the same spin Hamiltonian term can arises from the electron spin-obit interaction[12]. Once $\mathbf{D}$ is diagonalized to $\mathbf{D}_d$, the dipolar interaction can be written by

$$H_D = D_x S_x^2 + D_y S_y^2 + D_z S_z^2 \tag{72}$$

where D_x, D_y, and D_z are diagonal elements of $\mathbf{D}_d$ in the principal-axis system with D_z taken to be the principal value of the largest absolute magnitude and $tr(\mathbf{D}) = D_x + D_y + D_z = 0$ from Equation 70.

The effective spin Hamiltonian for two unpaired electrons is obtained by

$$\begin{aligned} H &= g\beta_e \mathbf{B}^T \cdot \mathbf{S} + \mathbf{S}^T \cdot \mathbf{D} \cdot \mathbf{S} \\ &= g\beta_e (B_x S_x + B_y S_y + B_z S_z) + D_x S_x^2 + D_y S_y^2 + D_z S_z^2 \end{aligned} \tag{73}$$

Equation 73 can be written with two elements of zero-field tensor, $D = \frac{3}{2} D_z$ and $E = \frac{1}{2}(D_x - D_y)$, as

$$H = g\beta_e (B_x S_x + B_y S_y + B_z S_z) + D[S_z^2 - \tfrac{1}{3} S(S+1)] + E(S_x^2 - S_y^2) \tag{74}$$

where $S^2 = S_x^2 + S_y^2 + S_z^2$ and the eigenvalue of S^2 is $S(S+1)$.

The orthogonal basis set for $S = 1$ is

$$\varphi_i = \{\left|+1\right\rangle, \left|0\right\rangle, \left|-1\right\rangle\} \tag{75}$$

and each spin operator is

$$\begin{aligned} S_z \left|+1\right\rangle &= 1\left|+1\right\rangle \\ S_z \left|0\right\rangle &= 0\left|0\right\rangle \\ S_z \left|-1\right\rangle &= -1\left|-1\right\rangle \end{aligned} \tag{76}$$

$$\begin{aligned} S_z^2 \left|+1\right\rangle &= 1S_z \left|+1\right\rangle = 1\left|+1\right\rangle \\ S_z^2 \left|0\right\rangle &= 0S_z \left|0\right\rangle = 0\left|0\right\rangle \\ S_z^2 \left|-1\right\rangle &= -1S_z \left|-1\right\rangle = 1\left|-1\right\rangle \end{aligned} \tag{77}$$

$$\begin{aligned} S_+ \left|0\right\rangle &= \sqrt{1(1+1) - 0(0+1)}\left|+1\right\rangle = \sqrt{2}\left|+1\right\rangle \\ S_+ \left|-1\right\rangle &= \sqrt{1(1+1) - (-1)(-1+1)}\left|0\right\rangle = \sqrt{2}\left|0\right\rangle \end{aligned} \tag{78}$$

$$\begin{aligned} S_-\left|+1\right\rangle &= \sqrt{1(1+1)-1(1-1)}\left|0\right\rangle = \sqrt{2}\left|0\right\rangle \\ S_-\left|0\right\rangle &= \sqrt{1(1+1)-0(0-1)}\left|-1\right\rangle = \sqrt{2}\left|-1\right\rangle \end{aligned} \tag{79}$$

$$S_+^2\left|-1\right\rangle = \sqrt{2}S_+\left|0\right\rangle = 2\left|+1\right\rangle \tag{80}$$

$$S_-^2\left|+1\right\rangle = \sqrt{2}S_-\left|0\right\rangle = 2\left|-1\right\rangle \tag{81}$$

$$\begin{aligned} S_x\left|+1\right\rangle &= (1/2)S_-\left|+1\right\rangle = \sqrt{2}/2\left|0\right\rangle \\ S_x\left|0\right\rangle &= (1/2)S_+\left|0\right\rangle + (1/2)S_-\left|0\right\rangle = \sqrt{2}/2\left|+1\right\rangle + \sqrt{2}/2\left|-1\right\rangle \\ S_x\left|-1\right\rangle &= (1/2)S_+\left|-1\right\rangle = \sqrt{2}/2\left|0\right\rangle \end{aligned} \tag{82}$$

$$\begin{aligned} S_y\left|+1\right\rangle &= (i/2)S_-\left|+1\right\rangle = i\sqrt{2}/2\left|0\right\rangle \\ S_y\left|0\right\rangle &= (-i/2)S_+\left|0\right\rangle + (i/2)S_-\left|0\right\rangle = -i\sqrt{2}/2\left|+1\right\rangle + i\sqrt{2}/2\left|-1\right\rangle \\ S_y\left|-1\right\rangle &= (-i/2)S_+\left|-1\right\rangle = -i\sqrt{2}/2\left|0\right\rangle \end{aligned} \tag{83}$$

$$\begin{aligned} S_x^2\left|+1\right\rangle &= \sqrt{2}/2S_x\left|0\right\rangle = 1/2\left|+1\right\rangle + 1/2\left|-1\right\rangle \\ S_x^2\left|0\right\rangle &= \sqrt{2}/2S_x\left|+1\right\rangle + \sqrt{2}/2S_x\left|-1\right\rangle = \left|0\right\rangle \\ S_x^2\left|-1\right\rangle &= \sqrt{2}/2S_x\left|0\right\rangle = 1/2\left|+1\right\rangle + 1/2\left|-1\right\rangle \end{aligned} \tag{84}$$

$$\begin{aligned} S_y^2\left|+1\right\rangle &= (i\sqrt{2}/2)S_y\left|0\right\rangle = 1/2\left|+1\right\rangle - 1/2\left|-1\right\rangle \\ S_y^2\left|0\right\rangle &= -i\sqrt{2}/2S_y\left|+1\right\rangle + i\sqrt{2}/2S_y\left|-1\right\rangle = \left|0\right\rangle \\ S_y^2\left|-1\right\rangle &= (-i\sqrt{2}/2)S_y\left|0\right\rangle = -1/2\left|+1\right\rangle + 1/2\left|-1\right\rangle \end{aligned} \tag{85}$$

$$\begin{aligned} (S_x^2 - S_y^2)\left|+1\right\rangle &= \left|-1\right\rangle \\ (S_x^2 - S_y^2)\left|0\right\rangle &= 0\left|0\right\rangle \\ (S_x^2 - S_y^2)\left|-1\right\rangle &= \left|+1\right\rangle \end{aligned} \tag{86}$$

and

$$D[S_z^2 - \tfrac{1}{3}S(S+1)]\left|m_S\right\rangle = D(S_z^2 - \tfrac{2}{3})\left|m_S\right\rangle \quad \text{for } S = 1 \tag{87}$$

If the quantization axis of the electron spin, S_z, is taken along the principal axis, Z, the Hamiltonian matrix can be written in the basis set of $\left|+1\right\rangle$, $\left|0\right\rangle$ and $\left|-1\right\rangle$ of S_z as

$$H = \begin{array}{c|ccc} \langle +1| & g\beta_e B_z + \frac{D}{3} & \frac{1}{\sqrt{2}} g\beta_e (B_x - iB_y) & E \\ \langle 0| & \frac{1}{\sqrt{2}} g\beta_e (B_x + iB_y) & -\frac{2}{3}D & \frac{1}{\sqrt{2}} g\beta_e (B_x - iB_y) \\ \langle -1| & E & \frac{1}{\sqrt{2}} g\beta_e (B_x + iB_y) & -g\beta_e B_z + \frac{D}{3} \end{array} \tag{88}$$

If the magnetic field B is taken along the Z axis, the determinant $\left|H - \lambda I\right|$ is computed with the simplified matrix

$$H - \lambda I = \begin{array}{c|ccc} \langle +1| & g\beta_e B_z + \frac{D}{3} - \lambda & 0 & E \\ \langle 0| & 0 & -\frac{2}{3}D - \lambda & 0 \\ \langle -1| & E & 0 & -g\beta_e B_z + \frac{D}{3} - \lambda \end{array} \tag{89}$$

since $B_x = B_y = 0$ and $D_x + D_y + D_z = 0$. Expansion of $\left|H - \lambda I\right|$ yields

$$\lambda = -\tfrac{2}{3}D \quad \text{and} \quad \tfrac{1}{3}D \pm \sqrt{E^2 + (g\beta_e B)^2} \tag{90}$$

and the energies can be expressed by

$$\begin{aligned} E_z &= -\tfrac{2}{3}D \\ E_{x,y} &= \tfrac{1}{3}D \pm \sqrt{E^2 + (g\beta_e B_z)^2} \end{aligned} \tag{91}$$

If $B_z = 0$, the zero field energies are obtained by

$$\begin{aligned} E_z &= -\tfrac{2}{3}D \\ E_{x,y} &= \tfrac{1}{3}D \pm E \end{aligned} \tag{92}$$

The energies for three states are depicted in Figure 44 for $B \| z$, $E \neq 0$, and $D > 0$. The system with uniaxial symmetry, there exist two degenerate states since $E = 0$.

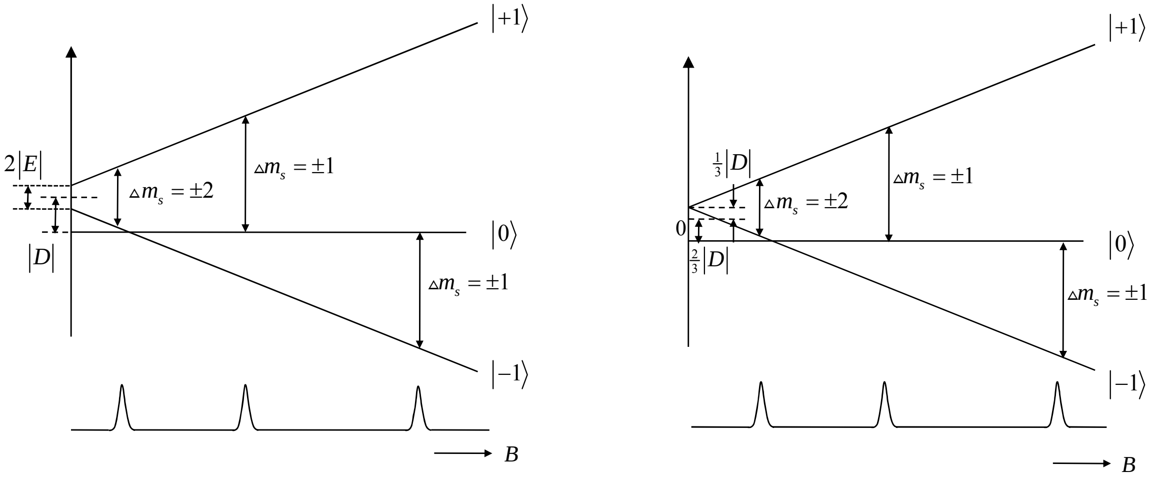

(a) (b)

Figure 44. The triplet state energies as a function of magnetic field (B‖z) for D>0and (a) E≠0 or (b) E=0.

APPENDIX B

FUNDAMENTAL CONSTANTS AND CONVERSION FACTORS

Table 4. Physical constants used in the magnetic resonance[6,13,14,15].

Planck's constant

$$h = 6.6261 \times 10^{-34}\,\mathrm{Js}$$

$$\hbar = h/2\pi = 1.0546 \times 10^{-34}\,\mathrm{Js}$$

Speed of light in the vacuum

$$c = 2.9979 \times 10^{8}\,\mathrm{m/s}$$

Permeability of the vacuum

$$\mu_0 = 4\pi \times 10^{-7}\,\mathrm{JC^{-2}s^{2}m^{-1}}(=\mathrm{T^{2}J^{-1}m^{3}})$$

Permittivity of the vacuum

$$\varepsilon_0 = 1/(\mu_0 c^2) = 8.8542 \times 10^{-12}\,\mathrm{J^{-1}C^{2}m^{-1}}$$

Electron charge

$$e = 1.6022 \times 10^{-19}\,\mathrm{C}$$

Electron mass

$$m_e = 9.1094 \times 10^{-31}\,\mathrm{kg}$$

Proton mass

$$m_p = 1.6726 \times 10^{-27}\,\mathrm{kg}$$

Bohr magnetron

$$\beta_e = \frac{e\hbar}{2m_e} = 9.2740 \times 10^{-24}\,\mathrm{J/T}$$

Nuclear magnetron

$$\beta_n = \frac{e\hbar}{2m_p} = 5.0508 \times 10^{-27}\,\mathrm{J/T}$$

Free-electron g factor

$$g_e = 2.0023$$

Free-electron gyromagnetic ratio

$$\gamma_e = -g_e\beta_e/\hbar = -1.7609 \times 10^{11}\,\mathrm{s^{-1}T^{-1}}$$

Nuclear gyromagnetic ratio for a proton ($g_n = 5.5854$)

$$\gamma_n = g_n\beta_n/\hbar = 4.2575 \times 10^{7}\,\mathrm{s^{-1}T^{-1}}$$

Table 4 Continued

Larmor frequency

$$\omega_0 = -\gamma B \,\text{rad/s}$$

$$\nu_0 = -\frac{\gamma B}{2\pi}\,\text{Hz}$$

*The positive and negative Larmor frequencies indicate the anticlockwise and clockwise processions, respectively.

Table 5. Useful conversion factors[6,13].

Magnetic field B (mT) to electron resonant frequency ν_e (MHz)

$$\nu_e(\text{MHz}) = \frac{g_e \beta_e B}{h}\frac{g}{g_e} = 28.0250\frac{g}{g_e}B(\text{mT})$$

Magnetic field B (mT) to nuclear resonant frequency ν_n (MHz) for a proton ($g_n = 5.5854$)

$$\nu_n(\text{MHz}) = \frac{g_n \beta_n B}{h} = 0.04258 B(\text{mT})$$

Calculation of electron g-factor

$$g = \frac{h\nu_e}{\beta_e B} = 0.0714\frac{\nu_e(\text{MHz})}{B(\text{mT})}$$

Table 6. Characteristics of selected atoms[6,13,16].

Element	Natural Abundance (%)	Spin I	g_n	Gyromagnetic Ratio $\gamma/(2\pi \cdot 10^6)$ $[\text{MHz}\cdot\text{s}^{-1}\cdot\text{T}^{-1}]$
^{1}H	99.985	$\frac{1}{2}$	5.5857	42.576
^{13}C	1.07	$\frac{1}{2}$	1.4048	10.705
^{14}N	99.632	1	0.4038	3.0766
^{15}N	0.368	$\frac{1}{2}$	-0.5664	-4.3156

APPENDIX C

OPTICAL SETUP FOR THE CONFOCAL MICROSCOPY

The experimental setup is based on a home-made scanning confocal microscopy as shown in Figure 45. A 532 nm CW frequency doubled Nd:YAG laser passes through an acousto-optic modulator and illuminates a diamond sample through a long working distance air objective with the aperture of 0.8 and magnification of 60 or a high numerical aperture (1.4) oil immersion objective of magnification 100.

A 2D galvanometer mirrors are used to scan the x-y image of the sample and a fine z-scan is achieved by a piezo objective mount to adjust the vertical position of the depth of focus within the diamond. The fluorescence light is collected with the same microscope objective, and focused into a multi-mode optical fiber. Spatial filtering is achieved by focusing on a 50 μm pinhole. To suppress the coupling of the green laser light into the fluorescence detection setup, a combination of a dichroic filter and a color filter were used. The fluorescence light from the single NV center is analyzed either by a Hanbury-Brown and Twiss setup or a spectrometer. It is finally detected by the single photon counting module (SPCM, PerkinElmer) using silicon avalanche photodiodes (APDs). As each incoming photon is detected, the APD generates a 35 ns wide TTL pulse, which is transmitted to the ultrafast multiple-event time digitizer for photon counting (P7888, FAST ComTec).

The Figure 46 shows the images of the NV centers between metal structures using the 250–300 nm of laser waist in the diamond. For the ^{12}C diamond, the NV centers were created by $^{15}N_2$ irradiation using the 200 keV energy at a dose of 10^9 electrons/cm2. The diamond was annealed in vacuum at 700°C for 1.5 hours.

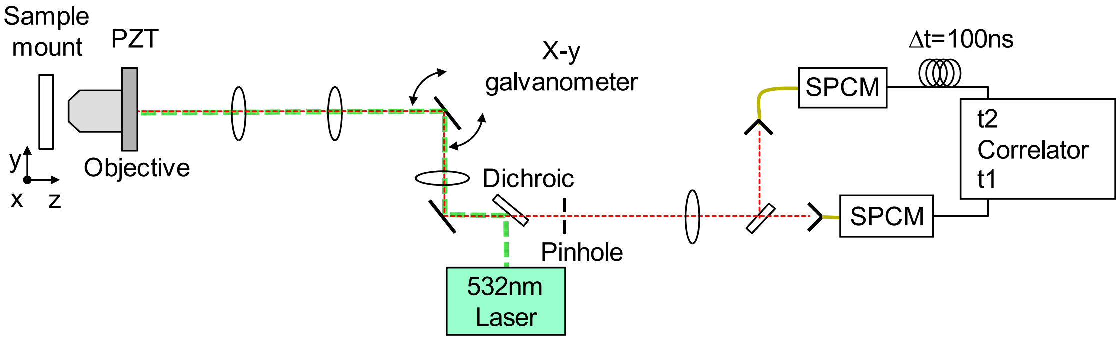

Figure 45. The schematic diagram plots the optical setup for shining the green laser on the sample and collecting the fluorescence emission into the photon counters.

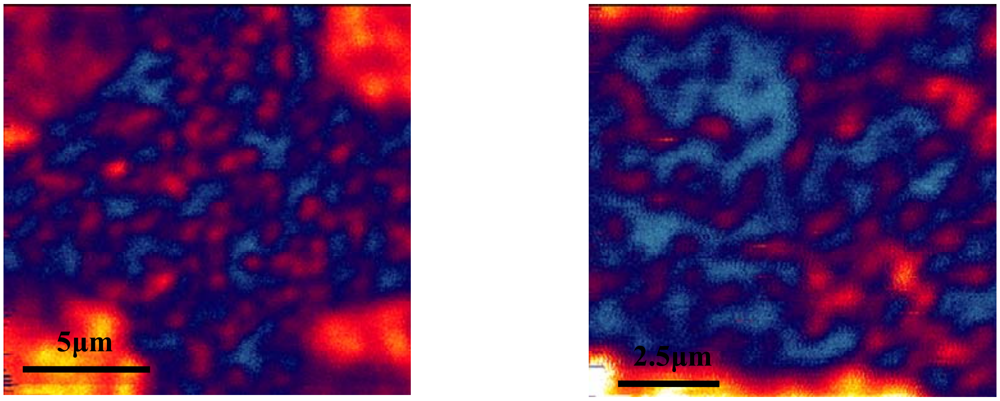

(a) (b)

Figure 46. The scanned fluorescence images of (a) the natural NV centers on the type Ib diamond and (b) the generated NV centers on the ^{12}C diamond.

The nanodiamond [see Figure 47] is a very useful source in creating the fluorescence emission. In order to generate the NV centers, the nanodiamonds are irradiated with electron or ion beams. They can be a promising tool in life science as a nanoprobe[17] and in the sensor industry requiring an electromagnetic field detector with the high sensitivity[18]. Recently researchers discovered a new route to produce the homogenous nanodiamonds with high yield[19].

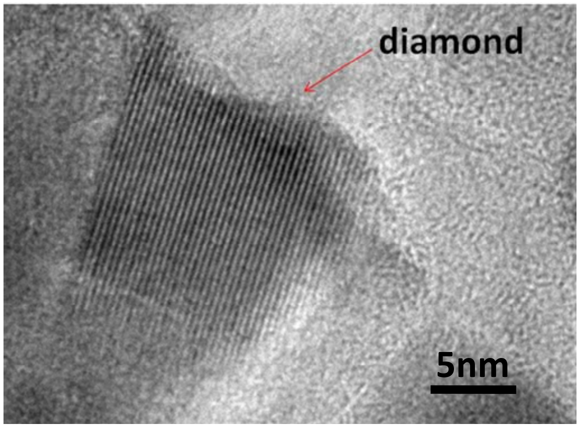

Figure 47. The TEM image of NV nanodiamond with the JEOL 2010 TEM at the 400 K magnification and 200 keV electron energy.

The time distribution of the emitted photons is characterized by the second order fluorescence autocorrelation function, which measures the joint probability of detecting the arrival of a photon at time t and another photon at time t $+\tau$ [20]. The normalized second order correlation function $g^{(2)}(\tau)$ is defined as: $g^{(2)}(\tau) = \langle I(t)I(t+\tau)\rangle / \langle I(t)\rangle^2$ where $I(t)$ is the fluorescence intensity at time t. When observing a single photon emitter, the correlation function shows a dip at zero time delay, $\tau = 0$, indicating that after a photon has been emitted, the system must be reexcited before a second photon can be emitted[21,22,23]. This phenomenon is referred to as antibunching. Since the TCSPC card has a dead time of 125 ns, it is necessary to apply an electronic delay longer than the TCSPC dead time to one of the two SPCM signals such that two fluorescence photons generated by the same laser pulse can both be detected[24]. If all emission is in the form of single photons and is well separated in time, then $g^{(2)}(\tau)=0$. Experimentally, the probability of exciting biexcitons cannot be reduced to zero. In a loss free measurement, if two independent but indistinguishable excited single photon emitters are present, it is found that $g^{(2)}(\tau)=1/2$. If the photons are emitted one at a time by a single quantum system, then the value of $g^{(2)}(\tau)$ is expected to lie between zero and 1/2[25,26,27].

APPENDIX D

HARDWARE FOR THE CW AND PULSED ESR

Conventional ESR/NMR employed magnetic resonance hardware involved in the readout scheme. The readout of the confocal microscopy experiments is completely optical and the magnetic resonance circuit is adapted in order to meet the requirements of the experimental approach. The microfabricated circuit is used for microwave signal transmission to manipulate the spin states of the NV center in diamond.

As shown in Figure 48, The microwave (mw) signal is generated by PTS 3200 and is amplified by a high power RF amp (Mini-Circuits). The mw signal generator is set to operate in triggered mode in order to synchronize the data acquisition (DAQ) card. For the pulsed experiments, the advanced pulse sequence is generated from a programmable pulse generator, PulseBlasterESR-Pro (SpinCore). The generated pulse sequence is used to control the laser light, microwave signal, and the photon counter.

The DAQ system and software are designed to meet the specific needs of experiments. DAQ is composed of three different parts: scanning, CW ESR, and pulse generation for pulsed ESR. For the signal generation and detection, the DAQ software is implemented on PCs using a National Instruments software, LabView.

For the scanning and CW and pulsed ODMR experiments, a program for both pulse sequence generation and data acquisition program was implemented. Since the equipment has its own delay or response time, accurate timing control is required to acquire valid data. For the pulsed ESR, the pulses trigger the microwave generator and the AOM for the laser light and the photon counter was triggered to synchronize the acquisition at each pulse sequence.

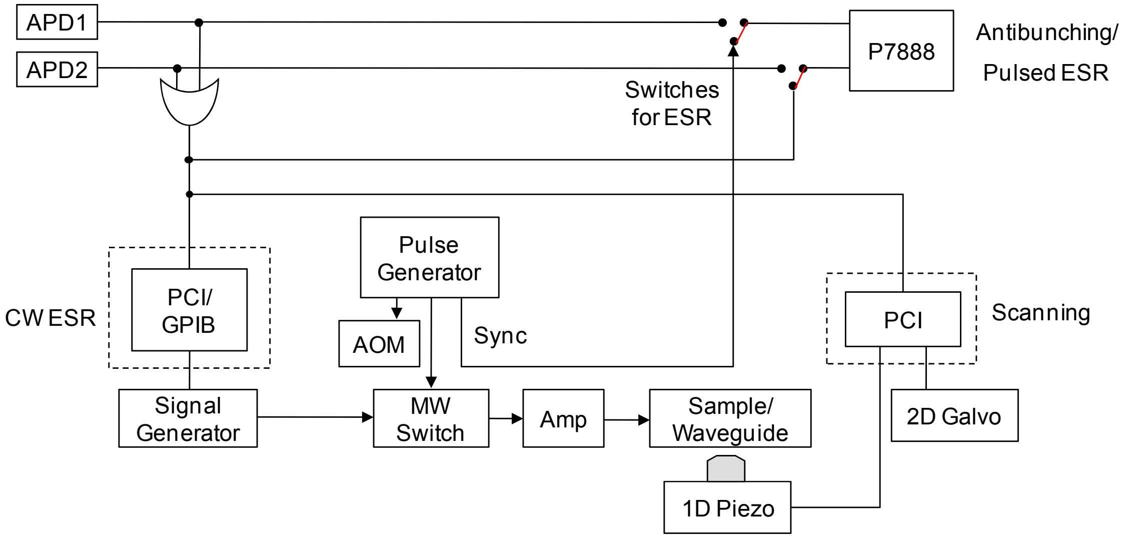

Figure 48. The block diagram depicts the data acquisition and microwave hardware control for scanning, CW ESR and pulsed ESR experiments.

APPENDIX E

MICROWAVE CIRCUIT FABRICATION

E.1 Vacuum System

In Figure 49, the vacuum system design shows the principal components of a vacuum metal deposition chamber for evaporation. In this design, the vacuum deposition chamber is large enough to guarantee the distance between the heated source and the substrates to minimize the radiated heating from the source[28]. For the thermal evaporation, the chamber has following general features[29]:

- A stainless steel or mild steel chamber
- Pumping capacity to reduce the chamber pressure down to 1×10^{-6} torr or below
- Evaporation source and power supply
- Pressure gauge
- Sample holder

The evaporation source (W or Mo) will be used to generate a heating to melt the target materials such as Ti and Au.

On the other hand, for plasma cleaning in the thin film technology, the reactive ion etching (RIE) uses RF glow discharges[30]. The reactive gas species, such as O_2 or CF_4, can be added to the chamber. Once the plasma is generated by the applied RF potentials between separate electrodes, the gas molecules break down into many fragments and radicals, some of which become ionized and are accelerated within the discharge chamber. A target sample is placed in the chamber and is exposed to a flux of ion bombardment. The ion bombardment and the chemical reaction between the gas species and the surface atoms of the sample which is the reactive etching chemistry clean the sample surface.

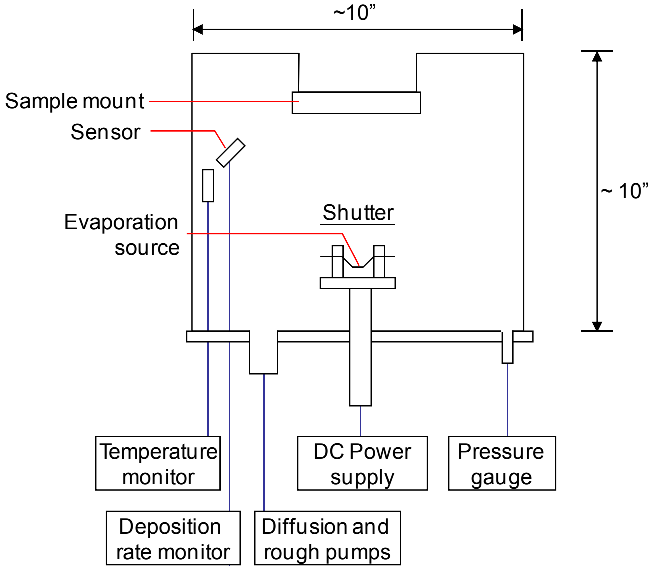

Figure 49. Vacuum chamber design for the thermal evaporator.

E.2 Microfabrication

The microfabrication technology is used to make micron-size metal structures directly on the diamond surface. Photolithography is the most critical process in microfabrication. There are three types of optical exposure: contact, proximity, and projection[31]. The proximity lithography is performed by bringing the mask 25–50 μm close to the resist surface. In contact mode, the mask touches the sample surface, thus the mask can get damages and unwanted residues may be left on the sample and the mask. In projection lithography, the complicated optics is utilized to project the mask image onto the sample surface. Typical resolution, i.e., the minimum feature size, for each mode is ~5 μm, ~ 1–2 μm, and sub-μm, respectively but the depth of focus, $\pm\lambda \cdot n/(2 \cdot NA^2)$ should be taken into account for the projection lithography.

For fabrication of a gold pattern used in experiments, a simple contact mask was used as shown in Figure 50. In order to facilitate the UV exposure, the high power UV laser diode ($P_{max} \approx 80$ mW and $\lambda = 405$ nm) was scanned using the 2D galvo scanner to shine the UV light over the mask area. This contact mask was practically capable of making ~5 μm-size pattern. In order to get higher resolution, the superior projection lithography may be used but some limitations should be considered[32].

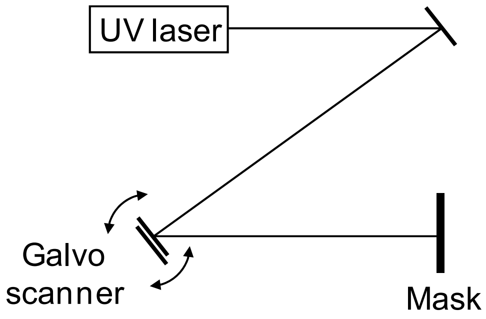

Figure 50. Photolithography setup for a contact mask.

Figure 51(a) shows the fabrication process of the gold wire for the microwave signal transmission for the experiment. It starts with a plasma cleaned bulk diamond. The sample substrate is coated with Ti and Au thin films in order. On top of metal surface, the 5–10 μm thick photoresist pattern is created by photolithography and development and the electroplating is followed. After the remaining photoresist is removed, the underlying thin metal layer below the photoresist is etched. The fabrication procedure is listed below:

- Sample cleaning with acids and a plasma cleaner
- Ti and Au deposition
- Spin-coating the photoresist and baking
- Developing the photoresist
- Plasma cleaning
- Electroplating
- Photoresist stripping
- Etching the Au and Ti thin films

Figure 51(b) shows the final image of the pattern which is mounted on the circuit board in the inset image.

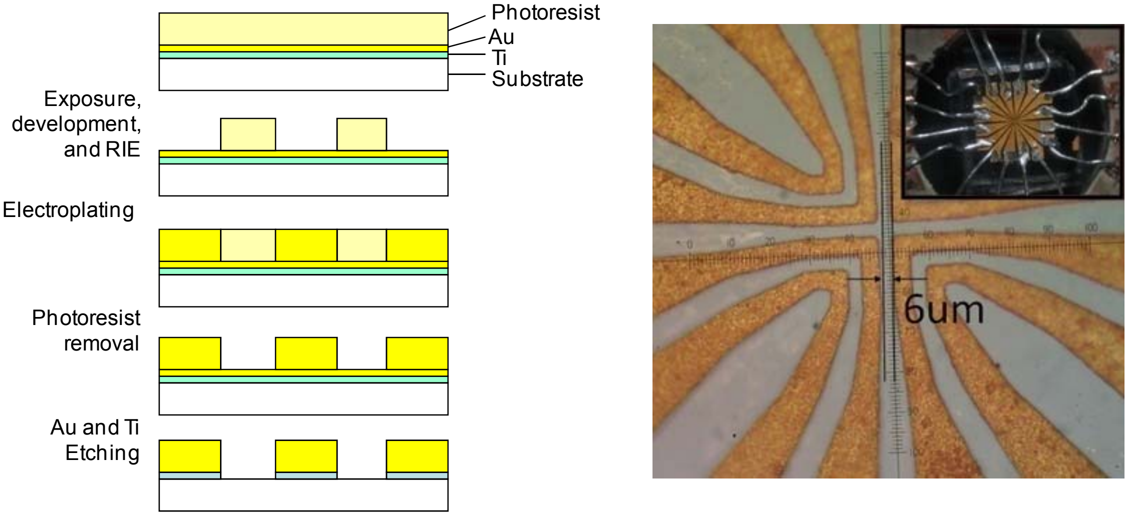

(a) (b)

Figure 51. (a) The fabrication procedure to make a gold structure is illustrated. (b) The gold plated ~10 μm wide pattern on a ^{12}C diamond is displayed.

APPENDIX F

REFERENCES IN THE APPENDICES

[1] J. J. Sakurai, *Modern Quantum Mechanics* (Addison-Wesley, New York, 1994).

[2] B. Odom, D. Hanneke, B. D'Urso, and G. Gabrielse, Phys. Rev. Lett. **97**, 030801 (2006).

[3] E. Fermi, Z. Physik. **60**, 320 (1930).

[4] G. Breit and I. I. Rabi, Phys. Rev. **38**, 2082 (1931).

[5] J. S. Blakemore, *Solid State Physics*, 2nd Ed. (Cambridge University Press, Cambridge, UK, 1985).

[6] J. A. Weil and J. R. Bolton, *Electron Paramagnetic Resonance*, 2nd Ed. (Wiley, New York, 2007).

[7] M. Brustolon and E. Giamello (Eds.), *Electron Paramagnetic Resonance: A Practitioner's Toolkit* (John Wiley & Sons, Hoboken, New Jersey, 2009).

[8] A. Abragam and B. Bleaney, *Electron Paramagnetic Resonance of Transition Ions* (Clarendon, Oxford, UK, 1970).

[9] S. Geschwind (Ed.), *Electron Paramagnetic Resonance* (Plenum, New York, 1972).

[10] A. Bencini and D. Gatteschi, *EPR of Exchange Coupled Systems* (Springer, Berlin, 1990).

[11] P. H. Rieger, *Electron Spin Resonance: Analysis and Interpretation* (RSC Publishing, Cambridge, UK, 2007).

[12] R. E. Coffman and A. Pezeshk, J. Magn. Reson. **70**, 21 (1986).

[13] C. P. Poole, Jr. and H. A. Farach (Eds.), *Handbook of Electron Spin Resonance: Data Sources, Computer Technology, Relaxation, and ENDOR* (AIP Press, New York, 1994).

[14] P. J. Mohr, B. N. Taylor, and D. B. Newell, Rev. Mod. Phys **80**, 633 (2008).

[15] P. J. Mohr, B. N. Taylor, and D. B. Newell, J. Phys. Chem. Ref. Data **37**, 1187 (2008).

[16] M. A. Bernstein, K. F. King, and X. J. Zhou, *Handbook of MRI Pulse Sequences* (Elsevier, Amsterdam, 2004).

[17] O. Faklaris, D. Garrot, V. Joshi, F. Druon, J. P. Boudou, T. Sauvage,. P. Georges, P. A. Curmi, and F. Treussart, Small **4**, 2236 (2008).

[18] J. M. Taylor, P. Cappellaro, L. Childress, L. Jiang, D. Budker, P. R. Hemmer, A. Yacoby, R. Walsworth, and M. D. Lukin, Nature Physics **4**, 810 (2008).

[19] http://www.sciencedaily.com/releases/2009/06/090604124806.htm

[20] V. Zwiller, H. Blom, P. Jonsson, N. Panev, S. Jeppesen, T. Tsegaye, E. Goobar, M-E. Pistol, L. Samuelson, and G. Björk, Appl. Phys. Lett. **78**, 2476 (2001).

[21] M. Ehrenberg and R. Rigler, Chem. Phys. **4**, 390 (1974).

[22] M. C. Teich and B. E. A. Saleh, Prog. Opt. **26**, 3 (1988).

[23] C. Cohen-Tannoudji and S. Reynaud, Philos. Trans. R. Soc. London, Ser. A **293**, 226 (1979).

[24] K. D. Weston, M. Dyck, P. Tinnefeld, C. Müller, D. P. Herten, and M. Sauer, Anal. Chem. **74**, 5342 (2002).

[25] C. Kurtsiefer, S. Mayer, P. Zarda, and H. Weinfurter, Phys. Rev. Lett. **85**, 290 (2000).

[26] A. Beveratos, R. Brouri, T. Gacoin, J.-Ph. Poizat, and Ph. Grangier, Phys. Rev. A **64**, 061802(R) (2001).

[27] A. Beveratos, R. Brouri, T. Gacoin, A. Villing, J. P. Poizat, and P. Grangier, Phys. Rev. Lett. **89**, 187901 (2002).

[28] D. M. Mattox, *Handbook of Physical Vapor Deposition (PVD) Processing* (Noyes Publications, Westwood, NJ, 1998).

[29] J. L. Vossen and W. Kern (Eds.), *Thin Film Processes II* (Academac Press, New York, 1991).

[30] S. M. Rossnagel, J. J. Cuomo, and W. D. Westwood (Eds.), *Handbook of Plasma Processing Technology: Fundamentals, Etching, Deposition, and Surface Interactions* (Noyes Publications, Park Ridge, NJ, 1990).

[31] N. Maluf and K. Williams, *An Introduction to Microelectromechanical Systems Engineering*, 2nd Ed. (Artech House, Boston, 2004).

[32] S. Rizvi (Ed.), *Handbook of Photomask Manufacturing Technology* (CRC Press, Boca Raton, FL, 2005).

VITA

Changdong Kim received his B.S. in electrical engineering from Korea University, Seoul, Korea in 2000. From 2000 to 2003, he was with Samsung Electronics, where he was a research engineer in the Optical Communication Lab. He received his M.S. in 2005 and Ph.D. in 2010 in electrical engineering at Texas A&M University. His research interests include confocal microscopy and electron spin resonance using an NV diamond. He also has research interests in the areas of quantum information, magnetic resonance, nanoscale imaging, micro/nanolithography, and vacuum systems.

Dr. Kim may be reached at: Department of Electrical Engineering, c/o Dr. Philip Hemmer, Texas A&M University, College Station, TX 77843-3128. His email is: ckim905@gmail.com.